

# Stochastic modelling of silicon nanoparticle synthesis

---

---

William Jefferson Menz  
Sidney Sussex College

October 15, 2013



A dissertation submitted for the degree of Doctor of Philosophy



# Stochastic modelling of silicon nanoparticle synthesis

William J. Menz

This thesis presents new methods to study the aerosol synthesis of nanoparticles and a new model to simulate the formation of silicon nanoparticles. Population balance modelling is used to model nanoparticle synthesis and a stochastic numerical method is used to solve the governing equations. The population balance models are coupled to chemical kinetic models and offer insight into the fundamental physiochemical processes leading to particle formation.

The first method developed in this work is a new mathematical expression for calculating the rate of Brownian coagulation with stochastic weighted algorithms (SWAs). The new expression permits the solution of the population balance equations with SWAs using a computationally-efficient technique of majorant rates and fictitious jumps. Convergence properties and efficiency of the expression are evaluated using a detailed silica particle model.

A sequential-modular algorithm is subsequently presented which solves networks of perfectly stirred reactors with a population balance model using the stochastic method. The algorithm is tested in some simple network configurations, which are used to identify methods through which error in the stochastic solution may be reduced. It is observed that SWAs are useful in preventing accumulation of error in reactor networks.

A new model for silicon nanoparticle synthesis is developed. The model includes gas-phase reactions describing silane decomposition, and a detailed multivariate particle model which tracks particle structure and composition. Systematic parameter estimation is used to fit the model to experimental cases. Results indicated that the key challenge in modelling silicon systems is obtaining a correct description of the particle nucleation process.

Finally, the silicon model is used in conjunction with the reactor network algorithm to simulate the start-up of a plug-flow reactor. The power of stochastic methods in resolving characteristics of a particle ensemble is highlighted by investigating the number, size, degree of sintering and polydispersity along the length of the reactor.

## Preface

This dissertation is the result of my own work and includes nothing which is the outcome of work done in collaboration, except where specifically indicated in the Acknowledgements. The work was performed at the Department of Chemical Engineering and Biotechnology at the University of Cambridge between October 2010 and June 2013. No other part of this thesis has been submitted for a degree.

The thesis contains 42 figures and 15 tables and approximately 30,000 words. Parts of this thesis have been published in the following articles:

- **W.J. Menz**, S. Shekar, G.P.E. Brownbridge, S. Mosbach, R. Körmer, W. Peukert and M. Kraft ‘Synthesis of silicon nanoparticles with a narrow size distribution: A theoretical study’ *Journal of Aerosol Science*, **44**:46–61, 2012.
- **W.J. Menz** and M. Kraft ‘A new model for silicon nanoparticle synthesis’ *Combustion and Flame*, **160**:947–958, 2013.
- **W.J. Menz** and M. Kraft ‘The suitability of particle models in capturing aggregate structure and polydispersity’ *Aerosol Science and Technology*, **47**:734–745, 2013.
- **W.J. Menz**, R.I.A. Patterson, W. Wagner and M. Kraft ‘Application of stochastic weighted algorithms to a multidimensional silica particle model’ *Journal of Computational Physics*, **248**:221–234, 2013.
- **W.J. Menz**, J. Akroyd and M. Kraft ‘Stochastic solution of population balance equations for reactor networks’ *Journal of Computational Physics*, **256**:615–629 2014.

William J. Menz  
October 15, 2013

## Acknowledgements

I would like to acknowledge the members of the Computational Modelling Group for their assistance: in particular, Prof. Markus Kraft (supervisor) for his guidance and Alastair Smith for tirelessly maintaining the group's computer resources.

The initial work towards this thesis was supported by collaboration with Dr. Richard Körner and Prof. Wolfgang Peukert at the Friedrich-Alexander-Universität Erlangen-Nürnberg. Their input on early silicon modelling attempts was invaluable.

The numerical aspects of the population balance modelling was developed with insight from Dr. Robert Patterson and Prof. Wolfgang Wagner at the Weierstrass Institute of Applied Analysis and Stochastics, Berlin. I would like to acknowledge them both for many useful discussions and some coding help.

Most importantly, I thank the Cambridge Australia Trust for providing the financial support, without whom my coming to Cambridge would not be possible.

# Contents

<b>Summary</b>	<b>iii</b>
<b>Preface</b>	<b>iv</b>
<b>Acknowledgements</b>	<b>v</b>
<b>List of Figures</b>	<b>ix</b>
<b>List of Tables</b>	<b>xi</b>
<b>1 Introduction</b>	<b>1</b>
1.1 Motivation . . . . .	2
1.2 Novel aspects of the thesis . . . . .	3
1.3 Structure of the thesis . . . . .	4
<b>2 Background</b>	<b>5</b>
2.1 Gas-phase chemical kinetics . . . . .	5
2.1.1 Rate expressions . . . . .	6
2.1.2 Three-body reactions . . . . .	7
2.1.3 Falloff reactions . . . . .	7
2.1.4 Thermochemistry . . . . .	8
2.1.5 Gas-phase library . . . . .	8
2.2 Population balance modelling . . . . .	8
2.2.1 The collision kernel . . . . .	11
2.2.2 Stochastic solution of the population balance equations	12
2.2.3 Other solution methodologies . . . . .	15
2.3 Reactor models . . . . .	16
2.3.1 Gas-particle coupling . . . . .	17
2.4 Error measurements . . . . .	17

2.5	Silicon nanoparticles . . . . .	19
2.5.1	Manufacture . . . . .	19
2.5.2	Applications . . . . .	21
<b>3</b>	<b>Choosing a particle model</b>	<b>23</b>
3.1	Model . . . . .	25
3.1.1	Type-space . . . . .	25
3.1.2	Derived properties . . . . .	26
3.1.3	Particle processes . . . . .	28
3.1.4	Average properties . . . . .	30
3.2	Case studies . . . . .	31
3.2.1	Coagulation and sintering . . . . .	31
3.2.2	Effect of polydispersity . . . . .	35
3.2.3	Computational resources . . . . .	37
3.3	Conclusions . . . . .	38
<b>4</b>	<b>A new coagulation kernel for stochastic weighted algorithms</b>	<b>40</b>
4.1	Model . . . . .	42
4.1.1	Type-space . . . . .	42
4.1.2	Particle processes . . . . .	42
4.2	Development of stochastic weighted algorithms . . . . .	45
4.2.1	Linear particle processes . . . . .	46
4.2.2	Coagulation process . . . . .	46
4.3	Numerical studies . . . . .	52
4.4	Results . . . . .	56
4.4.1	High-precision solution . . . . .	56
4.4.2	Convergence of algorithms . . . . .	58
4.4.3	Computational efficiency . . . . .	61
4.5	Conclusions . . . . .	64
<b>5</b>	<b>Solution of reactor networks</b>	<b>66</b>
5.1	Model . . . . .	68
5.1.1	Stochastic method . . . . .	69
5.1.2	Discrete Model . . . . .	72
5.1.3	Solution of reactor networks . . . . .	73
5.2	Numerical studies . . . . .	74
5.2.1	Comparison to Discrete Model . . . . .	74

5.2.2	Linear networks	76
5.2.3	Networks with recycle loops	80
5.2.4	Reactors with multiple inlets	82
5.3	Applications	84
5.3.1	Approximation of a PFR	84
5.4	Conclusions	86
<b>6</b>	<b>A detailed model for silicon nanoparticle synthesis</b>	<b>88</b>
6.1	Model development	91
6.1.1	Gas-phase kinetic model	91
6.1.2	Particle model	92
6.1.3	Particle processes	94
6.1.4	Coupling algorithm	98
6.2	Parameter estimation	99
6.3	Results and discussion	100
6.3.1	Numerical results	100
6.3.2	Case studies	102
6.4	Conclusions	112
<b>7</b>	<b>Putting it all together</b>	<b>114</b>
7.1	Particle model analysis	114
7.2	Unsteady-state response	118
7.3	Conclusions	121
<b>8</b>	<b>Conclusions</b>	<b>122</b>
8.1	Findings of this work	122
8.2	Suggestions for future work	124
<b>A</b>	<b>Appendix to Chapter 3</b>	<b>126</b>
A.1	Collision of particles in the near-spherical zone	126
A.2	Comparison of maximum sinterable surface area	127
<b>B</b>	<b>Appendix to Chapter 6</b>	<b>129</b>
B.1	Conversion of <i>SURFACE CHEMKIN</i> parameters	129
	<b>Nomenclature</b>	<b>131</b>

# List of Figures

2.1	Illustration of population balance solution methodologies . . .	12
2.2	Flowchart of the stochastic particle algorithm . . . . .	13
2.3	Schematic of the architecture of <i>MOPS</i> . . . . .	17
2.4	Temporal evolution of a macroscopic quantity in a particle system . . . . .	19
2.5	SEM image of highly-spherical silicon nanoparticles . . . . .	20
3.1	An illustration of different particle models' description of coagulation events . . . . .	29
3.2	Comparison of normalised mean collision diameter as a function of coagulation and sintering times . . . . .	33
3.3	Contours of difference between the binary-tree and surface-volume models . . . . .	34
3.4	Influence of polydispersity on particle morphology . . . . .	36
3.5	CPU time required for different particle models . . . . .	38
4.1	Comparison of the coagulation process implemented in direct simulation algorithm and weighted particle methods. . . . .	53
4.2	PSDs for the silica test case . . . . .	56
4.3	Temporal evolution of functionals describing the silica test case	57
4.4	Final values and confidence intervals of the key metrics for the silica model . . . . .	59
4.5	Relative statistical error in the final values of the key metrics for the silica model . . . . .	60
4.6	Computational time required for the coagulation algorithms .	62
4.7	Temporal evolution of number of coagulation events . . . . .	63
5.1	Algorithm used to solve the reactor network with Strang splitting. . . . .	74

5.2	Schematic of the test systems used in the present study . . . .	75
5.3	Transient evolution of moments for the three-reactor system .	77
5.4	Convergence of metrics for a linear network . . . . .	78
5.5	Comparison of statistical error in process metrics . . . . .	79
5.6	Convergence of metrics for $f_R = 0.5$ . . . . .	81
5.7	Statistical error as a function of recycle fraction . . . . .	82
5.8	Statistical error accumulation through a reactor network . . .	83
5.9	Convergence of network solutions to PFR solutions . . . . .	85
5.10	Comparison of network and PFR solutions . . . . .	86
6.1	Unimolecular rate constants for silicon decomposition . . . .	103
6.2	Experimental temperature profiles used in this work . . . . .	104
6.3	Comparison of experimental and theoretical PSDs for the case of Körmer et al. [75] . . . . .	106
6.4	Comparison of experimental and theoretical PSDs for the case of Frenklach et al. [49] . . . . .	107
6.5	Comparison of experimental and theoretical PSDs for the case of Wu et al. [163] . . . . .	108
6.6	Particle diameter dependence on silane for the system of Nguyen and Flagan [103] . . . . .	109
6.7	Comparison of experimental and theoretical PSDs for the case of Nguyen and Flagan [103] . . . . .	110
6.8	Temporal evolution of diameter for the case of Onischuk et al. [113] . . . . .	110
6.9	Comparison of experimental and computer-generated TEM images . . . . .	111
6.10	Temporal evolution of particle diameter in a laser-driven flame	112
7.1	Evolution of process metrics for the silicon model . . . . .	116
7.2	Trajectory of the case of Wu et al. [163] through the zones of Figure 3.3 . . . . .	117
7.3	Transient evolution of polydispersity and sintering level . . .	119
7.4	Transient evolution of collision diameter and number concen- tration . . . . .	120
A.1.1	Ratio of collision diameters, as predicted by different particle models . . . . .	127

# List of Tables

3.1	Comparison of derived properties of the particle models . . .	26
4.1	Particle selection properties for the weighted transition kernel	51
4.2	Definition of the coagulation weight transfer functions. . . .	51
4.3	Numerical and model parameters used in the silica test case .	54
4.4	Description of functionals used to investigate the silica model	55
5.1	Summary of process metrics studied in the present work. . . .	75
6.1	Gas-phase mechanism used for silane decomposition . . . . .	93
6.2	Heterogeneous reaction processes for silicon nanoparticles synthesis . . . . .	96
6.3	Numerical and model parameters used in the silicon model . .	98
6.4	Experimental data used to fit the silicon model . . . . .	100
6.5	Results of the parameter-fitting procedure . . . . .	101
6.6	Comparison of rate expressions for silane decomposition . . .	102
6.7	Process conditions of experimental test cases . . . . .	104
B.1	Surface reaction mechanism of Ho et al. [63] . . . . .	130
B.2	Estimation of surface-reaction pre-exponential for silicon . . .	131

# Chapter 1

## Introduction

It was not until the late 80's that the term *nanotechnology* entered the scientific vernacular [35]. Since then, the field has rapidly sub-divided and multiplied in size, like doomsday-bringing 'grey goo'. One of the biggest, and possibly most well-known areas of nanotechnology research is that which focuses on nanoparticles, defined as particles of diameter 1–100 nm.

One of the earliest identified uses of nanoparticles was as part of a decorative glaze applied to ceramic earthenware [39]. Gold, silver and copper 'nanoclusters'—formed during firing of the object—gave the ceramic its characteristic lustre. The nanoparticle glazes were made as early as the 10<sup>th</sup> century AD. Today, nanoparticles are both an engineered product for industrial or research purposes, and an undesirable by-product of human activity.

While it is common to think nanoparticles are an invention of humans, there are many which occur naturally. Fires and volcanic eruptions produce soot, which is composed of many different nano-sized moieties [105]. Physical and chemical processes in the soil may form inorganic nanoparticles [9], and organic structures such as viruses are often considered to be a type of nanoparticle [43].

Regardless of their origin, nanoparticles are of intense interest due to their unique properties. The small size and porous or aggregate structure of particles yield a large surface area to volume ratio [141], one of the factors to which these interesting properties are attributed. Quantum effects can come into effect at the 'nano' length-scale, in which strange but potentially useful characteristics manifest [80, 97].

The work in this thesis is directed towards understanding how nanoparticles can be made. In particular, population balance modelling will be used

to simulate the physiochemical processes leading to formation of nanoparticles in the gas-phase. New models and methods will be developed to elucidate the pathways to synthesising silicon nanoparticles, a material of considerable interest to industrial and research communities worldwide [88]. The motivation behind this will be discussed in Section 1.1, and the structure of the thesis will be presented in Section 1.3.

## 1.1 Motivation

The synthesis of nanoparticles in the gas-phase occurs over very short time-scales, on the order of microseconds. Therefore, it is difficult to characterise the processes responsible for particle formation with standard experimental techniques [128]. Modelling particle synthesis may be used as an alternative to experimentally characterising the formation processes. However, the challenge in obtaining experimental data can leave uncertainties in the kinetic expressions of the model. Such models typically utilise parameter estimation to arrive at approximate rates of particle processes [144].

As the properties of nanoparticles are strongly dependent on their size and morphology [2], it has become necessary to develop more detailed models which better-account for the physiochemical processes which yield the nanoparticle product. These models can potentially enhance process control [56], reduce waste [14] and improve product properties.

Models for nanoparticle synthesis could also be used to investigate where particles are *not* formed. Such knowledge could be used to suppress particle formation in conditions where inhalation of particles is a hazard [28, 106], or in conditions where particles are regarded as a contaminant in the manufacturing process [104].

The principal motivation of this work is to develop new methods and models for simulating silicon nanoparticle synthesis. Traditionally considered as an unwanted contaminant in semiconductor manufacture [41], they are now being evaluated as printable inks [7], medical imaging tracers [86] and in many other applications (see review by Mangolini [88]). The improvements to methods for modelling nanoparticle systems presented in this thesis will expand the flexibility of existing tools for solving the population balance equations. These methods are not restricted to the particular case of silicon.

## 1.2 Novel aspects of the thesis

In the first part of this thesis, new tools and methods for understanding nanoparticle synthesis with population balance models will be developed. Following that, a new model for silicon nanoparticle synthesis will be presented, and the new modelling tools will be used in conjunction with the silicon model to explore properties of an experimental system. Novel aspects this thesis include:

- A **comparison of particle models** commonly used in population balance modelling of nanoparticle formation. It is demonstrated that substantial errors can be incurred when using a particle model inappropriate for a particular modelling application.
- New insight into the structure and morphology of aggregate particles formed due to coagulation and sintering.
- A **new coagulation kernel** for stochastic weighted algorithms (SWAs). A detailed study of the numerical behaviour of the new kernel with a multidimensional silica particle model is conducted.
- A sequential modular approach to **solve a generic network** of reactors with a population balance model using a stochastic numerical method. The convergence of the stochastic particle algorithm in test networks is evaluated as a function of network size, feedback and numerical parameters.
- New **methods for accounting for particle transport** to- and from reactors with stochastic particle methods. The optimal transport and coagulation algorithms for some reactor systems are identified, yielding more efficient simulation of reactor networks.
- A detailed **multivariate silicon model** for the simulation of silicon nanoparticle synthesis from silane decomposition. The model is tested against a six different experimental configurations, with excellent fit observed for the majority of cases.

### 1.3 Structure of the thesis

Chapter 2 gives a review of the theory behind modelling gas-phase chemical kinetics, population balance modelling (particularly with reference to stochastic methods), and coupling of the two systems. The chapter is concluded with an overview of the methods for manufacture and potential future applications of silicon nanoparticles.

A mathematical description of particle models used in population balance modelling is provided in Chapter 3. Three models commonly used in the literature are compared under different conditions of coagulation and sintering. The results of this chapter highlight the importance of using multivariate particle models to capture the structure and morphology of aggregate particles.

In Chapter 4, a new mathematical expression is presented for calculating the rate of coagulation when using SWAs to solve the population balance equation. It is tested using a multivariate silica particle model, and the convergence and efficiency of the new expression are evaluated.

An algorithm for solving reactor networks with a population balance model using stochastic methods is presented in Chapter 5. The algorithm is tested for some simple reactor network configurations. These are used to identify methods through which systematic and statistical error in the stochastic solution may be reduced.

The formation of silicon nanoparticles is investigated in Chapter 6, where a new model for silicon nanoparticle synthesis is presented. Parameter estimation is used to fit the model to experimental cases. The new model is evaluated against a variety of experimental configurations at different process conditions in order to examine the goodness of fit. The physical significance of the model is also assessed.

The methods and models developed in this thesis will be tied-together in Chapter 7. First, the new silicon mechanism is analysed using the particle models discussed in Chapter 3. Secondly, the new coagulation kernel of Chapter 4 and reactor network algorithm of Chapter 5 are used with the new silicon model to simulate the start-up of a plug-flow reactor.

The findings of the thesis are concluded and suggestions for future work are presented in Chapter 8.

## Chapter 2

# Background

This chapter provides a theoretical background for the modelling work conducted in this thesis. In Section 2.1, the principles of kinetic modelling are outlined, which form the basis of the silicon chemical mechanism developed in Chapter 6. The population balance equations and the stochastic methodology to solve them are introduced in Section 2.2, which are used throughout this work for modelling nanoparticle formation.

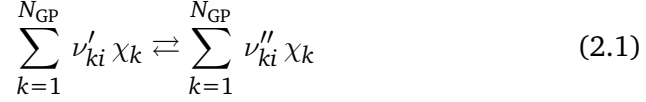
The equations which compose the reactor models, and the theory of coupling the gas-phase and particle solvers are given in Section 2.3. Numerical metrics to measure the accuracy and precision of the stochastic population balance solver, particularly relevant to Chapters 4 and 5, are discussed in Section 2.4. Finally, a literature review of the manufacture and applications for silicon nanoparticles is given in Section 2.5, which will be built upon in Chapters 6 and 7.

### 2.1 Gas-phase chemical kinetics

Kinetic modelling is used in order to understand the rate at which a chemical species converts into other chemical species. The collection of gas-phase chemical species and reactions will be referred to throughout this text as the ‘gas-phase mechanism’ or the gas-phase state-space,  $G$ . Combining a mechanism with a reactor model (discussed in Section 2.3) and solving the resultant system of ordinary differential equations (ODEs) yields the temporal evolution of chemical species concentrations.

### 2.1.1 Rate expressions

Chemical reaction  $i$  in  $N_{\text{rxn}}$  reactions may be represented in the general form [71]:



where  $\nu'_k$  and  $\nu''_k$  are the forward and reverse stoichiometric coefficients of species  $k$  for  $N_{\text{GP}}$  chemical species with chemical symbols  $\chi_k$ .  $k$  will be used here to index the gas-phase species. The production rate of species  $k$  is given by the sum of the rate of all forward and backwards reactions involving species  $k$ :

$$\dot{\omega}_k = \sum_{i=1}^{N_{\text{rxn}}} \nu_{ki} q_i \quad (2.2)$$

where  $\nu_{ki}$  is the net production rate:

$$\nu_{ki} = \nu''_{ki} - \nu'_{ki} \quad (2.3)$$

and  $q_i$  is the rate of progress variable for the  $i$ th reaction. The form of the rate of progress variable depends on the type of reaction under consideration. Generally, it is given by:

$$q_i = k_{fi} \prod_{k=1}^{N_{\text{GP}}} c(\chi_k)^{\nu'_{ki}} - k_{ri} \prod_{k=1}^{N_{\text{GP}}} c(\chi_k)^{\nu''_{ki}} \quad (2.4)$$

where  $c(\chi_k)$  is the molar concentration ( $\text{mol}/\text{m}^3$ ) of chemical species  $k$ ,  $k_{fi}$  is the forward rate constant and  $k_{ri}$  is the reverse rate constant. The best-known form for the forward rate constant is the modified-Arrhenius equation:

$$k_f = A T^\beta \exp\left(-\frac{E_A}{RT}\right) \quad (2.5)$$

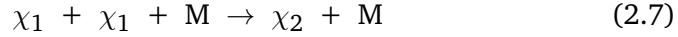
where  $A$ ,  $\beta$  and  $E_A$  are constants specific to the reaction. If reaction parameters are not specified for the reverse reaction, the reverse rate coefficient is given by:

$$k_r = k_f / K_C \quad (2.6)$$

where  $K_C$  is the equilibrium constant for the reaction, which can be obtained from the thermodynamic properties of the reacting species [71].

### 2.1.2 Three-body reactions

A third body, or collision partner, is often necessary for some reactions to proceed [63, 71]. These bodies are typically denoted by a generic collision species with chemical symbol M. An example of how such reactions can be written is:



where  $\chi_1$  and  $\chi_2$  are reactant and product chemical species, respectively.

In this work, it is assumed that all chemical species in a mixture contribute equally as third bodies. This results in the following formulation of the rate of progress variable:

$$q_i = \left( \sum_{k=1}^{N_{\text{GP}}} c(\chi_k) \right) \left( k_{\text{fi}} \prod_{k=1}^{N_{\text{GP}}} c(\chi_k)^{\nu'_{ki}} - k_{\text{ri}} \prod_{k=1}^{N_{\text{GP}}} c(\chi_k)^{\nu''_{ki}} \right) \quad (2.8)$$

The summation term is often represented as the concentration of species M:

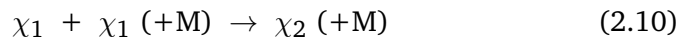
$$c(M) = \left( \sum_{k=1}^{N_{\text{GP}}} c(\chi_k) \right) \quad (2.9)$$

The calculation of the forward and reverse rate coefficients remains unchanged.

### 2.1.3 Falloff reactions

Equations (2.4) and (2.5) for standard Arrhenius reactions are typically used to describe reaction rates at the high-pressure limit, where the rate is dependent on temperature. However, three-body reactions imply a dependence on mixture pressure due to the  $c(M)$  term in the rate of progress variable. This condition is met when the system is near the low-pressure limit [71].

Expressions for the rate constant which span the low- and high-pressure limits are termed falloff reactions, as they include a blending function to account for the overlap between regions [71]. A falloff reaction is denoted by a (+M) term in a chemical reaction:



There are a variety of expressions to account for the reaction rate in the falloff region [87, 148, 151]. The equation of Lindemann et al. [87]

is the simplest and is used in this thesis. Two sets of modified-Arrhenius parameters are first defined: those for the high-pressure limit ( $k_\infty$ ) and the low-pressure limit ( $k_0$ ) according to Equation (2.5). The rate constant at any pressure is then given by:

$$k = k_\infty \left( \frac{P_r}{1 + P_r} \right) \quad (2.11)$$

where  $P_r$  is the reduced pressure, given by:

$$P_r = \frac{k_0 c(M)}{k_\infty} \quad (2.12)$$

#### 2.1.4 Thermochemistry

In order to calculate equilibrium coefficients, heat capacities, and other thermodynamic properties of chemical species, reliable thermochemical data is required. Such data is readily available on-line [150] or in other peer-reviewed literature (e.g. [149]). Alternatively, it is possible to derive this data through use of quantum-mechanical calculations and statistical mechanics (e.g. [126, 145]). In this work, thermochemical data in the form of NASA polynomials is used [20].

#### 2.1.5 Gas-phase library

It is necessary to solve a system of many ODEs when investigating the chemical behaviour system with many reactions. Before this can be done, the mechanism must be interpreted by a gas-phase chemical kinetics library, which supplies the rate of progress and mixture properties to an ODE solver.

This work uses an in-house built library named *Sprog* to determine chemical reaction rates and gas-phase mixture properties. *Sprog* is written in C++ and has been validated against other popular libraries such as *CHEMKIN* [71, 132] and *Cantera* [24].

## 2.2 Population balance modelling

The nucleation and growth of particles may be simulated with a population balance model. In order to formulate the population balance equations, which govern the behaviour of such models, it is necessary to mathematically describe a particle. This representation is called the type-space of a

particle, denoted as  $P$ . The collection of all particles and the information used to describe them is called the particle state-space,  $Z$ .

The evolution of the number density of particles  $n(t, P_q)$  at time  $t$  and of type  $P_q \in Z$  is described by a population balance equation:

$$\frac{d}{dt}n(P_q) = \mathcal{I}(\mathbf{c}, P_q) + \mathcal{K}(\mathbf{n}, P_q) + \mathcal{R}(\mathbf{c}, \mathbf{n}, P_q) + \mathcal{S}(\mathbf{n}, P_q) \quad (2.13)$$

where  $\mathcal{I}(\mathbf{c}, P_q)$ ,  $\mathcal{K}(\mathbf{n}, P_q)$ ,  $\mathcal{R}(\mathbf{c}, \mathbf{n}, P_q)$  and  $\mathcal{S}(\mathbf{n}, P_q)$  are the inception, coagulation, surface growth and sintering operators of particles of type  $P$ , respectively. The index  $q$  will be used to index particles throughout this work. The variable  $\mathbf{c}$  is the vector of gas-phase species concentrations and  $\mathbf{n}$  is the vector of particle concentrations. Each of these processes represents a reaction which alters type-space of a particle, however the actual transformation of the particle depends on the particle model used. These reactions and operators are explained in a general form below.

### Inception

Particles are created in the population balance by an inception process. The terms inception and nucleation will be used interchangeably in this thesis. This is represented by the following reaction:



where  $\chi_i$  and  $\chi_j$  are nucleating gas-phase species. The rate of nucleation is described by the inception operator  $\mathcal{I}(\mathbf{c}, P_q)$ :

$$\mathcal{I}(\mathbf{c}, P_q) = \frac{1}{2} \sum_{\substack{\chi_i, \chi_j \in G; \\ \chi_i + \chi_j = P_q}} K(\chi_i, \chi_j) c(\chi_i, t) c(\chi_j, t) \quad (2.15)$$

where  $K$  is the collision kernel, a function which defines the rate of collision, for the process. Equation (2.14) defines the  $+$  operator in the summation term of Equation (2.15). This representation will be used for the subsequent particle processes.

### Coagulation

Particles coagulate and stick together according to the following reaction:



The rate of coagulation depends on the choice of coagulation kernel  $K$ , which defines the probability of collision. Particles of type  $P_i$  coagulate with particles of type  $P_j$  at a rate  $K(P_i, P_j)$  according to the Smoluchowski equation, such that:

$$\begin{aligned} \mathcal{K}(\mathbf{n}, P_q) = & \frac{1}{2} \sum_{\substack{P_i, P_j \in Z; \\ P_i + P_j = P_q}} K(P_i, P_j) n(P_i, t) n(P_j, t) \\ & - n(P_q, t) \sum_{P_i \in Z} K(P_q, P_i) n(P_i, t) \end{aligned} \quad (2.17)$$

The first term in Equation (2.17) represents the formation of particles due to the collision of smaller particles. The second term represents the depletion of particles due to coagulation with larger particles.

### Surface growth

Surface growth refers to the addition of mass to particles from a different phase. This is typically described as a collisional process of a particle with a gas-phase species (condensation) or a heterogeneous reaction of a gas-phase species with the particle surface (surface reaction). Such events occur in the following manner:



The surface growth operator is given by:

$$\begin{aligned} \mathcal{R}(\mathbf{c}, \mathbf{n}, P_q) = & \sum_{\substack{P_i \in Z; \\ \chi_j \in G; \\ P_j + \chi_i = P_q}} R_{SG}(\chi_j, P_i) n(P_i, t) c(\chi_j, t) \\ & - \sum_{\chi_j \in G} R_{SG}(\chi_j, P_q) n(P_q, t) c(\chi_j, t) \end{aligned} \quad (2.19)$$

where  $R_{SG}$  is the surface growth rate:

$$R_{SG}(\chi_j, P_q) = \begin{cases} K(\chi_j, P_q) & \text{for condensation} \\ R_{SR}(\chi_j, P_q) & \text{for surface reaction} \end{cases}$$

$R_{SR}$  is the surface reaction rate, given by a Arrhenius expression, e.g. Equation (2.5).

## Sintering

Sintering refers to the reduction in particle surface area due to internal rearrangement of the component atoms or molecules. The form of a sintering reaction is strongly dependent on the particle model chosen. In general, they take the form:

$$S(P_i) \xrightarrow{\varsigma(P_q)} S(P_q) \quad (2.20)$$

where  $S$  is the surface area of the particle and  $S(P_q) \leq S(P_i)$  through transformation  $\varsigma$ . The sintering operator is given by:

$$S(\mathbf{n}, P_q) = \left[ \sum_{\substack{P_i \in Z; \\ \varsigma(P_i) = P_q}} R_{\text{sint}}(P_i) n(P_i, t) \right] - R_{\text{sint}}(P_q) n(P_q, t) \quad (2.21)$$

where  $R_{\text{sint}}$  is the rate of sintering for the particle.

### 2.2.1 The collision kernel

Equations (2.15), (2.17) and (2.19) utilise a ‘coagulation kernel’ to estimate the collision probability of two entities. The transition kernel  $K^{\text{tr}}$ , a computationally-efficient approximation of Brownian coagulation [70, 121], will be used in this thesis. It is given by:

$$K^{\text{tr}}(X_i, X_j) = \left( \frac{1}{K^{\text{fm}}(X_i, X_j)} + \frac{1}{K^{\text{sf}}(X_i, X_j)} \right)^{-1} \quad (2.22)$$

where  $X \in G, Z$ ; either a gas-phase or particle species.  $K^{\text{fm}}$  is the free-molecular kernel and  $K^{\text{sf}}$  is the slip-flow kernel. The dominant kernel is dependent on the Knudsen number ( $Kn$ ). The free-molecular kernel is dominant for  $Kn \gg 1$  [70] and takes the form:

$$K^{\text{fm}}(X_i, X_j) = k_{\text{fm}} \sqrt{\frac{\pi k_B T}{2}} \left( \frac{1}{m_i} + \frac{1}{m_j} \right)^{\frac{1}{2}} (d_i + d_j)^2 \quad (2.23)$$

where  $k_B$  is Boltzmann’s constant,  $T$  is the temperature and  $m_i$  and  $d_i$  are the mass and collision diameter of species  $i$ , respectively.  $k_{\text{fm}}$  is the free molecular enhancement factor, applied for the enhancement of the coagulation rate due to van der Waals forces [60]. After substitution of the Cunningham

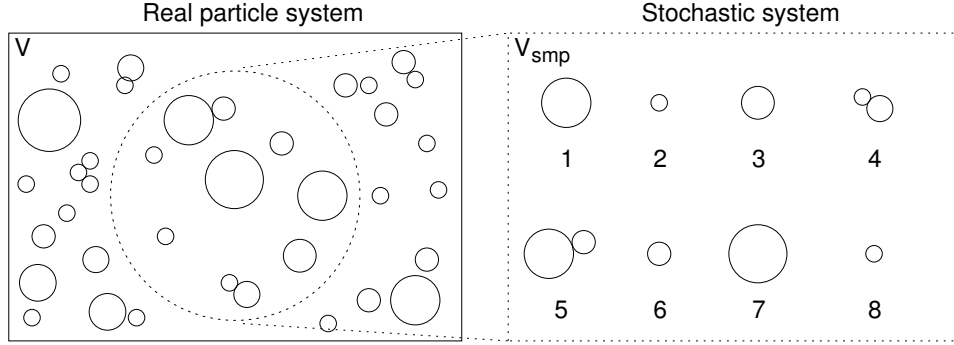


**Figure 2.1:** Illustration of the stochastic solution methodology for the population balance equations.

slip correction factor and the Knudsen number, the slip flow kernel is given by [70]:

$$K^{\text{sf}}(X_i, X_j) = \frac{2k_{\text{B}}T}{3\mu} \left( \frac{1}{d_i} + \frac{1}{d_j} + 1.257(2\sigma) \left[ \frac{1}{d_i^2} + \frac{1}{d_j^2} \right] \right) (d_i + d_j) \quad (2.24)$$

where  $\mu$  is the gas viscosity and  $\sigma$  is the mean-free-path of gas molecules.

## 2.2.2 Stochastic solution of the population balance equations

This thesis is primarily concerned with using stochastic methods to solve the population balance equations, however other methods are briefly discussed in Section 2.2.3. Stochastic methods approximate the real particles with a collection of computational particles in a sample volume  $V_{\text{smp}}$ .

In the illustration of Figure 2.1, an ensemble of eight computational particles is used to approximate the real system. Here,  $N(t)$  will be used to denote the number of computational particles in an ensemble, with the maximum capacity given the symbol  $N_{\text{max}}$ . Based on the properties of these particles, the stochastic particle algorithm calculates the particle process rates described by Equations (2.15), (2.17), (2.19) and (2.21).

A process is selected to be performed, based on the rates. A particle is then selected as the object of the process and is modified according to the physiochemical reaction of the process, defined by Equations (2.14), (2.16), (2.18) and (2.20). The process is repeated until the final time ( $t_f$ ) is reached. This algorithm is illustrated in Figure 2.2.

The stochastic population balance solver is written in C++ and named *Sweep*. In previous work, the basic stochastic algorithm has been modified

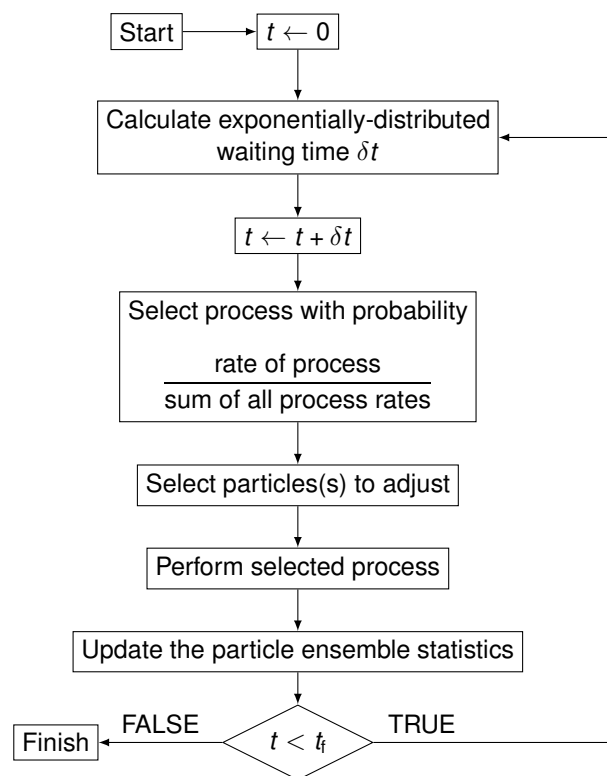


**Figure 2.2:** Stochastic algorithm for solving the population balance equation.

to increase its computational efficiency [37, 53, 120]. These improvements are described in the following subsections.

### Binary tree for ensemble statistics

The stochastic algorithm requires calculation of the total process rate in every timestep  $\delta t$  (Figure 2.2). This requires looping over each possible collision pair for coagulation, resulting in an order  $N(t)^2$  computational expense [53]. This problem is avoided by storing information about particles in a binary tree, which reduces the order of expense to  $N_{\max} \log(N_{\max})$  [54]. Each node of the tree stores a partial sum of the properties of a particle from the nodes below it. Thus, when a particle is changed, only the ‘branch’ of the tree on which the particle lies must be updated. It also enables rapid selection of a particle based on individual structural properties, e.g. surface area [54].

### Majorant rates and fictitious jumps

The expressions typically used for the collision kernel  $K$  in the coagulation process contain cross-terms, that is, they cannot be written as linear sums of particle properties (e.g.  $\sqrt{a+b}$ ). However, as the binary-tree pre-calculates certain sums, the rate calculation could be accelerated if the coagulation kernel was rewritten to take advantage of these sums. Eibeck and Wagner [37] proposed majorant kernels are used to resolve this issue. A majorant kernel  $\hat{K}$  must be greater than or equal to  $K$  for all  $P \in Z$  and should be fast and efficient to calculate. A majorant kernel for the free-molecular regime was presented by Goodson and Kraft [53], and a majorant formulation for the transition kernel was given by Patterson et al. [121]. A new majorant kernel is presented in this work in Chapter 4.

To correct for the over-estimation of the coagulation rate from use of a majorant kernel, the concept of fictitious jumps is introduced. When two particles are selected for coagulation, the true rate  $R$  (that calculated with the full kernel  $K$ ) and majorant rate  $\hat{R}$  are calculated for the particle pair. Fictitious jumps, those where the process is not actually performed for the particle pair, will occur with probability  $1 - R/\hat{R}$ .

### **Linear process deferment**

Linear processes are those which involve a single-particle interaction, e.g. surface growth or sintering. It is often the case that the rate of these processes is much greater than that of non-linear processes such as coagulation [8, 92], resulting in more computational effort being devoted to linear interactions. Patterson et al. [120] presented the Linear Process Deferment Algorithm (LPDA) to address this, in which the stochastic algorithm (Figure 2.2) does not include linear processes in the main loop. The deferred processes are performed in bulk on each particle at the end of an arbitrary timestep  $\Delta t$ .

### **2.2.3 Other solution methodologies**

As this thesis focuses on stochastic solution of the population balance equations, the two most popular alternative methods for solution are mentioned briefly here.

#### **Moment methods**

The method of moments [47, 48] describes the evolution of a population of particles by the moments of the distribution. It is typically fast, however the particle size distribution (PSD) can not be resolved from the results of such calculations. Despite this, their speed often makes them the choice for coupling with detailed computational fluid dynamics (CFD) calculations [3, 89].

#### **Sectional methods**

The sectional methods split the distribution of particle properties into sections [65], allowing resolution of PSD. The choice of sections is non-trivial, and often they must be dynamically chosen [156]. These methods are often more computationally expensive [165] than the moments method and can only be extended to multiple internal dimensions with great difficulties [61]. A type of sectional method will briefly be introduced in more detail in Chapter 5.

## 2.3 Reactor models

A reactor model defines how the temperature, pressure and volume of a reactor change with time. These factors are dependent on the assumptions made about the reactor and the source terms provided by the gas-phase and particle solvers. The choice of reactor model depends on the system which is to be modelled: two of the most common target modelling systems for nanoparticle synthesis are flames and plug-flow reactors (PFRs). As a stochastic approach for solving the population balance equations considers the transient evolution of a sample volume, it is common to use reactor models which are compatible with such restrictions. A common simplification is to take a Lagrangian view of particles (and gas) evolving along a streamline of a reactor or flame [99]. In this approximation, the equations governing the reactor are identical to a zero (spatial) dimensional batch reactor [26, 143].

The equations governing such systems are now presented. The rate of change in concentration of species  $k$  is given by:

$$\frac{dc_k}{dt} = \dot{\omega}_k(\mathbf{c}, T) + \dot{g}_k(\mathbf{c}, \mathbf{n}, T) - \gamma(\mathbf{c}, \mathbf{n}, T)c_k \quad (2.25)$$

where  $\dot{g}_k(\mathbf{c}, \mathbf{n}, T)$  is the molar production rates of species  $k$  at temperature  $T$  due to particle reactions. The production rate due to gas-phase reactions  $\dot{\omega}_k(\mathbf{c}, T)$  is given by Equation (2.2). The gas-phase expansion factor  $\gamma$  for the reactor is:

$$\gamma(\mathbf{c}, \mathbf{n}, T) = \frac{1}{\rho} \left( \sum_{k=1}^{N_{\text{GP}}} [\dot{\omega}_k + \dot{g}_k] \right) + \frac{1}{T} \frac{dT}{dt} \quad (2.26)$$

where  $\rho$  is the molar density of the mixture. Ignoring energy changes due to the particle population balance, the adiabatic energy balance of a constant-pressure reactor is:

$$\rho \bar{C}_p \frac{dT}{dt} = \sum_{k=1}^{N_{\text{GP}}} -\hat{H}_k \dot{\omega}_k \quad (2.27)$$

where  $\bar{C}_p$  is the bulk heat capacity and  $\hat{H}_k$  is the specific molar enthalpy of species  $k$ . The energy balance is analogous for a constant-volume reactor, however the specific molar internal energy is used in place of enthalpy. These equations will be expanded in Chapter 5 for modelling networks of reactors where transport of material between reactors can not be neglected.

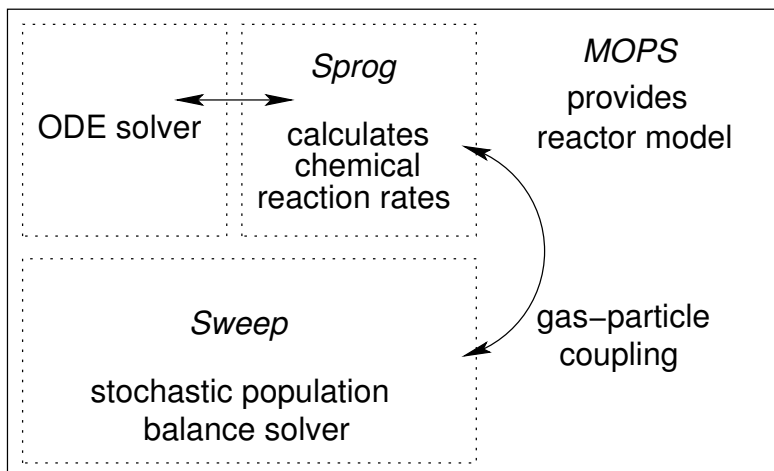


**Figure 2.3:** Schematic of the architecture of *MOPS*.

### 2.3.1 Gas-particle coupling

Equations 2.15, 2.19, 2.25 and 2.26 imply a two-way relationship between the particle- and gas-phase. Thus, it is appropriate to adopt a method of coupling to link the two. Here, the technique of operator splitting is employed to couple the gas- and particle-phases. In this work, Strang splitting is the chosen form of operator splitting. The algorithm by which this is done has been described in detail by Celnik et al. [25] and Shekar et al. [143].

The stochastic population balance solver (*Sweep*) is coupled with the gas-phase chemistry interface (*Sprog* and a separate ODE solver) in a code called *MOPS*. The flow of information through these libraries is illustrated in Figure 2.3. Implementation of the reactor models and network infrastructure developed for the present work (Chapter 5) is also administered by *MOPS*.

## 2.4 Error measurements

Chapters 4 and 5 investigate the convergence of the stochastic particle method’s solution as a function of numerical parameters. The stochastic particle method has three parameters which affect its numerical error, namely the maximum number of computational particles ( $N_{\max}$ ), the number of independent runs ( $L$ ) and the splitting timestep size ( $\Delta t_s$ ) [25]. This numerical error is composed of two parts: the systematic and statistical error ( $\epsilon_{\text{stat}}$ ).

The former is related to the accuracy of the stochastic solution. It is associated with choice of numerical parameters, for example too few computational particles. The statistical error is representative of the fluctuations due to the pseudorandom choices made in selecting particles and processes in the stochastic algorithm.

The systematic and statistical error can be assessed by generating  $L$  independent estimates of the particle system, and comparing the macroscopic quantities of the system ( $X(t)$ ) for a given set of numerical parameters. The temporal evolution of these functionals is averaged over the number of independent runs:

$$\xi^{(N_{\max},L)}(t) = \frac{1}{L} \sum_{l=1}^L X_l^{(N_{\max})}(t) \quad (2.28)$$

The confidence interval  $I_P$  for  $\xi^{(N_{\max},L)}(t)$  is given by:

$$I_P^{(N_{\max},L)}(t) = a_P \sqrt{\frac{\text{Var}^{(N_{\max},L)}(t)}{L}} \quad (2.29)$$

where  $P$  is the confidence level. In this work,  $P = 0.999$  is used, for which  $a_{0.999} = 3.29$  from normal distribution tables [143]. The variance is approximated by:

$$\text{Var}^{(N_{\max},L)}(t) = \frac{1}{L-1} \left[ \sum_{l=1}^L X_l^{(N_{\max})}(t)^2 \right] - \left[ \xi^{(N_{\max},L)}(t) \right]^2 \quad (2.30)$$

The total error is then estimated by calculating the normalised average absolute error ( $\bar{\epsilon}$ ) over  $M$  time intervals [25]:

$$\bar{\epsilon}^{(N_{\max},L)} = \frac{1}{M} \sum_{m=1}^M \frac{|\xi^{(N_{\max},L)}(t_m) - X^*(t_m)|}{X^*(t_m)} \quad (2.31)$$

where  $X^*(t)$  is the ‘true solution’, which could be that found analytically. Where analytical solutions are unavailable, a high-precision stochastic solution is used [143]. The normalised statistical error can be estimated by taking the ratio of the confidence interval and the mean:

$$\epsilon_{\text{stat}}^{(N_{\max},L)}(t) = \frac{I_P^{(N_{\max},L)}(t)}{\xi^{(N_{\max},L)}(t)} \quad (2.32)$$

The normalised average statistical error may then be obtained:

$$\bar{\epsilon}_{\text{stat}}^{(N_{\max},L)} = \frac{1}{M} \sum_{m=1}^M \epsilon_{\text{stat}}^{(N_{\max},L)}(t_m) \quad (2.33)$$

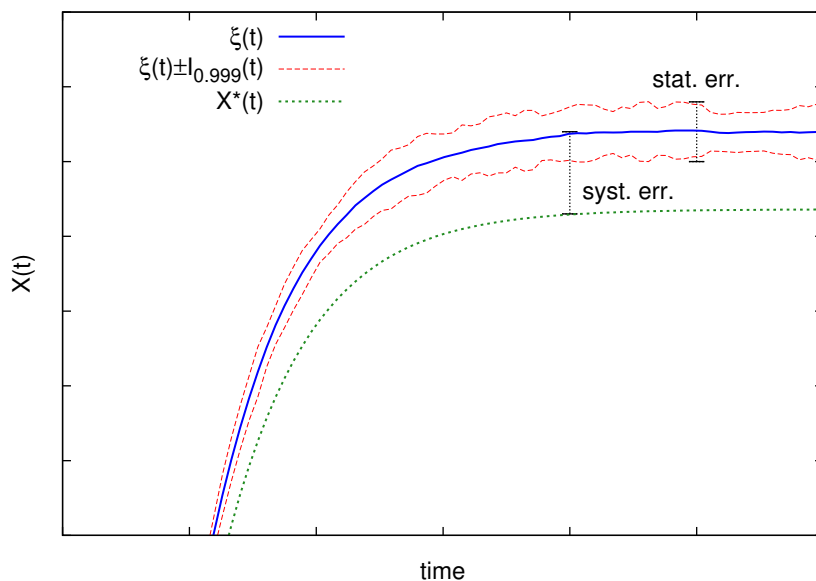


**Figure 2.4:** Temporal evolution of macroscopic quantity  $X(t)$ , showing statistical and systematic error.

These measurements will provide a basis on which to investigate the numerical properties of the stochastic algorithms developed in this work. The influence of these errors on a macroscopic property of the particle ensemble  $X(t)$  (e.g. average diameter) is illustrated in Figure 2.4.

## 2.5 Silicon nanoparticles

Knowledge of the properties of silicon has underpinned the revolution of information technology. A great deal of study has therefore been undertaken into its synthesis, purification and resultant properties. Silicon nanoparticles were first made in the late 1970's [101]. Since then, they have been the subject of considerable work towards improving their manufacture and identifying potential applications.

### 2.5.1 Manufacture

Gas-phase, laser and plasma synthesis of particles are the most common methods with which silicon nanoparticles are manufactured [88]. In general, these processes begin with silane ( $\text{SiH}_4$ ), which may be decomposed

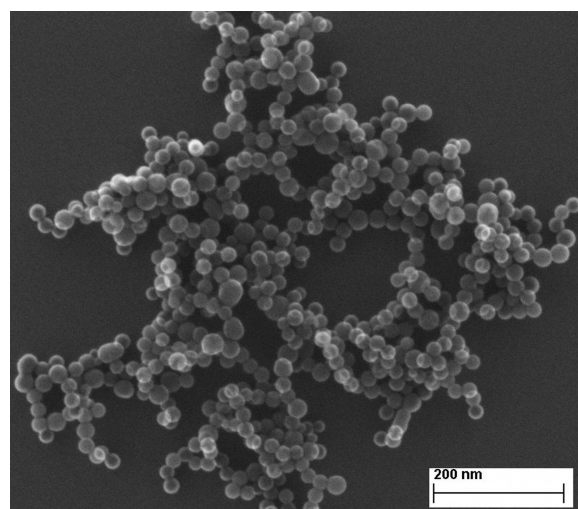


**Figure 2.5:** Highly-spherical silicon nanoparticles made in a hot-wall reactor. Reprinted from *Journal of Aerosol Science*, 41/11, Körmer, R. et al., “Aerosol synthesis of silicon nanoparticles with narrow size distribution–Part 1: Experimental investigations”, pp. 998–1007, Copyright (2010), with permission from Elsevier.

by thermal, laser or microwave radiation sources [22, 72, 103]. The decomposition of silane forms reactive silicon hydrides, which combine with each other to nucleate into silicon nanoparticles [149].

A tubular hot-wall reactor is frequently used to study silicon nanoparticles in a research environment [75, 158]. These reactors allow control of the temperature profile through the length of the reactor [161], and particles can be directly sampled from within the reactor [75]. The particle size, distribution and morphology is strongly dependent on the process conditions of the reactor, however large losses of silicon to wall-growth is often reported [75, 113]. Despite this, the product properties can be tightly controlled [56], and highly spherical particles, such as those in Figure 2.5, can be obtained.

Production of silicon nanoparticles through laser pyrolysis typically uses a CO<sub>2</sub> laser to promote silane decomposition [22, 44]. Laser heating causes rapid localised heating of the silane, leading to fast particle production. The short timescales over which particles are produced makes controlling the particle size distribution challenging. Laser ablation of solid silicon has also been identified as a means to produce nanoparticles [157].

In plasma synthesis, silane is fed into a parallel-plate reactor, where radiofrequency discharge ionises the precursor and initiates decay. A great deal of study has focused on characterising the mechanisms of silane anion formation, particle nucleation, and silicon deposition [50, 66]. Microwave reactors have also been used to generate silane plasmas [72]. The major advantage in plasma synthesis is that the particles become negatively charged, which suppresses coagulation and confines them in the plasma [88].

Once particles are produced, they can be modified in many ways. Bringing silicon particles into contact with air will cause oxidation of the particle surface, removing the Si-H bonds at the surface. Particles can be made stable in water by functionalising the surface with acrylic acid [86], or be made stable in air by replacing the hydride surface layer with hydroxide [88]. Finally, particle sizes can be reduced by etching with hydrogen fluoride and nitric acid [85].

### 2.5.2 Applications

There are two key properties of silicon nanoparticles which make them interesting to researchers. The first is photoluminescence, the emission of light due to the absorption of a photon. Early studies in silicon nanostructures observed photoluminescence of visible wavelength after excitation with UV light. It has since been confirmed to also occur through electrical excitation [88]. As such, silicon nanoparticles could make promising candidates for light-emission components. Cheng et al. [29] suggested they could be introduced into organic light-emitting diode (OLED) screens, where they could be used in future touchscreen technology.

Photoluminescent silicon nanoparticles have also been considered for medical imaging applications. Erogbogbo et al. [40] developed biocompatible luminescent silicon nanoparticles and successfully tracked them through pancreatic cancer cells. Park et al. [115] reported that silicon quantum dots exist in the body for a short time in comparison to other similar materials (e.g. gold nanoparticles or carbon nanotubes), with no evidence of toxicity.

The other property of silicon nanoparticles is its use as a semiconductor. Much study into applications of silicon nanoparticles in photovoltaics has been conducted. As the quantum confinement effects of a particle are strongly dependent on its size and structure, it may be possible to tune a photovoltaic cell to better match solar emission than in bulk material

[88]. Finally, printable semiconductor and photoluminescent inks of silicon nanoparticles have been proposed as a straightforward way of preparing next-generation circuits or displays [7].

## Chapter 3

# Choosing a particle model

*Three particle models commonly-used in the literature are compared in a detailed numerical study. The conditions under which these models differ are identified, and the effect of particle polydispersity upon each of the models is investigated. The study concludes with an analysis of the computational time required for the models.*

*Material from this chapter has been published in [91].*

The population balance equation (Equation (2.13)) describes the formation and growth of nanoparticles. When solving this equation, different assumptions can be made about the nature of the particles, and it is this level of detail which is defined as the ‘particle model’. Mathematically, the particle model is represented by the type-space.

The aerosol system to be modelled and the choice of population balance equation solution methodology define which particle model is used. The sectional methods and moment methods discussed in Sections 2.2.3 are difficult to extend to multiple internal dimensions [61] and will therefore use relatively simple particle models [47]. The stochastic particle method used in this thesis is ideal for comparing particle models, as the particle model is completely independent of the stochastic algorithm, and a type-space of any level of detail can be used.

Some of the most commonly-used particle models will now be reviewed. In early modelling attempts, particles were treated as spheres which would coalesce into larger spheres upon collision with other particles; for example, see Frenklach and Harris [48]. This corresponds to the spherical particle

model; which is a one-dimensional model tracking only the volume or some number of chemical elements in a particle.

However, not all nanoparticles are spherical [117, 139, 152]. It is very common to obtain aggregates (chemically bound collections of particles) and agglomerates (physically bound particles) [36], especially when particle growth occurs by coagulation or sintering. The surface-volume (surf-vol) particle model extends the basic spherical model by tracking the volume and total surface area of a particle [78, 165]. Another two-dimensional model providing similar information tracked the number of aggregates and the number of primary particles [116]. Such knowledge provides a basic understanding of aggregate structure of particles. The surface-volume model was also extended in the surface-volume-hydrogen model of Blanquart and Pitsch [15], which considered the number of active sites as an additional independent variable.

The surface-volume model is limited in the respect that it assumes that primary particles are monodisperse. Further, it has been identified that typical expressions used to calculate the primary particle size are not ideal [155]. Heine and Pratsinis [61] developed a sectional model to address this issue, where the polydispersity of primary particles was incorporated in a sectional model. Balancing the population of primary particles over all aggregate particles enabled the simultaneous effects of coagulation and sintering to be captured.

Even more detailed particle models have been developed. Sander et al. [136] presented a binary-tree particle model as part of a stochastic population balance model. It incorporated the full aggregate structure of soot particles, allowing for resolution of individual primary particles and their connections to other primary particles in an aggregate. This model has been extended to silica [143, 144] and silicon [92] in later studies.

Despite these advances in modelling the structure and morphology, many studies still use basic spherical or surface-volume particle models [4, 56, 76]. In this chapter, the conditions under which use of these models is appropriate will be investigated, and the conditions where their use could represent a significant over-simplification will be identified. This is accomplished using the generic stochastic population balance solver presented in Section 2.2.2.

The structure of this chapter is as follows. Section 3.1 presents the math-

ematical description of the particle models and explains how their derived properties (e.g. particle collision diameter) are calculated. Case study are presented in Section 3.2 and the implications of these studies discussed in Section 3.3.

## 3.1 Model

### 3.1.1 Type-space

This work uses a generic multicomponent description of the primary particles' chemical composition, that is:

$$p = p(\eta_1, \eta_2, \dots, \eta_n) \quad (3.1)$$

where  $p$  will contain  $\eta_i$  chemical components (e.g. number of carbon atoms). A particle  $P_q$  of index  $q$  in  $N_{\max}$  computational particles will always contain at least one primary particle  $p$ . Throughout this work, the term 'particle' will be used to refer to the computational particle  $P$ , whereas 'primary' will refer to a primary particle owned by a computational particle. For the spherical particle model, the type-space is very simple:

$$P_q = P_q(p^{(q)}) \quad (3.2)$$

Here the super-script is used to denote ownership of the primary particle  $p^{(q)}$  by computational particle  $P_q$ . The surface-volume model tracks the surface area  $S^{(q)}$  in addition to the chemical composition of primaries:

$$P_q = P_q(p^{(q)}, S^{(q)}) \quad (3.3)$$

The surface-volume model, however, assumes that primaries in a particle  $P_q$  are uniformly distributed. The ability to include polydispersity of primary particles was proposed by Sander et al. [136] in their binary-tree model. This model represents a particle as a binary tree of primary particles with connectivity stored in the non-leaf nodes:

$$P_q = P_q(p_1, p_2, \dots, p_{n_q}, \mathbf{C}^{(q)}) \quad (3.4)$$

where  $P_q$  contains  $n_q$  primary particles and  $\mathbf{C}$  is a lower-diagonal matrix representing the common surface area between two neighbouring primary particles. The form of this matrix is discussed in [136, 143, 144].

**Table 3.1:** Comparison of the derived properties of the particle models.

Property	Spherical	Surf-vol	Binary tree
type-space	$P_q(p^{(q)})$	$P_q(p^{(q)}, S^{(q)})$	$P_q(p_1, p_2, \dots, p_{n_q}, \mathbf{C}^{(q)})$
$V_q$	$\sum_{i=1}^n \frac{\eta_i M_i}{N_A \rho_i}$	$\sum_{i=1}^n \frac{\eta_i M_i}{N_A \rho_i}$	$\sum_{j=1}^{n_q} V(p_j)$
$d_{\text{sph},q}$	$\sqrt[3]{\frac{6}{\pi} V_q}$	$\sqrt[3]{\frac{6}{\pi} V_q}$	$\sqrt[3]{\frac{6}{\pi} V_q}$
$S_{\text{sph},q}$	$\pi d_{\text{sph},q}^2$	$\pi d_{\text{sph},q}^2$	$\pi d_{\text{sph},q}^2$
$S_q$	$S_{\text{sph},q}$	$S^{(q)}$	$\frac{S_{\text{sph},q}}{\bar{s}_q(1 - n_q^{-\frac{1}{3}}) + n_q^{-\frac{1}{3}}}$
$d_{\text{pri},q}$	$d_{\text{sph},q}$	$\frac{6V_q}{S_q}$	-
$\overline{d_{\text{pri},q}}$	-	-	$\frac{1}{n_q} \sum_{j=1}^{n_q} d_{\text{pri}}(p_j)$
$n_q$	1	$\frac{S_q^3}{36\pi V_q^2}$	$n_q$
$d_{\text{col},q}$	$d_{\text{sph},q}$	$\frac{1}{2} \left( d_{\text{sph},q} + \sqrt{\frac{S_q}{\pi}} \right)$	$\overline{d_{\text{pri},q}} \left[ \frac{S_q^3}{36\pi V_q^2} \right]^{\frac{1}{D_f}}$

### 3.1.2 Derived properties

The type-space of the particles allows for all other properties of the particles to be determined [143]. The volume of a primary is based on the number of chemical units  $\eta_i$  and bulk densities  $\rho_i$ :

$$v(p) = \sum_{i=1}^n \frac{\eta_i M_i}{N_A \rho_i} \quad (3.5)$$

where  $M_i$  is the molecular weight of element  $i$  and  $N_A$  is Avogadro's number. For spherical or surface-volume particles, the volume of the particle  $V_q$  is equal to that of the primary. In the binary tree model, the volume of a particle is the sum of the volume of its constituent primaries, that is:

$$V_q = V(P_q) = \sum_{j=1}^{n_q} v(p_j) \quad (3.6)$$

The derived properties of the surface-volume model have been published in [78]. Essentially, the volume and surface area  $S_q$  of a particle are used

to estimate the size of primary particles, the number of primaries and the collision diameter. These equations are summarised in Table 3.1. For the binary tree model, the derived properties are analogous to those used in previous studies [90, 136, 143]. Of key importance is the surface area:

$$S_q = \frac{S_{\text{sph},q}}{\bar{s}_q(1 - n_q^{-\frac{1}{3}}) + n_q^{-\frac{1}{3}}} \quad (3.7)$$

where  $S_{\text{sph},q}$  is the equivalent spherical surface of a sphere with the same volume as the particle  $P_q$ , and  $\bar{s}_q$  is the average sintering level between the primaries of the particle. The sintering level ( $0 \leq s \leq 1$ ) of two primary particles  $p_j$  and  $p_k$  is given by [136]:

$$s(p_j, p_k) = \frac{\frac{S_{\text{sph}}(p_j, p_k)}{C_{jk}} - 2^{-\frac{1}{3}}}{1 - 2^{-\frac{1}{3}}} \quad (3.8)$$

where  $C_{jk}$  represents the element of the common-surface matrix  $\mathbf{C}$  describing the common surface area of the two primaries  $p_j$  and  $p_k$ . For two primary particles in point contact, this initially represents the sum of their surface area. As sintering occurs, the common surface decreases until it is equal to the surface area of the sphere with the same volume as the sum of the primaries' volume,  $S_{\text{sph}}(p_j, p_k)$ . Thus, we can always write:

$$S_{\text{sph}}(p_j, p_k) < C_{jk} \leq S_{\text{sph}}(p_j) + S_{\text{sph}}(p_k) \quad (3.9)$$

The definition of sintering level implies that a spherical particle has a sintering level of 1, while two primaries in point contact (with no sintering) have a sintering level of 0. Note that the primary particle diameter described by the surface-volume model is an estimate based-on the surface area and volume. The primary particle diameter for the binary-tree model is an average within the particle, given by:

$$\overline{d_{\text{pri}_q}} = \frac{1}{n_q} \sum_{j=1}^{n_q} d_{\text{pri}}(p_j) \quad (3.10)$$

The collision diameter of a particle in the binary tree model is given by [143]:

$$d_{\text{col},q} = \overline{d_{\text{pri}_q}} \left[ \frac{S_q^3}{36 \pi V_q^2} \right]^{\frac{1}{D_f}} \quad (3.11)$$

where  $\overline{d_{\text{pri}_q}}$  is the average primary diameter (as calculated by Equation (3.10)) and  $D_f$  is the fractal dimension, assumed to be 1.8 for the present work [138]. These are summarised and compared with the derived properties of other particle models in Table 3.1.

### 3.1.3 Particle processes

The three particle models interact with several particle processes. Examples of such processes are inception (or nucleation), heterogeneous growth, coagulation and sintering. These processes are documented and mathematically described in detail in [90]. In the present work, coagulation and sintering are the two which differ most between models so are outlined here.

The rate of coagulation is calculated using the transition regime coagulation kernel (Equation (2.22)), which is a computationally efficient approximation to true Brownian coagulation [70]. In the spherical particle model, a coagulation event will form a sphere with volume equal to the sum of the coagulating spheres' volume. This is represented by the following transformation:

$$P_q(p^{(q)}) + P_r(p^{(r)}) \rightarrow P_s(p^{(q)} + p^{(r)}) \quad (3.12)$$

The addition of primary particles is equivalent to taking the sum of their component vectors:

$$\begin{aligned} p^{(q)}(\eta_1^{(q)}, \dots, \eta_m^{(q)}) + p^{(r)}(\eta_1^{(r)}, \dots, \eta_m^{(r)}) \\ = p^{(s)}(\eta_1^{(q)} + \eta_1^{(r)}, \dots, \eta_m^{(q)} + \eta_m^{(r)}) \end{aligned} \quad (3.13)$$

A similar transformation takes place for a coagulation event in the surface-volume model, except the total surface area is also conserved:

$$P_q(p^{(q)}, S^{(q)}) + P_r(p^{(r)}, S^{(r)}) \rightarrow P_s(p^{(q)} + p^{(r)}, S^{(q)} + S^{(r)}) \quad (3.14)$$

A coagulation event in the binary tree model will retain the primary particle information and connectivity of both coagulating particles:

$$\begin{aligned} P_q(p_1, \dots, p_{n_q}, \mathbf{C}^{(q)}) + P_r(p_1, \dots, p_{n_r}, \mathbf{C}^{(r)}) \\ \rightarrow P_s(p_1, \dots, p_{n_q}, p_{n_q+1}, \dots, p_{n_q+n_r}, \mathbf{C}^{(s)}) \end{aligned} \quad (3.15)$$

The common-surface matrix  $\mathbf{C}$  is changed to reflect the structure of old particles  $P_q$  and  $P_r$ , and their new connection. The process through which

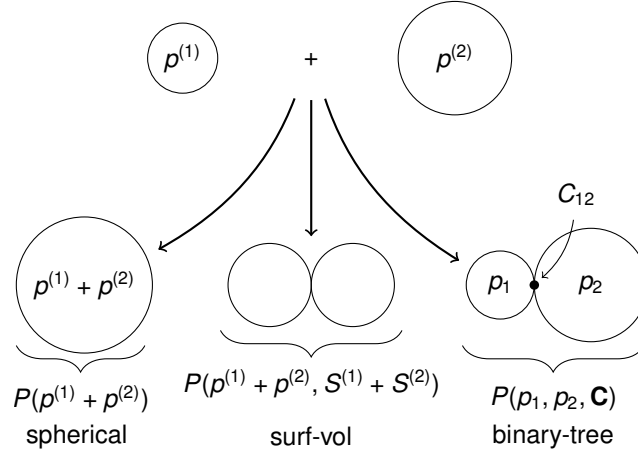


**Figure 3.1:** An illustration of different particle models' description of coagulation events

this is done is described in detail by Shekar et al. [143]. The physical interpretation of Equations (3.12)–(3.15) is illustrated in Figure 3.1.

The three models also include different descriptions of sintering. For the spherical particle model, sintering effectively occurs infinitely fast, as particles coalesce upon coagulation. For the surface-volume and binary tree models, the exponential excess surface area decay formula—as popularised by Koch and Friedlander [73]—is employed. In surface-volume model, the surface area of the whole particle is reduced:

$$\frac{\Delta S_q}{\Delta t} = -\frac{1}{\tau_S(p^{(q)})} (S_q - S_{\text{sph},q}) \quad (3.16)$$

where  $\tau_S$  is the characteristic sintering time. It is an empirical function of temperature  $T$  and diameter  $d$  which is related to the time required for two neighbouring primaries to coalesce. For the surface-volume model, it is expressed in the form [155]:

$$\tau_S(p^{(q)}) = A_S d_{\text{pri},q}^{n_S} T \exp\left(\frac{E_S}{RT}\right) \quad (3.17)$$

where  $A_S$ ,  $n_S$  and  $E_S$  are empirical parameters. These parameters are usually specific to a particular type of material and are not trivial to determine [19, 166]. Tracking of the connectivity of adjacent primary particles allows the binary tree model to sinter each connection individually. For a

single connection, the rate of sintering is given by [136]:

$$\frac{\Delta C_{jk}}{\Delta t} = -\frac{1}{\tau_S(p_j, p_k)} \left( C_{jk} - S_{\text{sph}}(p_j, p_k) \right) \quad (3.18)$$

where  $S_{\text{sph}}(p_j, p_k)$  is the equivalent spherical surface area of a particle with volume  $V_j + V_k$ . The characteristic sintering time also takes a slightly different form to account for two primaries of a different size touching:

$$\tau_S(p_j, p_k) = A_S \min [d_{\text{pri}}(p_j), d_{\text{pri}}(p_k)]^{n_S} T \exp \left( \frac{E_S}{RT} \right). \quad (3.19)$$

### 3.1.4 Average properties

In order to study the behaviour of a system of particles, it is useful to define some average quantities which describe the size and morphology of the particles and ensemble. In this thesis, the arithmetic and geometric mean of the collision and primary diameter is used. These are denoted as  $\mu_a$  and  $\mu_g$  respectively. For example, the geometric mean of the primary diameter is given by:

$$\mu_g(d_{\text{pri}}) = \left( \prod_{q=1}^{N(t)} d_{\text{pri},q} \right)^{\frac{1}{N(t)}} \quad (3.20)$$

where  $N(t)$  computational particles are in the ensemble at time  $t$ . Note that for the surface-volume model,  $\mu_g(d_{\text{pri}})$  represents the mean of the estimated primary diameter of each particle; while in the binary tree model it represents the mean of average primary diameter of each particle.

The (number-based) geometric standard deviation is also particularly useful for classifying polydispersity of particles [61]. Here, it is calculated in the context of the binary tree model for the average primary diameter as:

$$\sigma_g(\overline{d_{\text{pri}}}) = \exp \left( \sqrt{\frac{1}{N(t)} \sum_{q=1}^{N(t)} \ln \left[ \frac{d_{\text{pri},q}}{\mu_g(\overline{d_{\text{pri}}})} \right]^2} \right) \quad (3.21)$$

For the binary tree model, two estimates of  $\sigma_g(d_{\text{pri}})$  can be made. The first involves using Equation (3.21) to calculate the geometric standard deviation of the average primary diameter. The second takes the arithmetic mean of the geometric standard deviation of the primary diameter in each

particle:

$$\mu_a [\sigma_g(d_{\text{pri}})] = \frac{1}{N(t)} \sum_{q=1}^{N(t)} \exp \left( \sqrt{\frac{1}{n_q} \sum_{j=1}^{n_q} \ln \left[ \frac{d_{\text{pri},j}}{\mu_g(d_{\text{pri}})} \right]^2} \right) \quad (3.22)$$

These two estimates provide different descriptions of the geometric standard deviation of primary diameter.  $\sigma_g(\bar{d}_{\text{pri}})$  refers to the average geometric standard deviation of primary diameter across all particles. In contrast,  $\mu_a [\sigma_g(d_{\text{pri}})]$  yields information about the geometric standard deviation of primaries contained within a particle.

It should be noted that the average properties presented here are distinct from those in Section 2.4, as the former represent averages over the computational particles, and the latter over independent runs.

## 3.2 Case studies

In order to study the structure of particles simultaneously undergoing coagulation and sintering, several properties are first defined. The characteristic coagulation time  $\tau_C$  is given by [103, 168]:

$$\tau_C = \frac{1}{K^{\text{tr}} M_0} \quad (3.23)$$

where  $K^{\text{tr}}$  is the transition regime coagulation kernel evaluated for the particle ensemble under study ( $\text{m}^3/\text{s}$ ) and  $M_0$  is the zeroth moment, or particle number density ( $1/\text{m}^3$ ). For the cases in Sections 3.2.1 and 3.2.2, the initial characteristic coagulation time  $\tau_{C,i}$  is used. The characteristic times are normalised by the residence time  $\tau$ , yielding a dimensionless characteristic time.

In terms of numerical parameters, 16,384 computational particles ( $N_{\text{max}}$ ) and 8 independent runs ( $L$ ) were used to evaluate the following studies [143]. All results presented in the following sections are run-averages (Equation 2.28), with the  $\xi$  symbol neglected for clarity.

### 3.2.1 Coagulation and sintering

The three models presented in the present work use very different representations of coagulation and sintering processes. To compare the models,

a sample ensemble of monodisperse spherical particles of diameter  $d_i$  was generated. The initial characteristic coagulation time  $\tau_{C,i}$  of these particles was estimated based-on their size and number density; and the sintering time  $\tau_S$  was set to a constant value. The space of normalised coagulation time and normalised sintering time was scanned, and the resulting structures of particles analysed. Each point in this space represents a calculation for the same initialised ensemble of particles where only coagulation and sintering could operate at a specified rate.

The results of this analysis are presented in Figure 3.2, where the collision diameter (normalised by initial particle diameter) is plotted against the dimensionless sintering and initial coagulation time. The collision diameter was chosen as it is a strong function of type-space and is a good descriptor of overall aggregate size.

It is unsurprising that the models converge for high values of  $\tau/\tau_S$ . This corresponds to instantaneous sintering (or coalescence) of particles upon collision. It is interesting to observe that for some combinations of  $(\tau/\tau_S, \tau/\tau_{C,i})$  the particles obtained through the binary tree model are larger; whereas for other combinations they appear smaller than the surface-volume model. Indeed, an intersection between these surfaces defines a line at which the particles obtained through both models are identical. This is shown in more detail in Figure 3.3, where the contours corresponding to the intersection of the binary tree and surface-volume models, and  $\pm 5\%$  relative difference between the two are plotted. Specifically, the 5% error shading refers to the conditions under which:

$$0.95 \leq \frac{\mu_g(d_{\text{col}})^{\text{bin-tree}} - \mu_g(d_{\text{col}})^{\text{surf-vol}}}{\mu_g(d_{\text{col}})^{\text{bin-tree}}} \leq 1.05 \quad (3.24)$$

Four zones in this figure are identified, corresponding to different types of particles. Particles obtained in the spherical zone sinter sufficiently quickly to coalesce into spherical particles. In this zone, the all particle models effectively reduce to the spherical particle model; and there is no benefit gained from tracking the additional structural detail of particles.

In the near-spherical zone, aggregates containing few primary particles are formed, either due to a fast sintering rate or a slow coagulation rate. Figure 3.2 illustrates that the particles predicted by the binary tree model have a larger collision diameter, corresponding to smaller primary particles. The reason for this can be understood by considering the derived properties

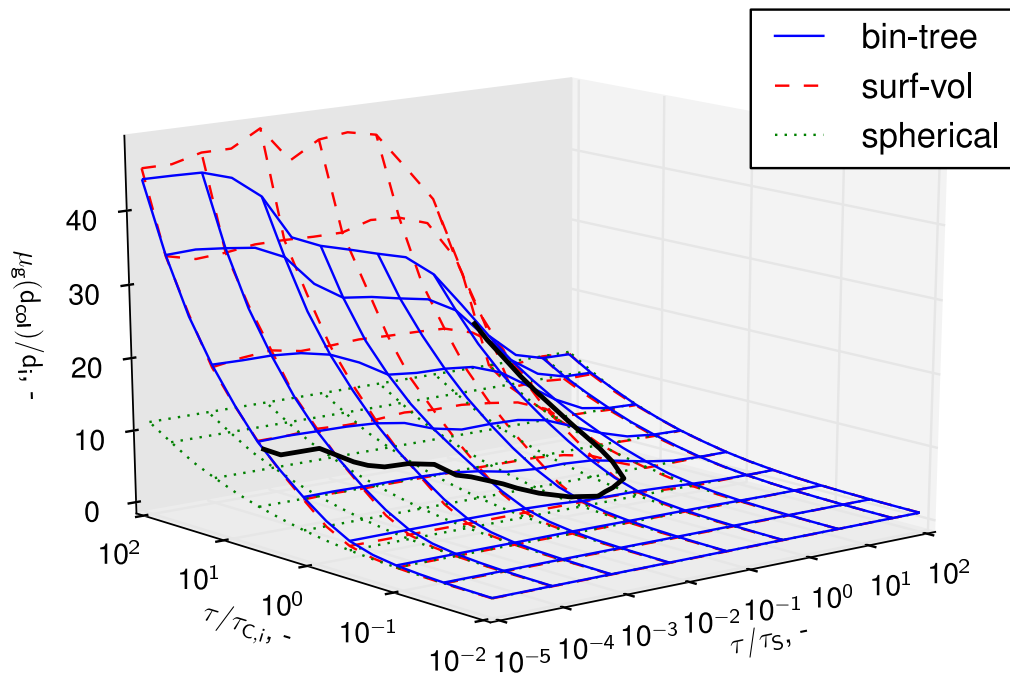


**Figure 3.2:** Comparison of the normalised geometric mean collision diameter as a function of dimensionless coagulation and sintering time for each of the three particle models. The thick line depicts the intersection of the binary tree and surface-volume model predictions.

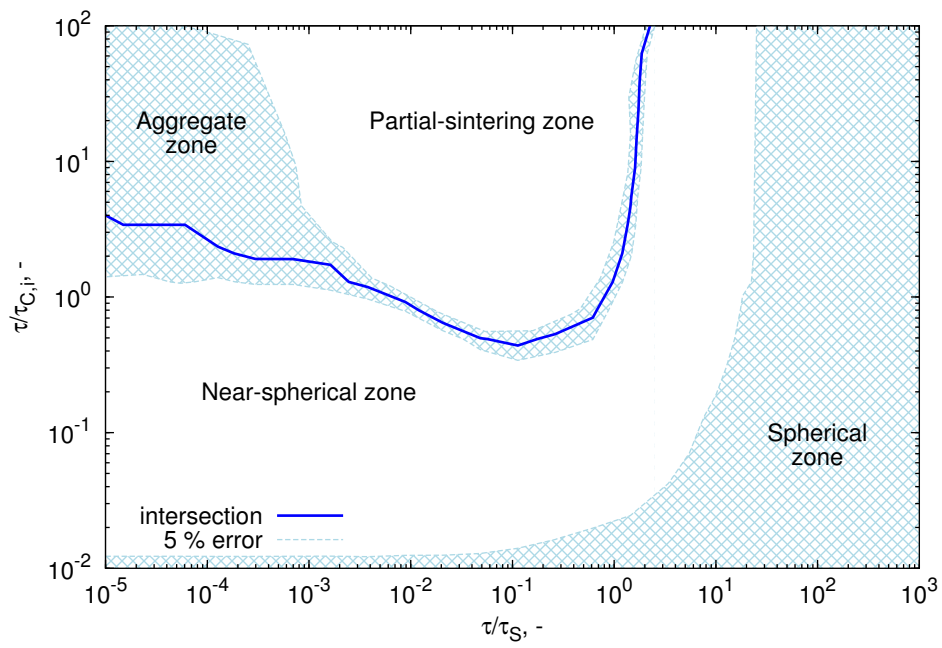


**Figure 3.3:** A contour plot depicting where the binary tree model is equivalent to the surface-volume model. The shading corresponds to within 5% deviation (with respect to collision diameter) of the surface-volume model from the binary tree model.

of the particle models, in particular the expressions for collision diameter. It is shown in Appendix A.1 that, for coagulation of similarly-sized particles, the surface-volume model will under-estimate the predictions of the binary-tree model to a maximum of 10% difference. While this deviation is small, it causes potentially large changes in the rate of coagulation (rate  $\propto d_{\text{col}}^2$  in the free-molecular regime), thus increasing the maximum error.

In the partial-sintering zone, particles coagulate to form partially-sintered aggregates with more than 2–3 primary particles. Here, the surface-volume model over-predicts the results of the binary tree model. The reason for this can be understood by considering the sinterable surface area of an aggregate. As each connection node in the binary tree model is individually sintered (according to Equation (3.18)) there must always be more sinterable surface area in an aggregate described by the binary tree model than one described by the surface-volume model. This is mathematically demonstrated in Appendix A.2. If sintering occurs within the same characteristic time, the model with more sinterable surface area will sinter the particles faster (Equations (3.16) and (3.18)). In this case, this causes the binary tree model to predict the formation of smaller aggregates with larger primaries.

The intersection of the partial-sintering and near-spherical zones corresponds to the point where primaries are uniformly sized within an aggregate. As  $\tau/\tau_S \rightarrow 0$  the binary tree model becomes identical to the surface-volume model: aggregates are composed of un-sintered monodisperse primary particles (the aggregate zone).

### 3.2.2 Effect of polydispersity

The study in the previous section highlights that under certain conditions, the surface-volume model yields aggregate particles with approximately the same size as the binary tree model. This, however, was determined for an initially monodisperse ensemble of particles (initial geometric standard deviation  $\sigma_g(d_i) = 1.0$ ). The purpose of this case study is to investigate how polydispersity can affect model performance, under conditions where the surface-volume and binary-tree models are equivalent for monodisperse particles. To investigate this, a point on the intersection line of Figure 3.3 was chosen ( $\tau/\tau_S = 1.4$ ,  $\tau/\tau_{C,i} = 5.0$ ) and ensembles initialised with spherical particles of increasing polydispersity (up to  $\sigma_g(d_i) = 3.0$ ). The results are given in Figure 3.4.

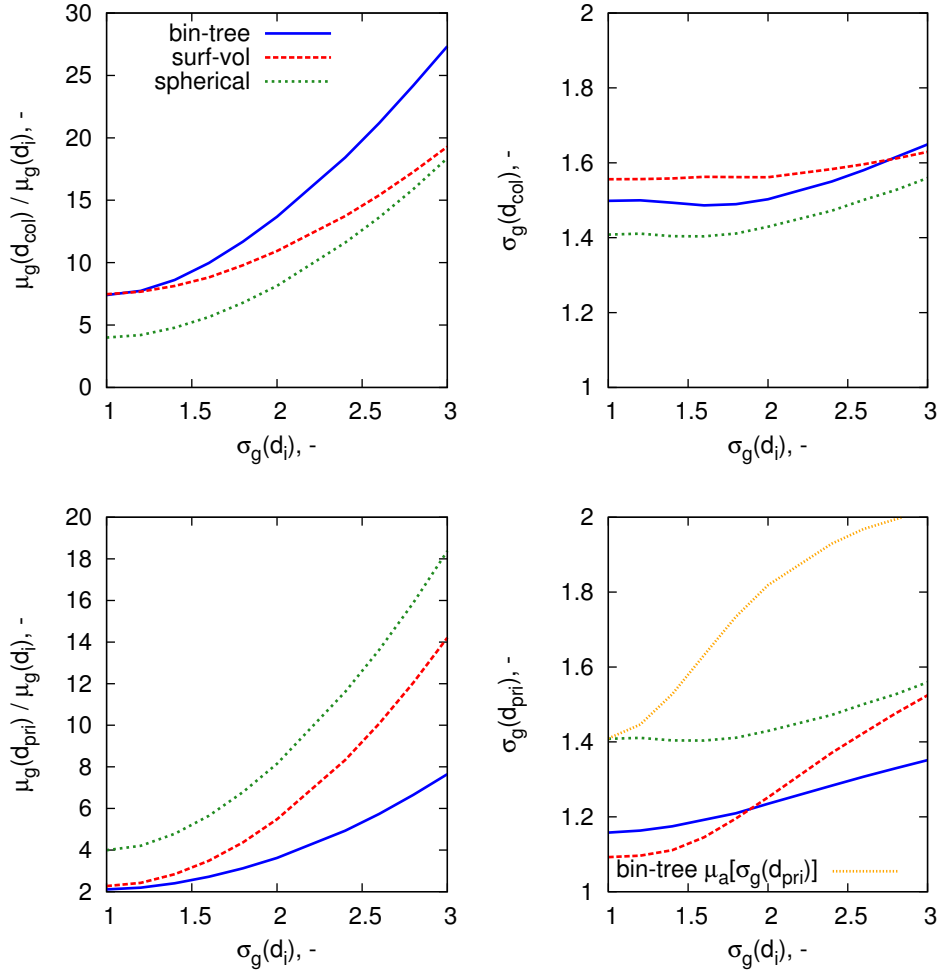


**Figure 3.4:** Effect of initial polydispersity,  $\sigma_g(d_i)$ , on morphology of particles. Shown are the normalised geometric mean  $\mu_g$  and standard deviation  $\sigma_g$  of the collision and primary diameter. These were generated for  $\tau/\tau_S = 1.4$ ,  $\tau/\tau_{C,i} = 5.0$ , on the intersection line of Figure 3.3.

It is evident that the the surface-volume and binary-tree models perform comparably with  $\sigma_g(d_i) < 1.5$ . Under these conditions, there appears to be good agreement with the geometric mean collision and primary diameter and a small difference in geometric standard deviation of both. Beyond  $\sigma_g(d_i) = 1.5$ , the binary-tree model appears to predict larger aggregates with smaller primaries than the surface-volume model. This is attributed to the phenomenon discussed in Section 3.2.1 for the prediction of collision diameter in the near-spherical zone.

It is also interesting to observe that for the binary tree model, the standard deviation of the average primary diameter is significantly smaller than the average standard deviation of the primary diameter. This suggests that the local polydispersity within a particle can often be quite different to the polydispersity of the ensemble. The right panels of Figure 3.4 show that the spherical particle model yields ensembles with  $\sigma_g(d) \approx 1.4$  for  $\sigma_g(d_i) > 1.5$ . This indicates that the system has reached the self-preserving particle size distribution [153].

In summary, this case study demonstrates that the prediction of the properties of an ensemble of polydisperse particles undergoing coagulation and sintering is strongly dependent on choice of particle model. Highly polydisperse  $\sigma_g(d_i) > 1.5$  systems are poorly described by the spherical or surface-volume models where coagulation and sintering occur on similar timescales.

### 3.2.3 Computational resources

While the binary tree model is capable of providing more information on particle structure and morphology, this comes at the cost of increased computational resources required. In order to capture all particle structure zones, a ‘slice’ across Figure 3.3 at  $\tau/\tau_{C,i} = 10$  is taken, and the computational time required per run plotted in Figure 3.5. Calculations were conducted on a SGI Altrix Cluster with nodes composed of two 3.00 GHz quad-core Intel Harpertown processors and 8 GB of RAM.

In the stochastic formulation of the population balance, it is evident that the surface-volume and spherical particle models require almost the same computational time, and this time is independent of the sintering rate. This is unsurprising, given that the additional effort required to adjust a particle’s surface area after a sintering event is minimal: it merely requires calculation of Equation (3.16).

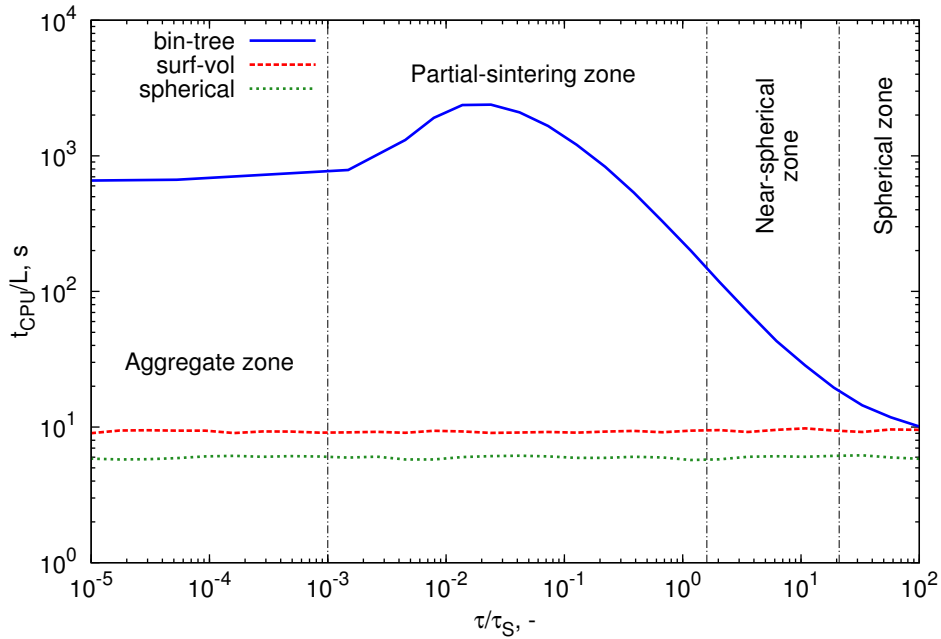


**Figure 3.5:** Comparison of computational time ( $t_{CPU}$ ) required per run for  $\tau/\tau_{C,i} = 10$  to calculate  $\tau = 0.5$  s of process time.

The three models require the same computational time when spherical particles are obtained. Only when coagulation becomes important (relative to sintering) does the binary-tree model require more time, and in this case it requires orders of magnitude more. In the partial-sintering zone, particles containing more than one primary experience ‘merge’ events, where two distinct primaries are combined into one due to sintering [143]. These events alter the binary tree structure and as such, for large trees (i.e. particles with many primaries), more time is required to regenerate the tree structure after a node is lost. This phenomenon is responsible for the peak in computational time in the partial-sintering zone.

### 3.3 Conclusions

This chapter has presented the mathematical formulation of particle models commonly used in aerosol dynamics of nanoparticles. A detailed numerical study was conducted in order to understand under which conditions these models differ. Starting from a set of identical conditions, the predictions

of the resulting average properties of the particle ensemble were compared for each of the particle models. It was identified that under certain circumstances, all models were equivalent to a spherical particle model.

Outside of this range, the performance of the popular and computationally inexpensive surface-volume model with respect to a model which tracks full aggregate structure (binary-tree model) was evaluated. The two models gave similar results (to within a small error margin) where sintering was slow. However, where coagulation and sintering occurred on a similar timescale, the models predicted substantially different results. Further, the spherical and surface-volume particle models were shown to incur a large error margin where the coagulating ensemble was highly polydisperse.

There is still considerable scope for further investigation of the behaviour of particle models. Heterogeneous growth processes are well-documented contributors to rounding of particles [83, 144] and have not been explicitly addressed in the present work. Further, only the most popular version of the surface-volume model has been used, when alternative two-dimensional formulations [61, 116] and different expressions for derived properties [155] exist.

As many population balance models use some degree of fitting or parameter estimation [27, 92, 142], the error in use of a ‘simple’ model will be reflected in the parameters obtained through the fitting procedure. The present work highlights that the choice of particle model *does* matter, and that a target modelling system should be well-characterised experimentally before proceeding to modelling.

## Chapter 4

# A new coagulation kernel for stochastic weighted algorithms

*The transition regime coagulation kernel is adapted for use with stochastic weighted algorithms (SWAs). A numerical study into use of the new kernel with a multidimensional silica particle model is conducted, and the convergence properties of SWAs are evaluated.*

*Material from this chapter has been published in [93].*

The key challenge in solving the population balance equations with a stochastic particle method is accounting for the coagulation mechanism. The Direct Simulation Algorithm (DSA)—introduced in [37]—was developed to solve the Smoluchowski coagulation equation through the technique of fictitious jumps and majorant kernels.

In direct simulation, every computational particle in the ensemble represents the same number of real particles. In basic implementations of DSA, coagulation events deplete the ensemble until there is only one computational particle remaining in the ensemble. To avoid this, the ensemble may be duplicated when it is below 50% capacity [81]. Even when extended to avoid computational particle depletion, DSA produces statistically noisy estimates of the concentrations of physically rare particles and other associated quantities [34, 122]. This is usually overcome by computationally expensive changes in the numerical parameters, for example, by increasing the number of computational particles in the ensemble [122].

To avoid these issues, stochastic weighted algorithms can be used [38,

74, 122, 134, 164]. These methods have been presented in various forms such as the Mass Flow Algorithm (MFA) [38, 54, 98, 99, 155] and the algorithms developed in [59, 170]. Stochastic weighted algorithms differ from direct simulation and constant-number methods in that coagulation events do not reduce the number of computational particles. Instead, simulated coagulations in the SWAs adjust the statistical weight that is attached to each computational particle. This statistical weight is proportional to the number of physical particles represented by the computational particle.

A recent paper gave a comprehensive review of present adaptations of SWAs [122]. It also gave the general formulation of weighted particle methods. This framework allowed for the development of general weighting rules which describe how the statistical weights are adjusted during coagulation. Further, it assumed a general form of the coagulation kernel and formulated this in terms of majorant techniques: an important method of reducing computational costs [37, 121].

The majority of previous studies of SWAs presented either used a simple spherical particle model [33, 34, 133] or a simple coagulation kernel for which an analytical solution to the population balance can be found [122, 170]. In one case, it was suggested that discrepancies with experimental results were a product of not using a coagulation kernel valid across the full range of Knudsen numbers [98].

In the previous chapter, the importance of using detailed particle models—especially where coagulation and sintering operate on similar timescales—was highlighted. Further, it has been previously identified that SWAs are particularly useful when extended to spatially inhomogeneous systems [57, 69, 118]. Thus, if stochastic methods are to be used to model systems with detailed type-space particle models, the numerical behaviour of these methods must be investigated. This will be achieved by extending the numerical studies on a silica particle model, conducted by Shekar et al. [143].

The structure of this chapter is as follows. In Section 4.1, the stochastic particle method used to solve the population balance equation is outlined. Section 4.2 shows how to implement the stochastic weighted algorithm for the transition regime coagulation kernel, and Section 4.3 gives the numerical studies used to test this system. The efficiency and convergence of the SWAs is discussed in Section 4.4 and the chapter is concluded with a critical analysis of these methods.

## 4.1 Model

A fully-coupled gas-phase and particle model is used to simulate the formation of silica from tetraethoxysilane. The kinetic model describing the gas-phase decomposition is described in [126, 142] and consists of 58 reversible gas-phase reactions among 27 chemical species.

### 4.1.1 Type-space

The binary-tree model presented in Section 3.1 is adapted here to the particular case of silica. A detailed mathematical formulation of this model's type-space is given in [143], however a brief overview of its salient features is presented here. Primary particles  $p$  are represented as:

$$p_x = p_x(\eta_{\text{Si}}, \eta_{\text{O}}, \eta_{\text{OH}}) \quad (4.1)$$

where  $\eta_{\text{Si}}$  is the number of silicon atoms,  $\eta_{\text{O}}$  is the number of oxygen (non-OH) atoms and  $\eta_{\text{OH}}$  is the number of OH units. Particles are represented as:

$$P_q = P_q(p_1, \dots, p_{n_q}, \mathbf{C}^{(q)}) \quad (4.2)$$

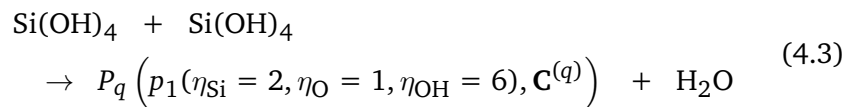
where particle  $P_q$  contains  $n_q$  primary particles. As the particle model tracks the number of chemical units of each primary and the aggregate structure, it is able to provide detailed information about the nature of a single silica particle.

### 4.1.2 Particle processes

In this model, particles may be created and changed through several different processes. The implementation of these processes in the framework of the stochastic weighted algorithm is described in Section 4.2.2.

#### Inception

The collision of two gas-phase  $\text{Si}(\text{OH})_4$  monomers yields a particle with an initial state given by  $p_1(\eta_{\text{Si}} = 2, \eta_{\text{O}} = 1, \eta_{\text{OH}} = 6)$ . This occurs through the reaction:



where the newly-incepted particle is denoted by  $P$ . Their rate of formation is based on the transition coagulation kernel:

$$R_{\text{incep}} = \frac{1}{2} K^{\text{tr}} (\text{Si}(\text{OH})_4, \text{Si}(\text{OH})_4) N_{\text{A}}^2 c_{\text{Si}(\text{OH})_4}^2 \quad (4.4)$$

where  $K^{\text{tr}} (\text{Si}(\text{OH})_4, \text{Si}(\text{OH})_4)$  is the transition kernel as applied to  $\text{Si}(\text{OH})_4$  monomers,  $N_{\text{A}}$  is Avogadro's constant and  $c_{\text{Si}(\text{OH})_4}$  is the gas-phase concentration of  $\text{Si}(\text{OH})_4$ .

### Coagulation

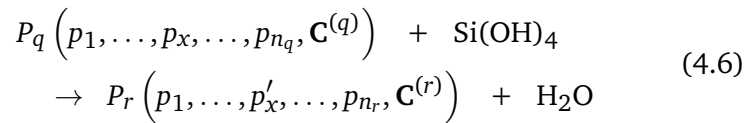
The collision and sticking of two silica particles is referred to as coagulation. The coagulation of particles  $P_q$  and  $P_r$  is represented by the following change to the particles' state:

$$\begin{aligned} P_q (p_1, \dots, p_{n_q}, \mathbf{C}^{(q)}) + P_r (p_1, \dots, p_{n_r}, \mathbf{C}^{(r)}) \\ \rightarrow P_s (p_1, \dots, p_{n_q}, p_{n_q+1}, \dots, p_{n_q+n_r}, \mathbf{C}^{(s)}) \end{aligned} \quad (4.5)$$

The matrix  $\mathbf{C}$  is transformed to include the connectivity of the old particles and that of the new point-connection [143]. The rate of coagulation is calculated using the transition coagulation kernel.

### Surface reaction

Surface reactions may occur when a  $\text{Si}(\text{OH})_4$  monomer reacts with an -OH site on the surface of a primary particle in a fashion analogous to inception. This alters the composition of the particle in the following manner:



where  $n_q = n_r$ . A primary  $p_x$  is uniformly selected and transformed according to:

$$p_x(\eta_{\text{Si}}, \eta_{\text{O}}, \eta_{\text{OH}}) \rightarrow p'_x(\eta_{\text{Si}} + 1, \eta_{\text{O}} + 1, \eta_{\text{OH}} + 2) \quad (4.7)$$

The common surface matrix ( $\mathbf{C}$ ) is changed by a surface reaction event ( $\mathbf{C}^{(q)} \rightarrow \mathbf{C}^{(r)}$ ) on  $p_x$  according to the following equation:

$$C'_{xy} = \begin{cases} 0 & p_x, p_y \text{ are non-neighbouring} \\ C_{xy} + \frac{2\Delta v \sigma_{\text{SR}}}{d_{\text{pri}}(p_x)} & p_x, p_y \text{ are neighbours} \end{cases} \quad (4.8)$$

where  $\Delta v$  is the volume element resulting from addition of mass and  $\sigma_{\text{SR}}$  is the surface-rounding factor, a smoothing factor such that  $0 \leq \sigma \leq 2$  [137].  $C_{xy}$  represents the element of the common-surface matrix  $\mathbf{C}$  which describes the common surface area of the two primaries  $p_x$  and  $p_y$ . The rate of surface reaction is proportional to the concentration of  $\text{Si(OH)}_4$  precursor and the number of OH sites on the particle surface:

$$R_{\text{surf}}(P_q) = A_{\text{surf}} \exp\left(-\frac{E_A}{RT}\right) \eta_{\text{OH}}(P_q) N_A c_{\text{Si(OH)}_4} \quad (4.9)$$

where  $A_{\text{surf}}$  and  $E_A$  are the gas-phase Arrhenius constants.

### Sintering

Neighbouring primary particles may sinter with each other according to the excess surface area decay formula popularised by Koch & Friedlander [73]:

$$\frac{\Delta C_{xy}}{\Delta t} = -\frac{1}{\tau_S(p_x, p_y)} (C_{xy} - S_{\text{sph}}(p_x, p_y)) \quad (4.10)$$

where  $S_{\text{sph}}(p_x, p_y)$  is equivalent surface area of primaries  $p_x$  and  $p_y$ . Here, a viscous-flow model is used to describe the characteristic sintering time  $\tau_S$  as a function of diameter and temperature:

$$\tau_S(p_x, p_y) = A_S \min [d_{\text{pri},x}, d_{\text{pri},y}] \exp\left(\frac{E_S}{T} \left[1 - \frac{d_{\text{p,min}}}{\min [d_{\text{pri},x}, d_{\text{pri},y}]} \right]\right) \quad (4.11)$$

where  $A_S$ ,  $E_S$  and  $d_{\text{p,min}}$  are empirical constants obtained from model-fitting [142]. The degree of sintering is measured by the sintering level parameter [136]:

$$s(p_x, p_y) = \frac{\frac{S_{\text{sph}}(p_x, p_y)}{C_{xy}} - 2^{-\frac{1}{3}}}{1 - 2^{-\frac{1}{3}}}. \quad (4.12)$$

where  $S_{\text{sph}}(p_x, p_y)$  is the surface area of the sphere with volume equal to the sum of the primaries' volume.

When the sinter process is called, the sintering level,  $s$ , of the neighbouring primaries is first checked against the coalescence criterion. If

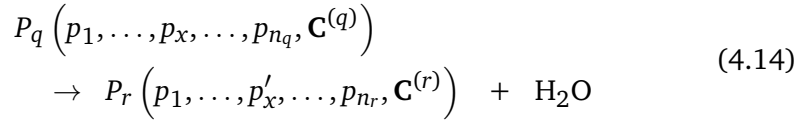
the sintering level is greater than 0.95, the particles are merged; otherwise, the particles are sintered according equation (4.10) for time  $\Delta t_{\text{sinter}}$  with

$$\Delta t_{\text{sinter}} = t - t_{\text{last update}} \quad (4.13)$$

where  $t_{\text{last update}}$  was the last time the sintering characteristics of the particle were updated. Sintering also results in the release of water, the amount of which, like surface reaction, is proportional to the particle's statistical weight.

### Intra-particle reaction

The -OH units on the surface of a primary particle may also react with each other to release water. A particle is transformed by a intra-particle reaction as:



where  $n_q = n_r$ .  $\mathbf{C}$  is altered in the same manner as for surface reaction. A primary  $p_x$  is uniformly selected and adjusted by:

$$p_x(\eta_{\text{Si}}, \eta_{\text{O}}, \eta_{\text{OH}}) \rightarrow p'_x(\eta_{\text{Si}}, \eta_{\text{O}} + 1, \eta_{\text{OH}} - 2) \quad (4.15)$$

The rate of intra-particle reaction is calculated for each particle such that the Si:O ratio tends to 1:2 as  $t \rightarrow \infty$ . It is mathematically described by the difference between the surface reaction rate and the whole-particle sintering rate:

$$R_{\text{int}}(P_q) = R_{\text{surf}}(P_q) - \frac{\eta_{\text{OH}}(P_q)}{2 S(P_q)} \left[ \sum_{x,y=1}^{n_q} \frac{C_{xy} - S_{\text{sph}}(p_x, p_y)}{\tau_{\text{S}}(p_x, p_y)} \right] \quad (4.16)$$

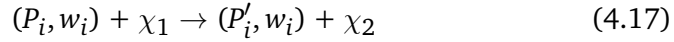
The reader is referred to [143] for the derivation and explanation of this formula.

## 4.2 Development of stochastic weighted algorithms

In stochastic weighted algorithms, computational particles are described by a type  $P_i$  and a statistical weight  $w_i$ . The physical concentration of particles of type  $P_i$  is given by  $w_i/V_{\text{smp}}$ .

### 4.2.1 Linear particle processes

While the rate expressions of linear particle processes such as inception and surface reaction remain unchanged in this weighted particle method [122], the interaction of these with the gas-phase must be carefully considered. A process which removes one molecule of  $\chi_1$  from the gas-phase and release one molecule of  $\chi_2$  into the gas-phase can be written as:



The amount of  $\chi_1$  removed ( $\Delta c_{\chi_1}$ ) and  $\chi_2$  added is proportional to the statistical weight of the particle  $w_i$  and the scaling factor  $V_{\text{smp}}$ , that is:

$$\Delta c_{\chi_1} = -\frac{w_i}{N_A V_{\text{smp}}} \quad (4.18)$$

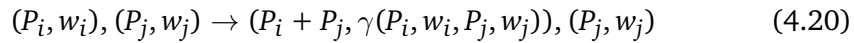
where  $V_{\text{smp}}$  refers to the computational sample volume, and:

$$\Delta c_{\chi_2} = \frac{w_i}{N_A V_{\text{smp}}} \quad (4.19)$$

Note that the statistical weight  $w_i$  remains unchanged throughout this process. Particles are created in the population balance with weight  $w_i = 1.0$  where inception occurs.

### 4.2.2 Coagulation process

Coagulation events in the SWA are asymmetric [38]. An ordered pair of particles  $(P_i, w_i)$  and  $(P_j, w_j)$  coagulate at rate  $K(P_i, P_j)w_j$  such that:



The computational particle  $(P_j, w_j)$  is unaffected by the simulated coagulation event, but the new particle with index  $i$  is constructed using  $(P_j, w_j)$ . This applies to the new type  $P_i + P_j$  and the new statistical weight, which is calculated with the weight transfer function  $\gamma$  [122].

In the stochastic simulation of a coagulation process, the total jump rate  $R$  for coagulation using the direct simulation algorithm is given by [121]:

$$R = \frac{1}{2} \sum_{i \neq j}^{N(t)} \frac{K(P_i, P_j)}{V_{\text{smp}}} \quad (4.21)$$

where  $N(t)$  is the number of stochastic particles in the ensemble at time  $t$ . When a weighted particle method is used, the jump rate is given by

$K(P_i, P_j)w_j$  and coagulation is no longer symmetric [122], so the total rate expression is modified to:

$$R = \sum_{i \neq j}^{N(t)} \frac{K(P_i, P_j)w_j}{V_{\text{smp}}} \quad (4.22)$$

The function  $K(P_i, P_j)$  represents the physics of the coagulation process and is dependent on characteristics of the particle pair and the chemical conditions of the surroundings. The transition kernel (Equation (2.22)) is a popular choice as it approximates the more detailed Fuchs Interpolation Formula and is valid across a wide range of Knudsen numbers [70, 127].

The implementation of the transition kernel within direct simulation is explained in detail in [121]. Of central importance is the use of majorants as they provide computationally efficient approximations of the true kernel such that  $K \leq \hat{K}$ . In the context of SWAs, the majorant kernel  $\hat{K}$  is written:

$$\hat{K}(P_i, w_i, P_j, w_j) = \hat{K}(P_i, P_j) w_j \quad (4.23)$$

To adapt the transition kernel to weighted methods, the majorant techniques of [122] are used. Provided the coagulation kernel satisfies:

$$\begin{aligned} \hat{K}(P_i, w_i, P_j, w_j) \leq & h_1^{(1)}(P_i, w_i) h_2^{(1)}(P_j, w_j) \\ & + h_1^{(2)}(P_i, w_i) h_2^{(2)}(P_j, w_j) \\ & + \dots + h_1^{(N_h)}(P_i, w_i) h_2^{(N_h)}(P_j, w_j) \end{aligned} \quad (4.24)$$

where  $h_i^{(j)}$  is part of an upper bound for  $\hat{K}$  and  $N_h$  is the number of terms in the factorised expression, the majorant rate can be factorised as:

$$\sum_{i,j=1}^{N(t)} \hat{K} \leq \lambda_1^{(1)} \lambda_2^{(1)} + \lambda_1^{(2)} \lambda_2^{(2)} + \dots + \lambda_1^{(N_h)} \lambda_2^{(N_h)} \quad (4.25)$$

where:

$$\lambda_l^{(k)} = \sum_{i=1}^{N(t)} h_l^{(k)}(P_i, w_i), \quad k, l = 1, 2, \dots, N_h \quad (4.26)$$

The quantities  $h_l^{(k)}(P_i, w_i)$  are stored in a binary tree which enables rapid calculation of the sums  $\lambda_l^{(k)}$  [54, 122]. They are also used to select the pair of particles for a coagulation event: more information on such processes is given in [54]. To apply this formulation to the transition kernel, it needs to be considered separately as its two components.

### Free-molecular kernel

The free-molecular kernel is given in Equation (2.23). In this chapter, it will be written as:

$$K^{\text{fm}}(P_i, P_j) = \alpha \left( \frac{1}{m_i} + \frac{1}{m_j} \right)^{\frac{1}{2}} (d_i + d_j)^2 \quad (4.27)$$

where the constant  $\alpha$  is given by:

$$\alpha = 2.2 \sqrt{\frac{\pi k_B T}{2}} \quad (4.28)$$

This is decomposed into its majorant rate form  $\hat{K}^{\text{fm}}(P_i, P_j)$  to allow for efficient jump rate calculation:

$$\hat{K}^{\text{fm}}(P_i, P_j) = \alpha k_{\text{maj}} \left( \frac{1}{\sqrt{m_i}} + \frac{1}{\sqrt{m_j}} \right) (d_i^2 + d_j^2) \quad (4.29)$$

where  $k_{\text{maj}}$  is the majorant rate scaling factor ( $k_{\text{maj}} = 2.0$ ), necessary to satisfy the inequality  $K^{\text{fm}} \leq \hat{K}^{\text{fm}}$  [53]. To calculate the total majorant rate,  $\sum_{i \neq j} \hat{K}^{\text{fm}}(P_i, P_j) w_j$  must be calculated and split into the individual jump terms. Using Equation (4.29), we obtain:

$$\begin{aligned} \sum_{i \neq j} \hat{K}^{\text{fm}}(P_i, P_j) w_j = & \\ & \alpha k_{\text{maj}} \left\{ (N(t) - 1) \sum d_i^2 m_i^{-\frac{1}{2}} w_i \right. \\ & + \left[ \sum d_i^2 \sum m_i^{-\frac{1}{2}} w_i - \sum d_i^2 m_i^{-\frac{1}{2}} w_i \right] \\ & + \left[ \sum d_i^2 w_i \sum m_i^{-\frac{1}{2}} - \sum d_i^2 m_i^{-\frac{1}{2}} w_i \right] \\ & \left. + \left[ \sum d_i^2 m_i^{-\frac{1}{2}} \sum w_i - \sum d_i^2 m_i^{-\frac{1}{2}} w_i \right] \right\} \quad (4.30) \end{aligned}$$

The indices are neglected here for clarity, however all sums act from  $i = 1$  to  $N(t)$ . For the free-molecular kernel, there are four  $\lambda_i^{(1)} \lambda_i^{(2)}$  terms, giving  $N_h = 4$ . Note that a  $\sum d_i^2 m_i^{-\frac{1}{2}} w_i$  term is subtracted from the other terms to remove self-coagulations. The majorant jump rate of free-molecular coagulation is therefore given by:

$$\hat{R}^{\text{fm}} = \sum_{i \neq j} \frac{\hat{K}^{\text{fm}}(P_i, P_j) w_j}{V_{\text{smp}}} \quad (4.31)$$

### Slip-flow kernel

The slip flow kernel from Equation (2.24) is written in this chapter as:

$$K^{\text{sf}}(P_i, P_j) = \beta_1 \left( \frac{1}{d_i} + \frac{1}{d_j} + \beta_2 \left[ \frac{1}{d_i^2} + \frac{1}{d_j^2} \right] \right) (d_i + d_j) \quad (4.32)$$

where  $\beta_1$  and  $\beta_2$  are constants, expressed as:

$$\beta_1 = \frac{2k_B T}{3\mu}, \quad \beta_2 = 1.257(2\sigma) \quad (4.33)$$

The slip-flow kernel does not need a majorant due to its simple form [121]. Thus, the sum can be directly expanded:

$$\begin{aligned} \sum_{i \neq j} K^{\text{sf}}(P_i, P_j) w_j = & \\ & \beta_1 \left\{ 2(N(t) - 1) \sum w_i \right. \\ & + \left[ \sum d_i \sum d_i^{-1} w_i - \sum w_i \right] \\ & + \left[ \sum d_i w_i \sum d_i^{-1} - \sum w_i \right] \\ & + \beta_2 \left( (N(t) - 1) \sum d^{-1} w_i \right. \\ & + \left[ \sum d_i \sum d_i^{-2} w_i - \sum d^{-1} w_i \right] \\ & + \left[ \sum d_i w_i \sum d_i^{-2} - \sum d^{-1} w_i \right] \\ & \left. \left. + \left[ \sum d_i^{-1} \sum w_i - \sum d^{-1} w_i \right] \right) \right\} \end{aligned} \quad (4.34)$$

The jump rate of slip-flow coagulation is thus given by:

$$R^{\text{sf}} = \sum_{i \neq j}^{N(t)} \frac{K^{\text{sf}}(P_i, P_j) w_j}{V_{\text{smp}}} \quad (4.35)$$

### Particle selection algorithm

Equations (4.30) and (4.34) comprise the majorant rate expression for the ‘weighted majorant transition kernel’:

$$\hat{K}(P_i, P_j) w_j = \begin{cases} \sum_{i \neq j} \hat{K}^{\text{fm}}(P_i, P_j) w_j & \text{if } \hat{R}^{\text{fm}} < R^{\text{sf}} \\ \sum_{i \neq j} K^{\text{sf}}(P_i, P_j) w_j & \text{if } \hat{R}^{\text{fm}} \geq R^{\text{sf}} \end{cases} \quad (4.36)$$

In a similar vein to [53], these expressions can be thought of as sums of individual rate terms. For example, Equation (4.30) can be rewritten as:

$$\hat{K}^{\text{fm}}(P_i, P_j)w_j = \hat{K}^{\text{fm},1} + \hat{K}^{\text{fm},2} + \hat{K}^{\text{fm},3} + \hat{K}^{\text{fm},4} \quad (4.37)$$

where, as an illustration, the first free-molecular jump rate term is given by:

$$\hat{K}^{\text{fm},1} = \alpha k_{\text{maj}}(N(t) - 1) \sum_{i=1}^{N(t)} d_i^2 m_i^{-\frac{1}{2}} w_i \quad (4.38)$$

Comparing Equation (4.30) to Equation (4.25), we see that each of these individual rate terms  $\hat{K}^{(\text{fm},i)}$  is composed of two parts  $\lambda_1^{(\text{fm},1)}$   $\lambda_2^{(\text{fm},1)}$ . For  $\hat{K}^{\text{fm},1}$ , these two terms are given by:

$$\begin{aligned} \lambda_1^{(\text{fm},1)} &= (N(t) - 1) \\ \lambda_2^{(\text{fm},1)} &= \sum_{i=1}^{N(t)} d_i^2 m_i^{-\frac{1}{2}} w_i \end{aligned} \quad (4.39)$$

which yields the following selection properties  $h_1^{(\text{fm},1)}$ ,  $h_2^{(\text{fm},1)}$ :

$$\begin{aligned} h_1^{(\text{fm},1)} &= 1 \\ h_2^{(\text{fm},1)} &= d_i^2 m_i^{-\frac{1}{2}} w_i \end{aligned} \quad (4.40)$$

A selection property of 1 indicates uniform selection probability; that is, each computational particle has an equal chance for being selected, regardless of its physical properties. The coagulating partners  $i$  and  $j$  are selected according to the probabilities:

$$\frac{h_1^{(\text{fm},1)}(P_i, w_i)}{\lambda_1^{(\text{fm},1)}} \text{ and } \frac{h_2^{(\text{fm},2)}(P_j, w_j)}{\lambda_2^{(\text{fm},1)}} \quad (4.41)$$

The particle selection properties and partial sums for the remainder of the free-molecular and slip-flow kernels are summarised in Table 4.1.

### Coagulation jump process

If a coagulation event is selected to occur, two particles must be chosen from the ensemble and physically joined. This process is represented by Equation 4.20. The weight transfer functions  $\gamma(P_i, w_i, P_j, w_j)$  define how the statistical

**Table 4.1:** Particle selection properties for the weighted transition kernel

Term	Equation	Particle 1	Particle 2
FM1	$(N(t) - 1) \sum d_i^2 m_i^{-\frac{1}{2}} w_i$	Uniform	$d_i^2 m_i^{-\frac{1}{2}} w_i$
FM2	$\sum d_i^2 \sum m_i^{-\frac{1}{2}} w_i - \sum d_i^2 m_i^{-\frac{1}{2}} w_i$	$d_i^2$	$m_i^{-\frac{1}{2}} w_i$
FM3	$\sum d_i^2 w_i \sum m_i^{-\frac{1}{2}} - \sum d_i^2 m_i^{-\frac{1}{2}} w_i$	$m_i^{-\frac{1}{2}}$	$d_i^2 w_i$
FM4	$\sum d_i^2 m_i^{-\frac{1}{2}} \sum w_i - \sum d_i^2 m_i^{-\frac{1}{2}} w_i$	$d_i^2 m_i^{-\frac{1}{2}}$	$w_i$
SF1	$2(N(t) - 1) \sum w_i$	Uniform	$w_i$
SF2	$\sum d_i \sum d_i^{-1} w_i - \sum w_i$	$d_i$	$d_i^{-1} w_i$
SF3	$\sum d_i w_i \sum d_i^{-1} - \sum w_i$	$d_i^{-1}$	$d_i w_i$
SF4	$(N(t) - 1) \sum d_i^{-1} w_i$	Uniform	$d_i^{-1} w_i$
SF5	$\sum d_i \sum d_i^{-2} w_i - \sum d_i^{-1} w_i$	$d_i$	$d_i^{-2} w_i$
SF6	$\sum d_i w_i \sum d_i^{-2} - \sum d_i^{-1} w_i$	$d_i^{-2}$	$d_i w_i$
SF7	$\sum d_i^{-1} \sum w_i - \sum d_i^{-1} w_i$	$d_i^{-1}$	$w_i$

**Table 4.2:** Definition of the coagulation weight transfer functions.

Name	Formula
SWA1	$w_i \frac{w_j}{w_i + w_j}$
SWA3	$w_i \frac{m_i}{m_i + m_j}$

weights are manipulated through such a process and are summarised in Table 4.2 [122].

The two best performing weight transfer functions (SWA1 and SWA3) from the family derived in [122] were selected for the numerical tests in this chapter.

In a stochastic coagulation process, two particles are first selected to coagulate. For direct simulation, the mass of the second particle is added to the first, and the ‘old’ second particle is deleted. As discussed in the introduction, the ensemble will eventually deplete if not somehow replenished. This is done by doubling the ensemble when the number of computational particles  $N(t)$  falls below half of the maximum capacity  $N_{\max}$ . When using SWAs, the weight of the first particle is adjusted (using the functions in Table 4.2), then the mass of the second particle is added to the first, and the second particle is left unchanged. As no particles are deleted, there is no need for a doubling algorithm. The ensemble properties cached in the binary tree structure are updated at the end of the coagulation event [54, 122]. The complete process in which a coagulation event is handled is provided in Figure 4.1.

### 4.3 Numerical studies

While the stochastic weighted algorithms presented in the previous section are general and may be applied to a stochastic population balance method with any particle model, the multivariate silica particle model is used here as a test-case. A simple case was defined in [143] in which numerical convergence studies were conducted. This case simulated a zero-dimensional batch reactor with 250 ppm of precursor (tetraethoxysilane, TEOS) in nitrogen bath gas. The temperature was held constant at 900 °C and a residence time of 0.8 s was chosen. The numerical parameters, model parameters and process settings used for this test case are summarised in Table 4.3.

As in [143], the convergence of several key metrics was studied as a function of the number of computational particles  $N_{\max}$  and runs  $L$ . These are given in Table 4.4, along with their physical interpretations. For a simulation with a given  $(N_{\max}, L)$ , the run-average (Equation (2.28)) and confidence interval (Equation (2.29)) of each metric was determined. These results are given in the following section.

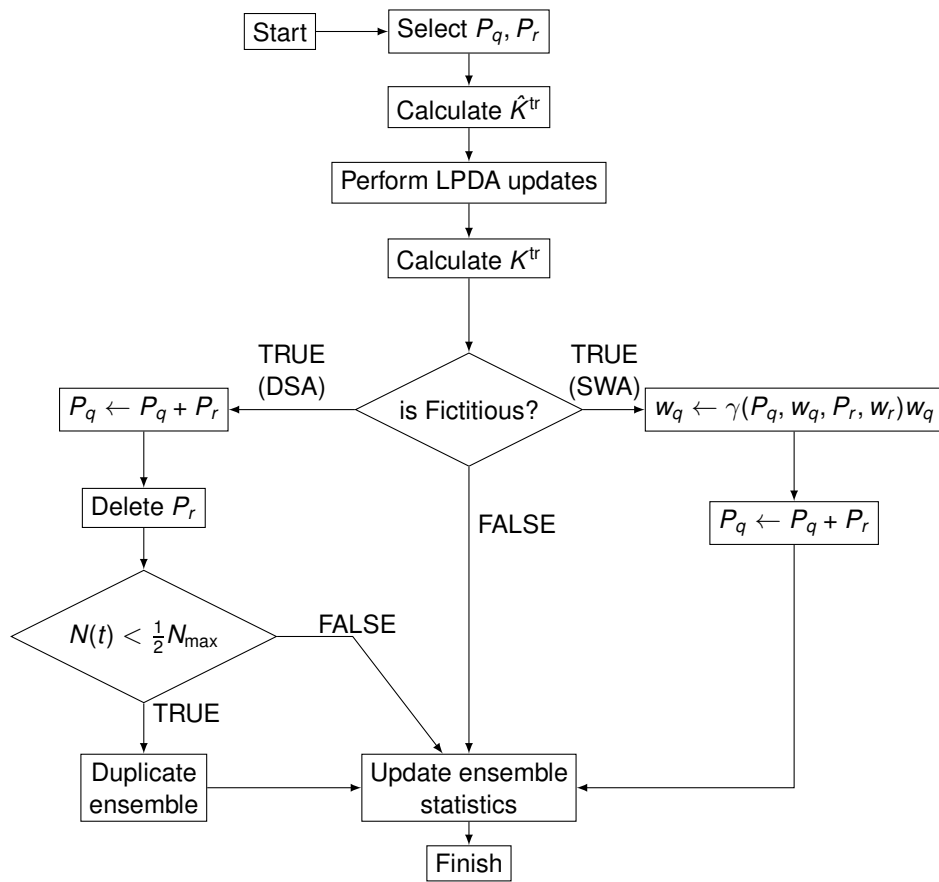


**Figure 4.1:** Comparison of the coagulation process implemented in direct simulation algorithm and weighted particle methods.

**Table 4.3:** Numerical and model parameters used for the silica test case.

Description	Symbol	Value	Ref.
<i>Numerical parameters</i>			
Number of splits	$N_{\text{splits}}$	100	[143]
Timestep	$\Delta t$	0.0015 s	[143]
Max. number of stochastic particles	$N_{\text{max}}$	64–131072	[143]
Number of runs	$L$	1–2048	[143]
<i>Model parameters</i>			
Maximum zeroth moment	$M_{0,\text{max}}$	$1.6 \times 10^{18} \text{ \#/m}^3$	[143]
Sintering pre-exponential	$A_S$	$1.1 \times 10^{16} \text{ s/m}$	[143]
Sintering characteristic energy	$E_S$	$1.2 \times 10^5 \text{ K}$	[143]
Sintering minimum diameter	$d_{p,\text{min}}$	4.4 nm	[143]
Surface smoothing factor	$\sigma_{\text{SR}}$	1.0	[142]
Gas-phase parameters	-	-	[142]
Free-molecular enhancement factor	$k_{\text{fm}}$	2.2	[66]
<i>Process settings</i>			
Initial temperature	$T$	900 °C	[143]
Residence time	$\tau$	0.8 s	[143]
Initial TEOS fraction	$y_{\text{TEOS}}$	250 ppm	[143]
Initial total pressure	$P_i$	1.0 atm	[143]

**Table 4.4:** Summary of key process metrics (from Shekar et al. [144]) investigated in this chapter.

$X(t)$	Description	Formula
$M_0(t)$	Particle number concentration	$\frac{1}{V_{\text{smp}}} \sum_{i=1}^{N(t)} w_i$
$F_V(t)$	Particle volume fraction	$\frac{1}{V_{\text{smp}}} \sum_{i=1}^{N(t)} w_i V_i$
$\mu_a(n)(t)$	Mean number of primaries per particle	$\frac{1}{\sum w_i} \sum_{i=1}^{N(t)} w_i n_i$
$\mu_a(d_{\text{col}})(t)$	Mean collision diameter	$\frac{1}{\sum w_i} \sum_{i=1}^{N(t)} w_i d_{\text{col},i}$
$\mu_a(\overline{d}_{\text{pri}})(t)$	Mean average primary diameter	$\frac{1}{\sum w_i} \sum_{i=1}^{N(t)} w_i \overline{d}_{\text{pri},i}$
$\mu_a(\overline{s})(t)$	Mean average sintering level	$\frac{1}{\sum w_i} \sum_{i=1}^{N(t)} w_i \overline{s}_i$

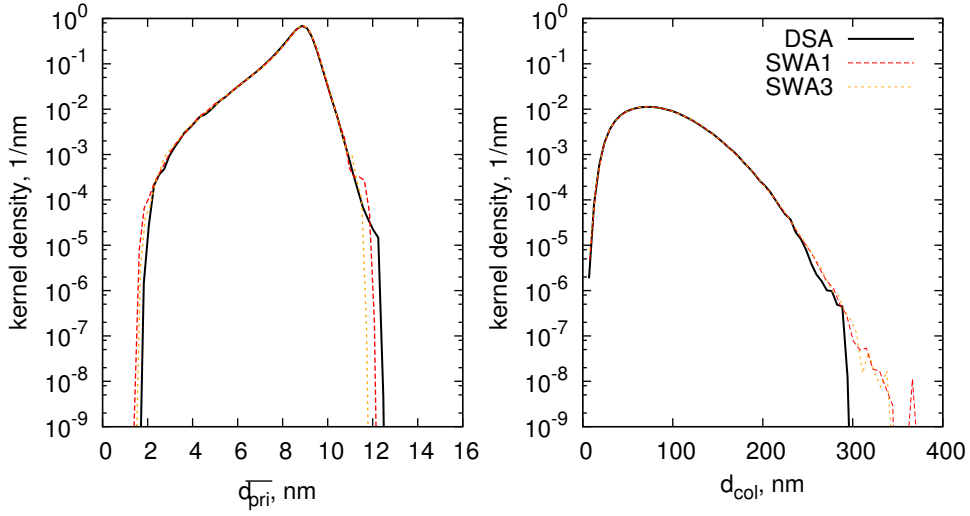


Figure 4.2: PSDs predicted by the high-precision solutions at  $t = 0.8$  s.

## 4.4 Results

### 4.4.1 High-precision solution

Before investigating any useful convergence properties of the weighted methods, one must ascertain whether the solutions when using SWAs converge in the limit to those solutions when using direct simulation. Here, the high-precision solutions ( $N_{\max} = 131072$ ,  $L = 10$ ) are compared.

The particle size distributions (PSDs) predicted by the algorithms were first examined. As the silica model tracks primary particles, a PSD of the primary particles may be generated in addition to PSDs for the aggregates. The high-precision primary and collision PSDs are given for direct simulation and the weighted methods in Figure 4.2. These were generated using a Gaussian kernel density estimation procedure, and the normal distribution approximation to estimate the bandwidth [146].

It is evident that the SWA1 and SWA3 algorithms perfectly reproduce the PSD predicted by direct simulation. Further, SWA1/3 better resolve the large ( $>300$  nm) and rare particles.

The metrics in Table 4.4 also provide a useful tool to examine agreement between algorithms. The temporal evolution of such metrics for the direct simulation and weighted algorithms is presented in Figure 4.3.

Again, the SWA1 and SWA3 algorithms produce trajectories with excel-

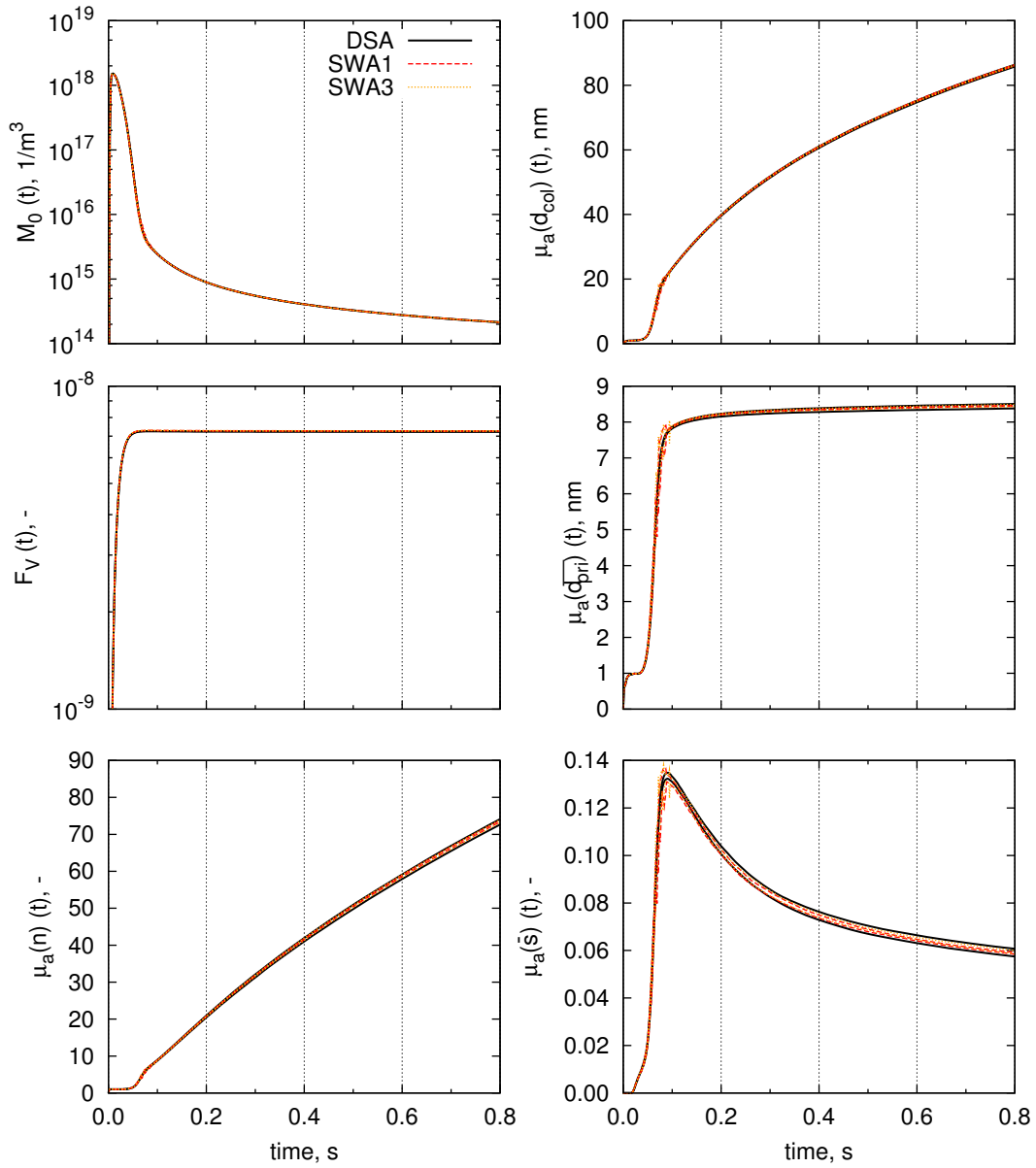


**Figure 4.3:** Temporal evolution of Table 4.1's key metrics for the high-precision solutions using DSA and SWAs. The two lines show the upper- and lower-bound of the 99.9% confidence interval.

lent agreement with those of DSA. The confidence intervals for these cases are typically too narrow to be observed here. It is clear that the SWAs' high-precision solutions are equivalent to those predicted through direct simulation, indicating that all algorithms approach the same solution in the limit as  $N_{\max} \rightarrow \infty$ .

#### 4.4.2 Convergence of algorithms

When using stochastic particle methods, one must choose  $L$  such that the statistical uncertainty in the results is acceptably small. One must also choose  $N_{\max}$  such that the systematic error appears close to zero, however in practice it may be chosen such that the differences between successive values of  $N_{\max}$  are not statistically significant. The multidimensional silica particle model permits tracking of any number of functionals describing the particle size and morphology. Here, the convergence behaviour of these metrics is investigated.

The convergence studies reported here were conducted by varying  $N_{\max}$  and  $L$  while holding their product  $N_{\max} \times L$  constant at a value of  $2^{17}$ . The relationship between the final average value of these functionals and  $N_{\max}$  is given in Figure 4.4. The uncertainty in each point is depicted using the confidence interval  $I_{0.999}(t_f)$ .

##### Particle number concentration

The final value of the SWA solutions for particle number concentration  $M_0$  (or zeroth moment) has lower systematic error than direct simulation.

##### Volume fraction

The volume fraction represents the ratio of total particle volume to gas volume. The SWAs achieve a solution within the confidence interval of the high-precision solution for  $N_{\max} \geq 128$ , indicating that they accurately predict the volume fraction with very few stochastic particles.

##### Mean number of primaries per particle

The mean number of primaries per particles  $\mu_a(n)$  is a measure of both the size of the aggregate and number of coagulation events. Figure 4.4 shows that much smaller aggregates are obtained when  $N_{\max}$  is too low.

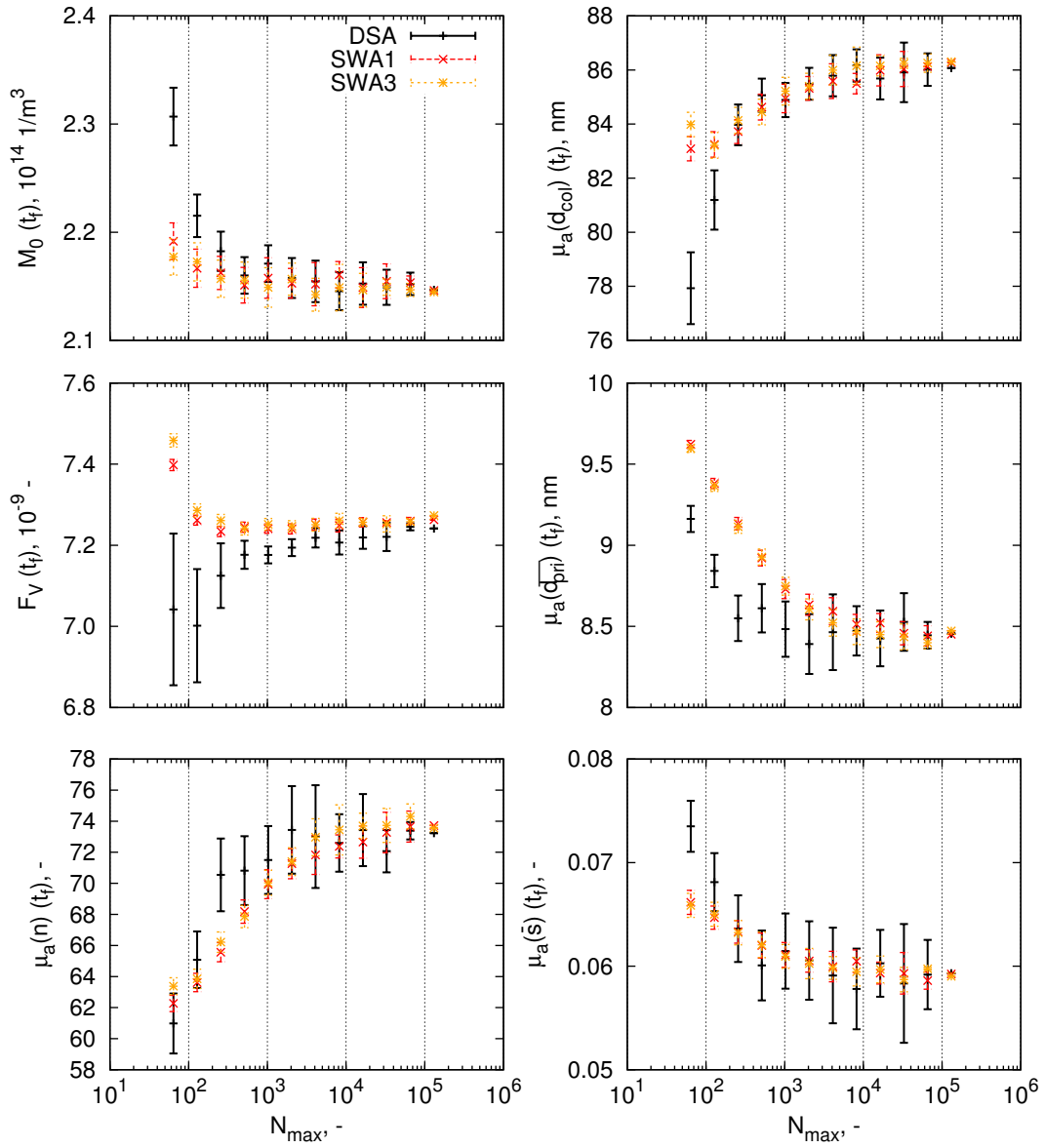


**Figure 4.4:** Run-averaged values of the functionals studied (Table 4.4) and their corresponding confidence intervals at  $t = 0.8\text{s}$  with  $N_{\max} \times L = 2^{17}$ .

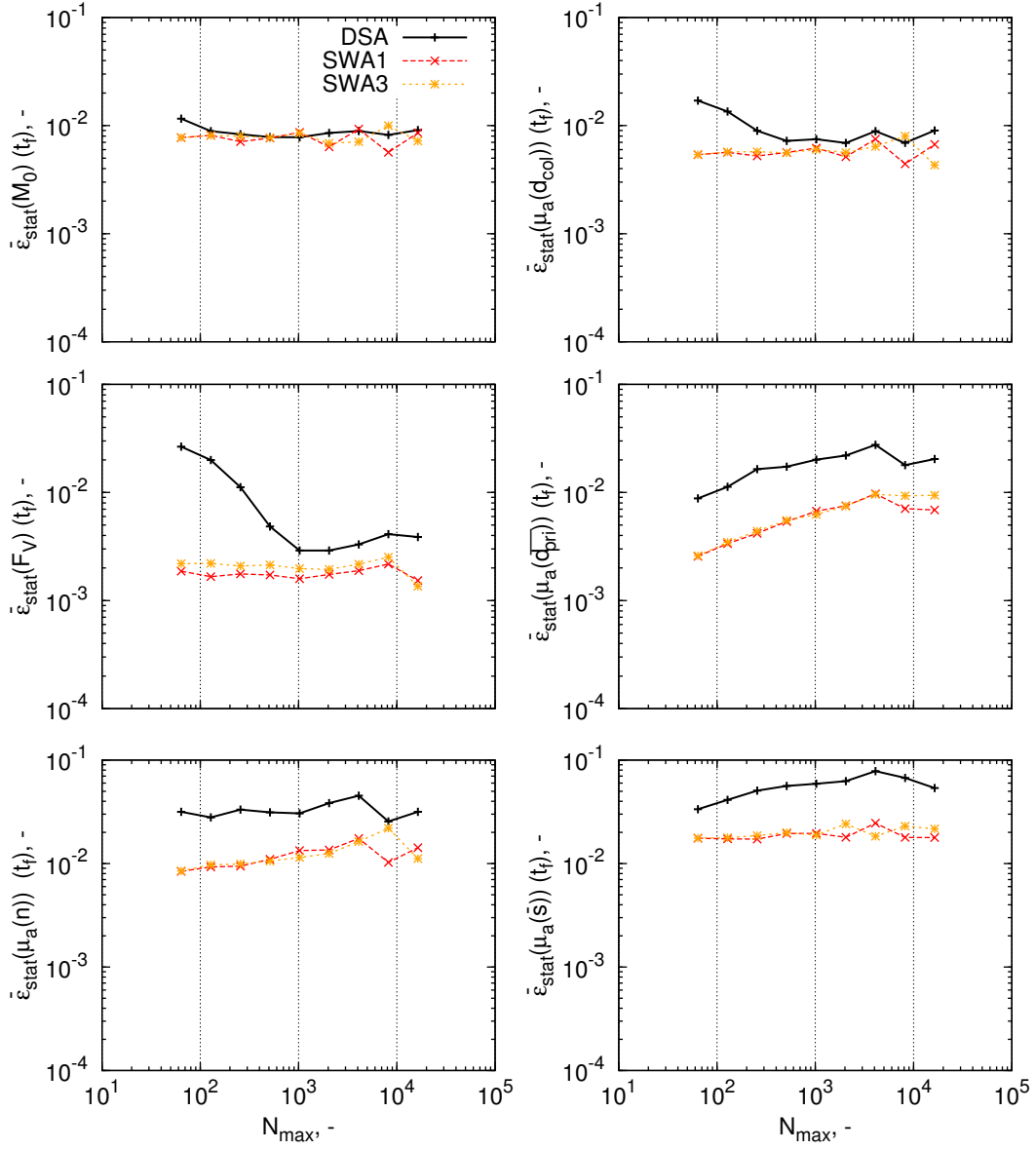


**Figure 4.5:** Relative statistical error of final values for Table 4.3's metrics with constant  $N_{\max} \times L = 2^{17}$ .

### Mean collision diameter

The mean collision diameter  $\mu_a(d_{\text{col}})$  is an important property which characterises the size of an aggregate particle. SWAs appear to have better accuracy at lower  $N_{\text{max}}$ , but there is a common limit as  $N_{\text{max}}$  becomes large.

### Mean primary diameter

The mean average primary diameter  $\mu_a(\overline{d_{\text{pri}}})$  estimates the average size of the primary particles which compose an aggregate. Curiously, despite SWAs predicting the final value of the collision diameter better than DSA, they have a larger systematic error than DSA for fewer computational particles. This may be associated with SWAs preference towards larger particles (with larger primaries).

### Mean sintering level

The mean average sintering level  $\mu_a(\overline{s})$  is a measure of the extent to which the ensemble's particles are sintered. SWAs and DSA show similar convergence properties for this metric.

In summary, the weighted methods show convergence for fewer stochastic particles for  $M_0$ ,  $F_V$ ,  $\mu_a(d_{\text{col}})$ , and the sintering level. Figure 4.4 demonstrates that the SWAs consistently have a smaller confidence interval than an equivalent DSA simulation with a given  $N_{\text{max}}, L$ . This is consistent with observations made in [122].

In any case, it is evident that Table 4.4's functionals satisfactorily converge to a stable value. For this system, a choice of  $N_{\text{max}} \geq 16384$  would be recommended when using SWAs.

### 4.4.3 Computational efficiency

The computational time required to simulate the silica test system for a given  $N_{\text{max}}$ ,  $L$ , or error is investigated in this section. These calculations were conducted on a SGI Altix Cluster with nodes composed of two 3.00 GHz quad core Intel Harpertown processors and 8 GB of RAM.

The computational times of the DSA and SWA simulations for increasing  $N_{\text{max}}$  are compared in Figure 4.6. Typically, a simulation with a given  $N_{\text{max}}$  and  $L = 1$  using SWAs required six to eight more times the CPU time than

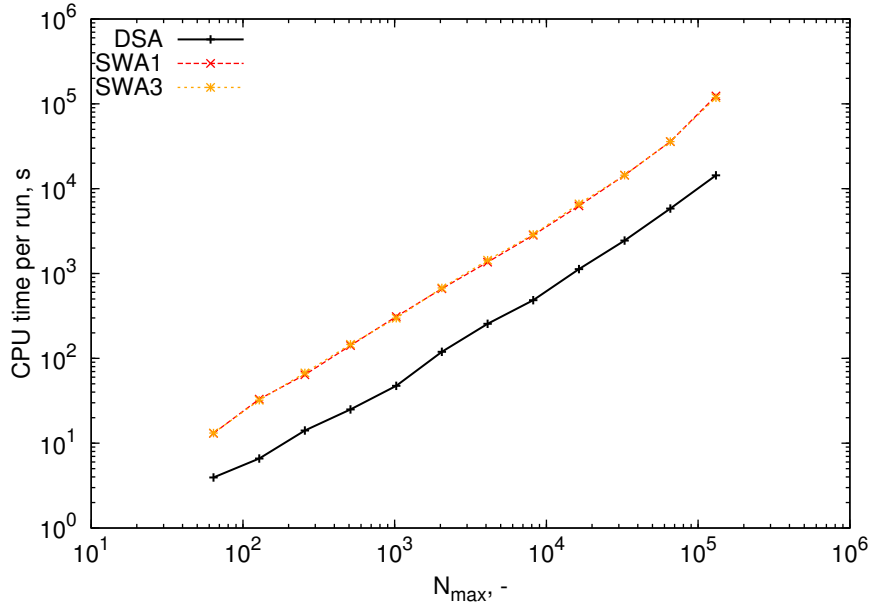


**Figure 4.6:** Average CPU time required per run as a function of number of stochastic particles.

the equivalent DSA simulation. Further, it was observed that the time required per run increases approximately linearly with the maximum number of stochastic particles.

It is also no coincidence that the additional time required by the SWAs as compared to the DSA is proportional to the number of additional simulated coagulation events, which are shown in Figure 4.7. Firstly, as SWAs emphasise calculation of larger, rarer particles (e.g. [122] or Figure 4.2), more time on average is required to determine the extent of sintering (Equations (4.10) and (4.13)) of the ensemble's particles at the end of each timestep. Secondly, as SWAs always have a full ensemble ( $N(t) = N_{\max}$ ), there are always more particles for which the process jump rates and sintering characteristics must be evaluated.

The additional numerical coagulation events that occur during SWA computations are a consequence of the redistributed statistical accuracy, that also reduces the variance of the studied metrics. This is depicted in Figure 4.5, where the confidence interval widths (or relative statistical error  $\epsilon_{\text{stat}}$ ) for the metrics' final values are compared across algorithms. Generally, a constant confidence interval is obtained, with a few notable excep-

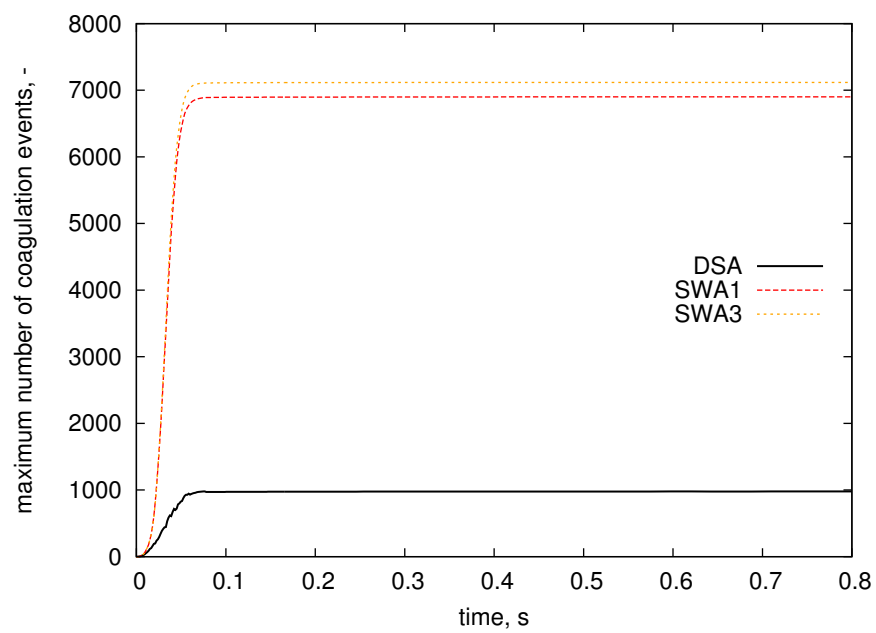


**Figure 4.7:** Comparison of the maximum number of coagulation events undergone by particles for direct simulation and the SWAs for  $N_{\max} = 131072$ .

tions. Those metrics which show steadily increasing or decreasing statistical errors correspond to the metrics whose final values (at  $N_{\max}$  small) is significantly different ( $\sim 10\%$ ) from the high-precision solution. That is, the presence of systematic error in the confidence interval when a simulation is unconverged affects the estimation of statistical error.

The difference in size of DSA confidence intervals with respect to the SWA intervals is dependent on the metric analysed. For the zeroth moment they are the same, however for primary diameter they differ by a factor of about 4. It is evident that the weighted methods offer superior variance reduction for all of the unique properties tracked in the multidimensional particle model.

## 4.5 Conclusions

This chapter has used majorant techniques to adapt the transition regime coagulation kernel to weighted particle methods. This is an important development if SWAs are to be used to solve real-world coagulation problems. This kernel is used in conjunction with a state-of-the-art multidimensional silica particle model to investigate the numerical behaviour of the population balance solution methodology.

Within the particle model, particles are described by the primary particles and their connectivity, which are in turn described by the number of Si, O and OH units of which they are composed. This permits tracking of many detailed features of the particles and particle ensemble through time.

Two SWAs were tested for convergence to direct simulation in the limit. Excellent agreement of all algorithms' high-precision solutions was obtained, indicating that the weighted algorithms are expected to converge to the direct simulation solution for sufficiently large number of stochastic particles.

The convergence of the functionals describing particle properties was investigated with respect to the maximum number of computational particles in the ensemble. SWAs generally achieved the correct value of these functionals for fewer stochastic particles than DSA, except in the calculation of number of primary particles and the primary diameter. For a calculation with a given number of stochastic particles and runs, the confidence intervals of the functionals were up to four times smaller, indicating that weighted algorithms studied here achieve better variance reduction than di-

rect simulation. However, this comes at the cost of increased computational expense, with the algorithms requiring approximately seven times more CPU time per run than direct simulation.

In this chapter, it was demonstrated that stochastic weighted algorithms can be successfully used to solve population balances with real-world coagulation kernels and complex particle models. This is particularly important for spatially inhomogeneous systems, where weighted methods offer practical and numerical advantages over direct simulation. A new majorant formulation of the transition kernel, as adapted to stochastic weighted algorithms was presented. A detailed numerical analysis of the convergence properties and efficiency of these methods was conducted, showing that weighted methods satisfactorily converge to a stable numerical solution.

## Chapter 5

# Solution of reactor networks

*An algorithm to solve networks of reactors with population balance models is presented. The convergence of the stochastic particle method is evaluated as a function of network size, feedback and numerical parameters.*

*Material from this chapter is published in [94].*

Population balance modelling has traditionally been applied to modelling particle formation in a batch or a plug-flow reactor [8, 92, 99]. In the former case, the equations governing particle growth can be simplified to exclude terms for particle transport to and from the reactor. For the latter case, the reactor model typically represents an axial streamline through the plug flow reactor (PFR). However, there are many systems found in engineering where advective or diffusive particle transport is important [82, 119]. This typically requires use of computational fluid dynamics (CFD) or a reactor network approach, coupled with a population balance model to accurately capture particle dynamics.

Solutions for the population balance equation in these coupled systems may be grouped into several classes, the most common of which are monodisperse [18, 68], moment [3, 4, 48, 89] and sectional [130] methods. All of these methods yield a set of differential equations which may be solved within the framework of the differential equations describing fluid transport and/or chemical reactions [82].

Many commercial packages now include particle population balance models using the aforementioned methods, for example FLUENT [6], CHEMKIN-PRO [131] and gPROMS [10]. The major drawback of using these methods

to solve the population balance equations is that they either do not resolve the particle size distribution (e.g. moments) or they utilise a simplified particle model such as a spherical or surface-volume type description. This can cause errors when particle aggregates are formed through coagulation and sintering [91].

Implementation of stochastic population balance solvers for flow systems requires discretising the reactor geometry into a mesh composed of reactor cells [82, 119]. These connected cells can be considered a type of reactor network. Kruis et al. [82] developed a ‘cell-based weighted random walk’ method to account for the movement of particles between cells in one- and two-dimensional reactor geometries. While reasonably good agreement with a moments code was reported, it was observed that the method was sensitive to stochastic noise, a result of using too few computational particles.

Patterson and Wagner [119] presented a stochastic method for coagulation-advection problems. The performance in accounting for coagulation of the conventional DSA against SWAs was evaluated. It was reported that DSA is particularly susceptible to stochastic noise, which eventually manifests itself as a systematic variance from the true solution.

A study by Zhao and Zheng [169] gave a three-dimensional adaptation of a stochastic population balance solver (using an SWA [170]) coupled with a CFD code. An algorithm was presented to de-couple the fluid flow, particle flow and particle dynamics by choosing an appropriate timestep size. In a similar vein to [82], limits associated with computational cost restricted the maximum number of computational particles, preventing precise agreement with direct numerical simulation (DNS).

‘Multizonal’ [11, 12] or ‘compartmental’ models [5, 67, 84, 167] are models in which the fine mesh of CFD is simplified to a coarse network of reactors with a specified flow between each node. Such techniques typically require orders of magnitude fewer reactor cells, thus reducing computational cost, however this comes at the price of decreased spatial resolution of particle dynamics.

Only recently have these models begun to be investigated using stochastic methods. Irizarry [67] recently presented an approach to solve a population balance compartmental model using a stochastic method. A new algorithm to move particles between cells (‘particle bundle flow’ method) was

reported, in which particles were restricted from jumping more than one compartment by choosing a suitably small timestep. The numerical properties of some test systems were evaluated as a function of the timestep, however the effect of other numerical parameters was not addressed.

There are additional open questions in solving reactor networks with stochastic population balance solvers. In order to maximise efficiency of these algorithms, it is necessary to understand the convergence of these algorithms with respect to the number of computational particles and independent runs [143]. Further, it is important to quantify and reduce stochastic noise in the system, as this was identified as a potential issue in [82]. Finally, the coupling of a such a system to a reacting gas-phase has not yet been investigated.

The purpose of this chapter is to extend the work of Irizarry [67], Kruis et al. [82] and Zhao and Zheng [169] by developing an algorithm for solving a fully-coupled gas-phase ODE/particle population balance network. The convergence properties of the stochastic population balance will first be investigated, and methods to reduce statistical error will be considered. The flexibility of stochastic methods in solving the population balance equation will be demonstrated by use of a detailed multivariate particle model to simulate silicon nanoparticle growth in a plug-flow reactor.

The structure of this chapter is as follows. In Section 5.1, the reactor models are presented. The stochastic solution methodology and model used for generating reference solutions are discussed in Sections 5.1.1 and 5.1.2, respectively. The numerical test cases and their results are discussed in Section 5.2. Finally, Section 5.3 illustrates one of the many ways in which reactor networks can be applied to model a real reactor system.

## 5.1 Model

This work will study the numerical and physical behaviour of a constant-pressure network of perfectly-stirred reactors (PSRs; or continuous-stirred tank reactors, CSTRs). It is assumed that each of these reactors has a characteristic residence time  $\tau_{\text{PSR}} = Q/V$  associated with it, where  $Q$  is the volumetric flowrate and  $V$  is the reactor volume. The inflow and outflow terms modify Equation (2.13) to:

$$\begin{aligned} \frac{d}{dt}n(P_q) &= \mathcal{I}(\mathbf{c}, P_q) + \mathcal{K}(\mathbf{n}, P_q) + \mathcal{R}(\mathbf{c}, \mathbf{n}, P_q) + \mathcal{S}(\mathbf{n}, P_q) \\ &+ \frac{1}{\tau_{\text{PSR}}} \left( \sum_{j=1}^{N_{\text{in}}} f^{[j]} n^{[j]}(P_q) - n(P_q) \right) - \gamma(\mathbf{c}, \mathbf{n}, T) n(P_q) \end{aligned} \quad (5.1)$$

where the reactor is assumed to have  $N_{\text{in}}$  inflow streams, each with fraction  $f^{[j]}$  of the total volumetric flow. The operators  $\mathcal{I}(\mathbf{c}, P_q)$ ,  $\mathcal{K}(\mathbf{n}, P_q)$ ,  $\mathcal{R}(\mathbf{c}, \mathbf{n}, P_q)$  and  $\mathcal{S}(\mathbf{n}, P_q)$  take the same form as in Equations (2.15), (2.17), (2.19) and (2.21) respectively. For  $N_{\text{GP}}$  gas-phase species, the rate of change in concentration of species  $k$  is given by:

$$\frac{dc_k}{dt} = \dot{\omega}_k(\mathbf{c}, T) + \dot{g}_k(\mathbf{c}, \mathbf{n}, T) + \frac{1}{\tau_{\text{PSR}}} \left( \sum_{j=1}^{N_{\text{in}}} f^{[j]} c_k^{[j]} - c_k \right) - \gamma(\mathbf{c}, \mathbf{n}, T) c_k \quad (5.2)$$

where  $\dot{\omega}_k(c, T)$  and  $\dot{g}_k(c, \mathbf{n}, T)$  are the molar production rates of species  $k$  at temperature  $T$  due to gas-phase and particle reactions, respectively. The gas-phase expansion factor for a PSR is given by:

$$\gamma(\mathbf{c}, \mathbf{n}, T) = \frac{1}{\rho} \left( \sum_{k=1}^{N_{\text{GP}}} [\dot{\omega}_k + \dot{g}_k] + \frac{1}{\tau_{\text{PSR}}} \left[ \sum_{j=1}^{N_{\text{in}}} f^{[j]} \rho^{[j]} - \rho \right] \right) + \frac{1}{T} \frac{dT}{dt} \quad (5.3)$$

where  $\rho$  is the molar density of the mixture. Ignoring energy changes due to the particle population balance, the adiabatic energy balance of a constant-pressure PSR is:

$$\rho \bar{C}_p \frac{dT}{dt} = \sum_{k=1}^{N_{\text{GP}}} \left( -\hat{H}_k \dot{\omega}_k + \frac{1}{\tau_{\text{PSR}}} \sum_{j=1}^{N_{\text{in}}} f^{[j]} c_k^{[j]} [\hat{H}_k^{[j]} - \hat{H}_k] \right) \quad (5.4)$$

where  $\bar{C}_p$  is the bulk heat capacity and  $\hat{H}_k$  is the specific molar enthalpy of species  $k$ .

### 5.1.1 Stochastic method

#### Type-space

The spherical type-space presented in Chapter 3 will be used for the numerical and case studies of this chapter. Here, the type-space will be written as:

$$P_q = P_q(p(\eta_1)) \quad (5.5)$$

where computational particle  $q$  contains one primary  $p$  with an arbitrary component  $\eta_1$ . For this very simple particle model, the type-space can be simplified to:

$$P_q = P_q(p(\eta_1)) = P_q(v^{(q)}) \quad (5.6)$$

### Particle processes

In the stochastic method, the process which create and change particles are typically implemented as jump processes [91]. A very simple particle mechanism will be used in this chapter to test the reactor network implementation. It is briefly discussed here.

### Inception

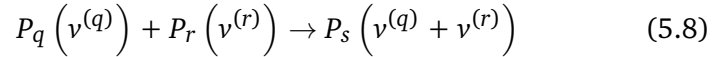
Particles are created in the population balance by inception:



where  $\chi_1$  is a nucleating gas-phase species, and  $v_1$  is the size of the smallest possible particle.

### Coagulation

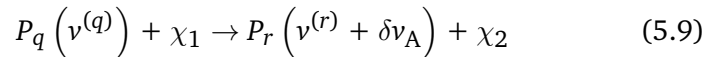
Particles coagulate and stick together according to the following reaction:



Both the constant kernel ( $K^{\text{const}} = 1$ ) and transition kernel ( $K^{\text{tr}}$ ) are used in this chapter.

### Surface growth

A surface reaction event may occur in the following manner:



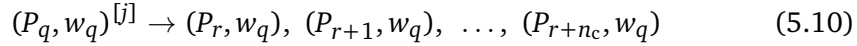
where  $v^{(q)} = v^{(r)}$ ,  $\chi_1$  is a reacting gas-phase species,  $\chi_2$  is a product species, and  $\delta v_A$  is the volume element added due to the reaction.

### Algorithms for coagulation

The key challenge in stochastic particle methods is how to solve the Smoluchowski coagulation equation [93]. In this chapter, DSA and a stochastic weighted algorithm (SWA1 of Table 4.2) will again be compared.

## Flow processes

Previous studies account for particle transport by moving computational particles between cells [67, 169]. Alternative formations for accomplishing this task are presented in the following section. An inflow process uniformly selects a particle of index  $q$  from inflow stream  $j$ , identifying the particle to be copied into the ensemble. This is represented by the reaction:



where  $P_r$  is a copy of  $P_q$ , and  $n_c$  copies of the particle are made. Note that the particle weights remain unchanged in the inflow process. The number of copies to add is determined by the scaling factor:

$$n_c = \begin{cases} \lfloor F_c \rfloor + 1 & \text{for } u < F_c - \lfloor F_c \rfloor \\ \lfloor F_c \rfloor & \text{otherwise} \end{cases} \quad (5.11)$$

where  $u$  is a pseudorandomly chosen real number such that  $u \in [0, 1)$ . Adding multiple copies of particles in this manner has the advantage of accelerating the computational particle count  $N(t)$  to the maximum value  $N_{\max}$ , thus preventing depletion of the ensemble (when using the DSA) should the outflow rate be similar. The quantity  $F_c$  represents the ratio of the current to inflow ensemble scaling factors:

$$F_c = \frac{V_{\text{smp}}}{V_{\text{smp}}^{[j]}} \quad (5.12)$$

The rate of an inflow or outflow process is proportional to the number of stochastic particles in the ensemble [13, 25]. For a constant-pressure reactor with constant volumetric inflow, the rate of inflow from stream  $j$  is given as:

$$R_{\text{inflow}}^{[j]} = f^{[j]} \frac{N^{[j]}(t)}{\tau_{\text{PSR}}} \quad (5.13)$$

where  $N^{[j]}(t)$  is the number of stochastic particles in the inflow stream. Two possible implementations of an outflow are now presented. Firstly, upon selection of an outflow jump process, particles can simply be deleted:



The alternative requires consideration of flow processes as continuous rather than as a stochastic jump process. Supposing particles are lost due to an outflow process in time  $\Delta t$ , the ensemble scaling factor  $V_{\text{smp}}$  can be scaled by

factor  $F_s$  to represent a decrease in the real particle number concentration, as  $M_0 = N(t)/V_{\text{smp}}$  [93]. The rescaling factor  $F_s$  is given by:

$$F_s = \frac{1}{1 - \Delta t/\tau_{\text{PSR}}} \quad (5.15)$$

The new sample volume is obtained using  $V_{\text{smp}}^{\text{new}} = F_s V_{\text{smp}}$ . This form of particle outflow is termed a ‘rescale’ outflow. It should also be observed that the outflow process of an upstream reactor does not necessarily provide the inflow term of a downstream reactor. The rate of particle outflow from a reactor is given by:

$$R_{\text{outflow}} = \frac{N(t)}{\tau_{\text{PSR}}}. \quad (5.16)$$

The inflow and outflow (in the case of particle deletion) may be included in the stochastic particle method as conventional jump processes (e.g. in Algorithm 2 of [143]). It should also be noted that copying and deletion of computational particles makes tracking of a particle’s trajectory through the network challenging.

### Coupling to the gas-phase

The stochastic particle method is fully-coupled to a gas-phase ODE solver. The technique of operator splitting is employed to couple the gas- and particle-phases. The algorithm by which this is done (Strang splitting) has been described in detail by Celnik et al. [25] and Shekar et al. [143].

#### 5.1.2 Discrete Model

In order to assess the numerical properties of the stochastic method, a reliable reference model is needed. In this work, the Discrete Model will be used, which writes the population balance equation as a series of ordinary differential equations (ODEs) [48]. These may be solved using conventional differential equation packages. The Discrete Model is similar to a sectional method, however every particle size is represented by its own differential equation. Arbitrarily high precision can be obtained by choosing a sufficiently large maximum particle size, corresponding to the number of ODEs,  $N_{\text{ODE}}$ .

For the test particle mechanism, constant inception ( $K^{\text{const}} = 1$ ) and constant surface growth rates ( $R_{\text{SG}} = 1$ ) will be assumed. The rate of coagulation is determined using the Smoluchowski coagulation equation, and is

given in [48] as:

$$\mathcal{K}(\mathbf{n}, P_i(v^{(i)})) = \frac{1}{2} \sum_{j=1}^{i-1} K_{j,i-j} n_j n_{i-j} - n_i \sum_{j=1}^{N_{\text{ODE}}} K_{i,j} n_j \quad (5.17)$$

where  $K_{i,j}$  is the coagulation kernel evaluated for particle pair  $(P_i, P_j)$ . Supposing that particles of size  $i \in [1, N_{\text{ODE}}]$  are spherical with volume  $iv_1$ , and that coagulation occurs with the constant kernel, the population balance equation is written as:

$$\frac{dn_i}{dt} = \begin{cases} K^{\text{const}} - K^{\text{const}} n_i \sum_{j=1}^{N_{\text{ODE}}} n_j - R_{\text{SG}} n_i \\ \quad + \frac{1}{\tau_{\text{PSR}}} \left( \sum_{j=1}^{N_{\text{in}}} f^{[j]} n_i^{[j]} - n_i \right) & i = 1 \\ \frac{1}{2} K^{\text{const}} \sum_{j=1}^{i-1} n_j n_{i-j} - K^{\text{const}} n_i \sum_{j=1}^{N_{\text{ODE}}} n_j + R_{\text{SG}} (n_{i-1} - n_i) \\ \quad + \frac{1}{\tau_{\text{PSR}}} \left( \sum_{j=1}^{N_{\text{in}}} f^{[j]} n_i^{[j]} - n_i \right) & i > 1 \end{cases}$$

### 5.1.3 Solution of reactor networks

The formulation of the above flow processes permits linking of reactors in a generic manner. To solve the transient response of the network, a simple sequential procedure is adopted. This is termed ‘sequential-modular simulation’, and similar approaches have been used in other applications [169]. The algorithm employed to solve the fully-coupled gas-phase ODE system with the stochastic population balance solver for  $N_{\text{reac}}$  reactors is given in Figure 5.1.

The algorithm in Figure 5.1 illustrates the solution methodology for Strang splitting, although in theory any form of coupling, such as predictor-corrector [26], could be used. The accuracy of this algorithm is clearly dependent on choice of a sufficiently small splitting timestep  $\Delta t_s$ , which has been investigated elsewhere [67, 169].

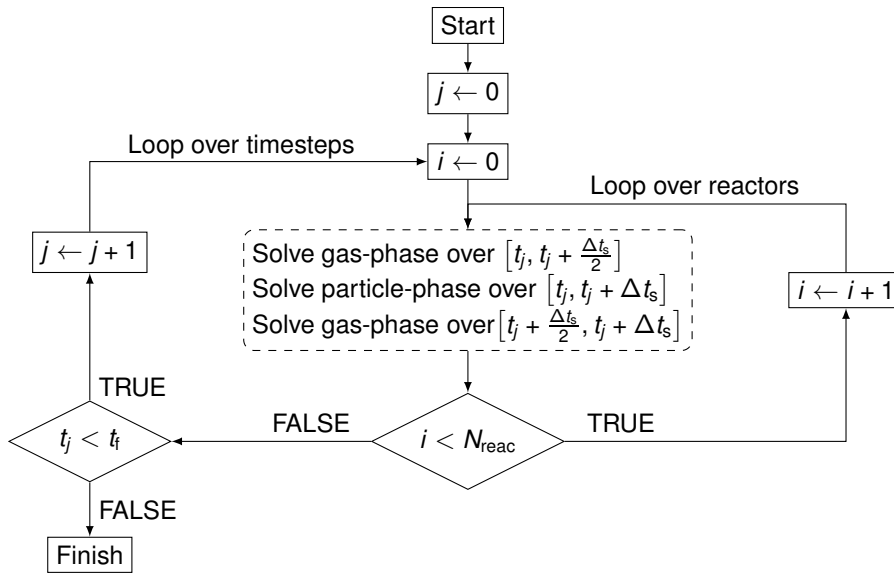


**Figure 5.1:** Algorithm used to solve the reactor network with Strang splitting.

## 5.2 Numerical studies

As in Chapter 4, the statistical quantities from Section 2.4 will be used to calculate the run-averaged mean and confidence intervals of a metric  $X(t)$ . Equations (2.31), (2.32) and (2.33) were additionally used to estimate the total average normalised error ( $\bar{\epsilon}$ ), normalised statistical error ( $\epsilon_{\text{stat}}(t)$ ) and average normalised statistical error ( $\bar{\epsilon}_{\text{stat}}$ ); respectively. The functionals studied in this chapter are given in Table 5.1.

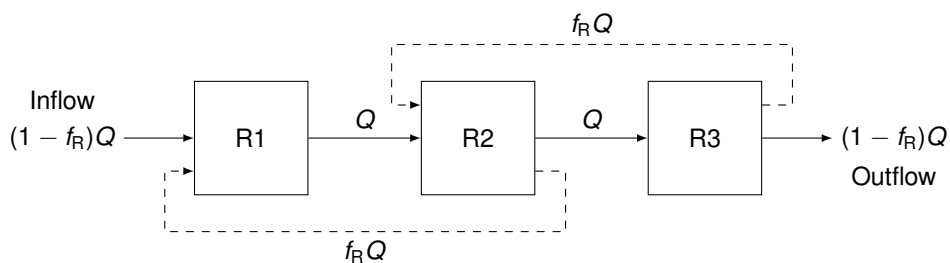
### 5.2.1 Comparison to Discrete Model

To test the validity of the stochastic particle algorithm in solving the population balance equations, a simple test system was devised: three reactors connected in series, with possible countercurrent recycle streams opposing the direction of flow. Material is recycled from reactors R2 and R3 with fraction  $f_R$ , and the total volumetric flowrate  $Q$  is constant between all reactors. It was assumed that the inflow to the network contained  $1 \text{ \#/m}^3$  particles of size  $i = 1$ , with each reactor having the same residence time  $\tau_{\text{PSR}}$ . A schematic of this system is provided in Figure 5.2(a).

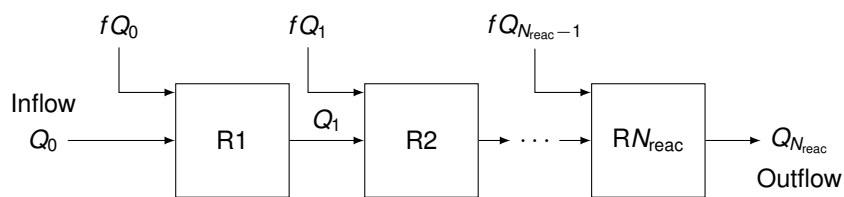
This system was solved using a simple particle mechanism including

**Table 5.1:** Summary of process metrics studied in the present work.

$X(t)$	Description	Formula
$M_0(t)$	Particle number concentration	$\frac{1}{V_{\text{smp}}} \sum_{i=1}^{N(t)} w_i$
$\mu_a(v)(t)$	Average particle volume	$\frac{1}{\sum w_i} \sum_{i=1}^{N(t)} v^{(i)}$
$M_2(t)$	Second mass moment	$\frac{1}{V_{\text{smp}}} \sum_{i=1}^{N(t)} w_i (\rho v^{(i)})^2$
$M_3(t)$	Third mass moment	$\frac{1}{V_{\text{smp}}} \sum_{i=1}^{N(t)} w_i (\rho v^{(i)})^3$



(a) Linear network with recycles



(b) Linear network with multiple inflows

**Figure 5.2:** Schematic of the test systems used in the present study.

terms for coagulation, surface growth and inception, all with rates given by a constant. While these do not represent physical rate equations, they are helpful for evaluating the performance of the stochastic particle method against other solution methodologies. This was first undertaken by applying the Discrete Model [48] and the stochastic particle method (using the SWA [122]) to solve the test system. The results of this analysis are given in Figure 5.3, for a linear ( $f_R = 0$ ) and countercurrent (with  $f_R = 0.5$ ) network; and  $N_{\max} = 16384$ ,  $L = 8$ .

The transient evolution of  $M_0$  illustrates the issue of statistical error present in stochastic solutions to the population balance equation: the random nature of the processes in the stochastic method induce fluctuations in functionals describing the system (e.g. the moments). The noise can be eliminated by averaging the solution over multiple independent runs (i.e. with a different random seed). The influence of this statistical error and systematic variation will be addressed in the following sections.

### 5.2.2 Linear networks

It is useful to investigate how the error in a stochastic solution varies with the number of computational particles ( $N_{\max}$ ) and independent runs ( $L$ ). Further, it is likely that the different coagulation algorithms and two outflow process types could contribute different amounts of systematic or statistical error to the stochastic solution. Using the test case described in the previous section, the stochastic solutions using the DSA and the SWA were generated. It was assumed that reactors R1 and R3 used outflow rescaling as their outflow process, while the outflow process type of R2 was varied. The normalised average error in R2 of the stochastic solution with respect to the Discrete Model was evaluated, with a constant  $N_{\max} \times L = 10 \times 2^{18}$ , and is given in Figure 5.4.

It is difficult to observe any meaningful differences between coagulation algorithms or outflow processes in examining the error in the zeroth moment (Figure 5.4, left panel). The approximately flat error indicates that  $M_0$  has converged for all systems by  $N_{\max} = 256$ , after which the total error is representative of the statistical error. Higher moments (e.g.  $M_2$ ,  $M_3$ ) show analogous behaviour. In contrast to this, the error in average particle volume (Figure 5.4, right panel), and similarly other average particle properties, shows a clear difference between the convergence of the DSA and

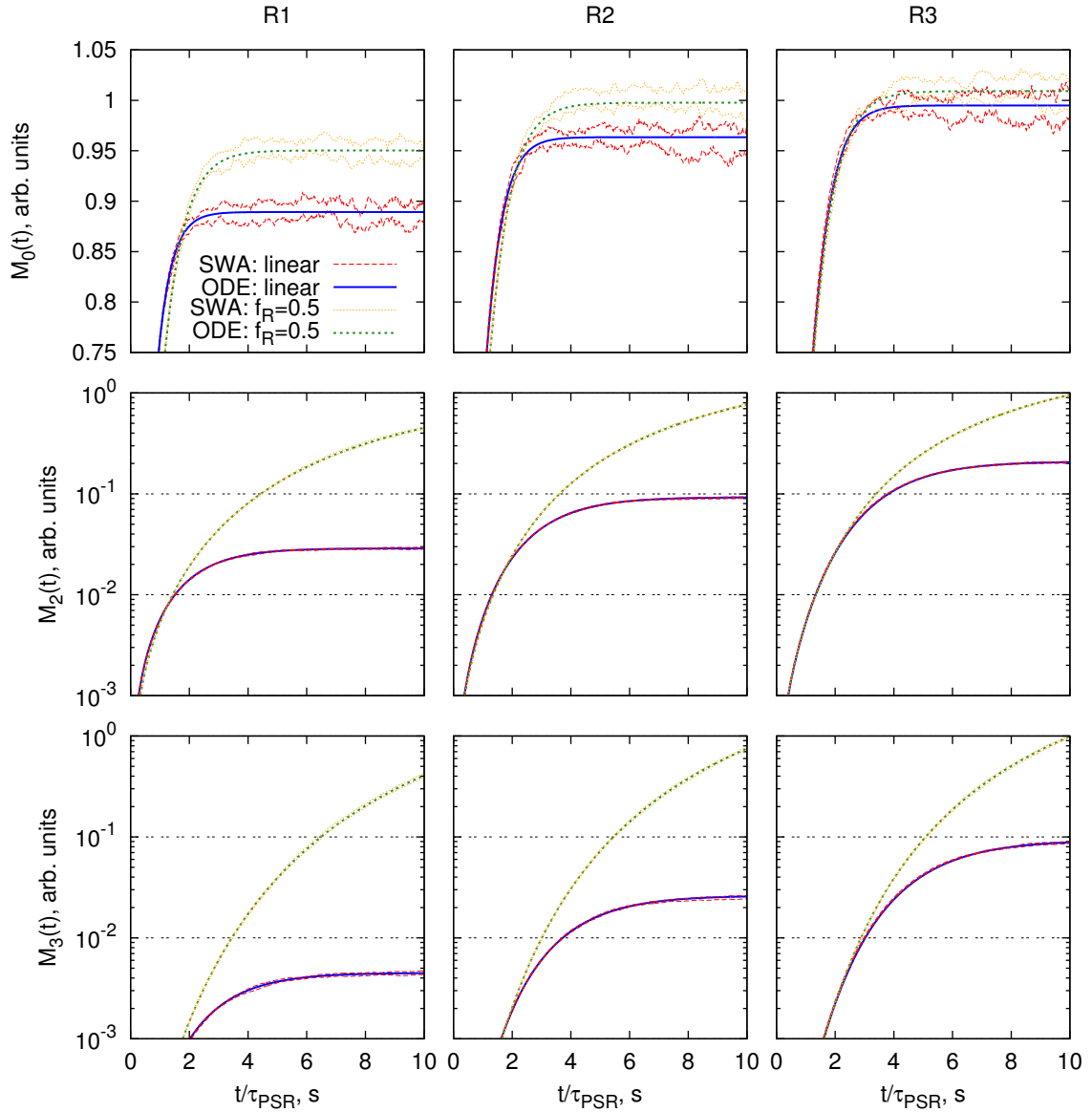


**Figure 5.3:** Comparison of solutions for transient evolution of normalised moments  $M_0$ ,  $M_2$  and  $M_3$  from the Discrete (ODE) Model [48] and stochastic method (using the SWA) for the three-reactor system (Figure 5.2(a)) with  $f_R = 0$  and  $f_R = 0.5$ . Confidence intervals of the stochastic solution are given where visible.

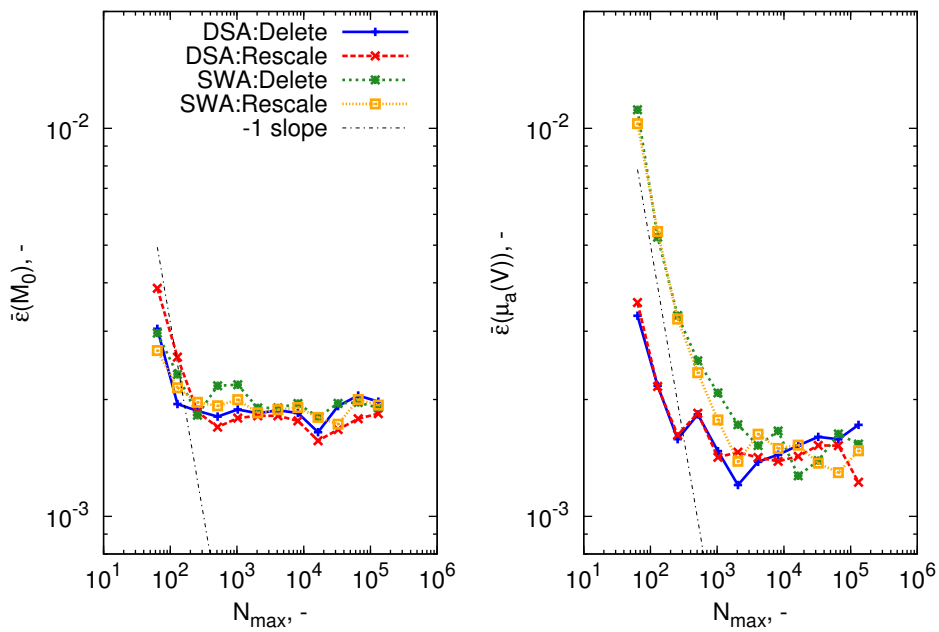


**Figure 5.4:** Convergence of the zeroth moment ( $M_0$ ) and average volume ( $\mu_a(V)$ ) in R2 using the DSA, SWA; and outflow rescaling and particle deletion.

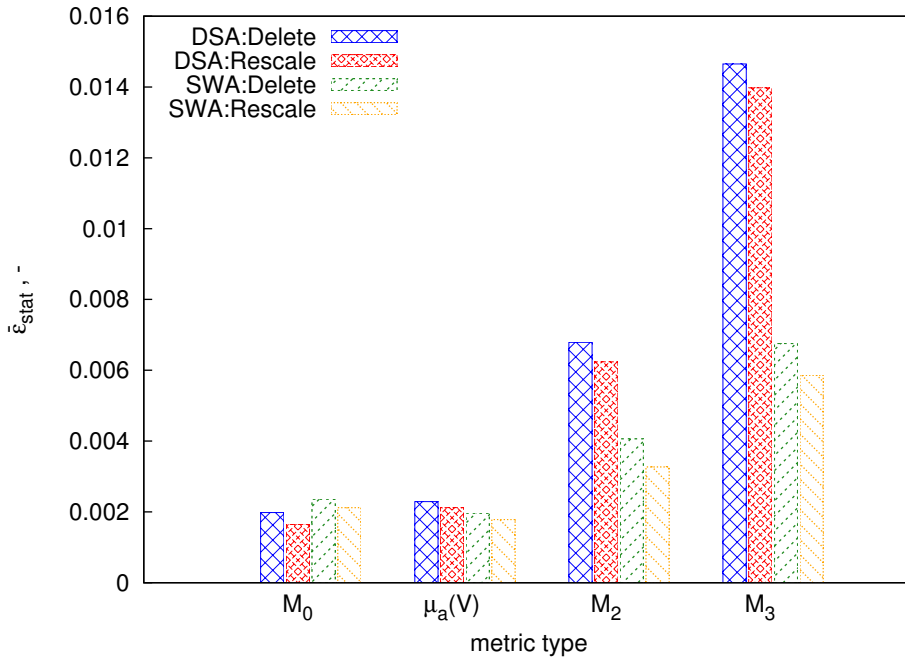


**Figure 5.5:** Comparison of the normalised average statistical error ( $\bar{\epsilon}_{\text{stat}}$ ) in selected process metrics in R2 ( $f_R = 0$ ) using the DSA, SWA; and outflow rescaling and particle deletion ( $N_{\text{max}} = 16384$ ,  $L = 160$ ).

SWA. Similar behaviour of the SWA was reported in [93].

The previous discussion focused on the reduction of systematic error as a function of numerical parameters. Using Equation (2.33), the relative amount of statistical error present in each case can also be compared. These results are presented in Figure 5.5.

Only in the zeroth moment does DSA appear to have a slight advantage in terms of reducing statistical error. For all other cases (particularly the higher moments), the SWA shows up to a 45% reduction in average uncertainty, which is consistent with previous studies [93, 122]. The outflow rescaling process type appears to contribute less statistical error than its particle deletion counterpart. This is unsurprising, since the removal of a particle from the ensemble deletes information that could otherwise be preserved in a rescaling approach.

### 5.2.3 Networks with recycle loops

Chemical engineering process models may often include a ‘recycle stream’ [46], where material or energy is transferred from a downstream to an upstream unit operation. The stochastic solution of the population balance equation has only recently been studied with such networks [67]. As such, this section aims to investigate some of the preliminary characteristics of the stochastic particle algorithm where feedback loops are present.

The normalised average error in R2 with respect to the Discrete Model was evaluated for the network in Figure 5.2(a) using the test particle mechanism with  $f_R = 0.5$  ( $N_{\max} \times L = 10 \times 2^{18}$ ), and is presented in Figure 5.6.

In contrast to the results of Figure 5.4, it is evident the system is more sensitive to the number of computational particles. The linear decrease in the metrics’ average error (slope of -1) with  $N_{\max}$  is consistent with other studies of convergence of stochastic particle methods [25, 53, 99]. Only for the zeroth moment does the DSA outperform the SWA for reduction of error as a function of  $N_{\max}$ . Both methods appear to converge by the same threshold;  $N_{\max} = 4096$ .

In addition to recycling material (gas-phase and particles), a feedback loop could also recycle statistical error. Using outflow rescaling, the transient evolution of the statistical error in  $M_3$  was evaluated (Equation (2.32)) in R3 for different values of the recycle fraction. These results are displayed in Figure 5.7.

As the recycle fraction increases, so does the ‘noise’ in the solution. Use of the SWA is particularly advantageous in this system, in some cases showing more than an order of magnitude less statistical error than the DSA. The same phenomenon is observed for all other metrics, with the exception of  $M_0$ . In the case of  $M_0$ , the statistical error is so small that any potential advantage of DSA is outweighed by the error accumulation in the other metrics.

Although the statistical errors appear to stabilise as the reactor reaches steady-state, the statistical error in the DSA solutions is concerningly large; reaching more than 20% for  $f_R = 0.8$ . In practical use of stochastic population balance modelling, it is uncommon to use 160 independent runs (8 is more common: [90, 143]), as the computational expense can be too great. Since the statistical error is dependent on the number of runs, it fol-

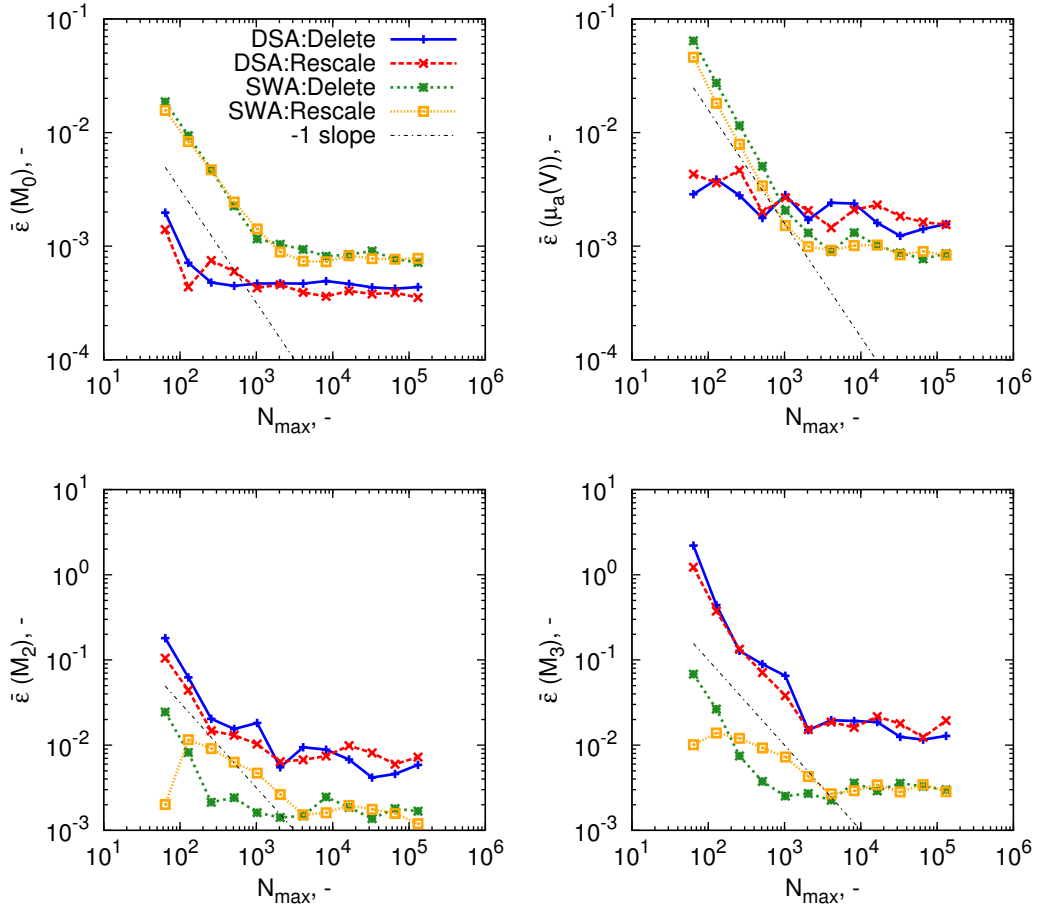


**Figure 5.6:** Convergence of the zeroth moment ( $M_0$ ), average volume ( $\mu_a(V)$ ) and second and third mass moments ( $M_2$ ,  $M_3$ ) for the second reactor (R2) in a countercurrent network with  $f_R = 0.5$ .

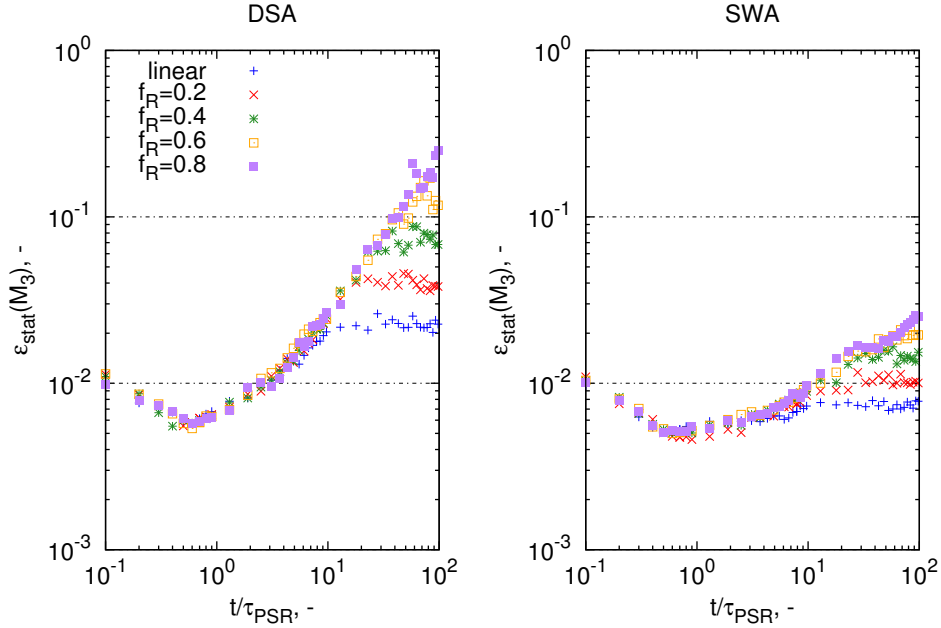


**Figure 5.7:** Normalised statistical error in R3 as a function of dimensionless reactor time and recycle fraction ( $N_{\max} = 16384$ ,  $L = 160$ ).

lows from these results that a SWA should be used in place of the DSA for networks with strong feedback.

#### 5.2.4 Reactors with multiple inlets

The previous analyses addressed linear reactor networks and those which recycle information through the network for a system with three reactors. It is also important to understand the effect of increasing the length of the reactor network and the contribution of material from inflow streams to a reactor. The Damköhler number is typically used to investigate the latter phenomenon, and is defined here as:

$$Da = \frac{1/\tau_{\text{coag}}^{\text{in}}}{1/\tau_{\text{PSR}}} \quad (5.18)$$

where  $\tau_{\text{coag}}$  is the characteristic coagulation time, given by  $1/(K^{\text{const}}M_0)$  [91]. By varying the Damköhler number of a stream, the effect of an increased coagulation rate upon the test system can be assessed. To do this, the system given in Figure 5.2(b) with length  $N_{\text{reac}} = 10$  reactors and inflow

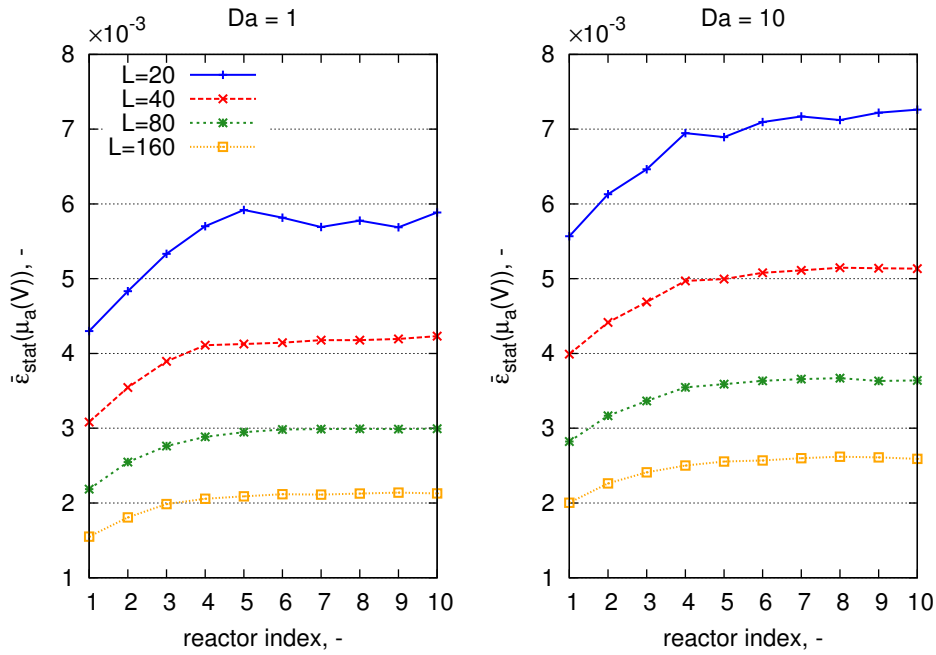


**Figure 5.8:** Normalised average statistical error in the mean particle volume as function of reactor index ( $N_{\max} = 16384$ , SWA coagulation).

fraction  $f = 0.5$  was used. The statistical error in each reactor as a function of the inflow Damköhler number was determined and is given in Figure 5.8.

The error measurements increase through the length of the PSR chain, before leveling-off after five reactors. Where more coagulation occurs (higher  $Da$ , right panel), the error is increased. This analysis illustrates how error can potentially propagate through a reactor chain, although in this particular example the error is sufficiently low to be of no concern. It is suggested that for systems where particle processes (e.g. coagulation, surface growth) occur over much shorter characteristic times than the transport time, more independent runs or computational particles could be used to offset the accumulation of statistical error.

## 5.3 Applications

### 5.3.1 Approximation of a PFR

Many aerosol synthesis processes use a tubular hot-wall reactor or similar method to manufacture nanoparticles [75, 99, 141, 163]. These processes are typically modelled using a plug-flow reactor (PFR) model, where the length coordinate of the reactor is translated into a time coordinate to permit solution of the population balance equations. However, this formulation does not permit investigation of the transient behaviour of the flow reactor, as the time coordinate actually refers to the distance through the reactor.

In development of the plug-flow reactor model, it is typically assumed that the reactor is composed of infinitesimally thin ‘plugs’. Supposing that a PFR with constant volume  $V$  has a constant volumetric flowrate  $Q$ , the residence time of each reactor is given by:

$$\tau_{\text{PFR}} = \frac{V}{Q} \quad (5.19)$$

Approximating the PFR as a series of  $N_{\text{reac}}$  perfectly-stirred reactors, the residence time of each reactor (or plug) is straightforwardly calculated:

$$\tau_{\text{PSR}} = \frac{\tau_{\text{PFR}}}{N_{\text{reac}}} \quad (5.20)$$

Under this approximation, the ability to model networks of flow reactors with the stochastic particle method permits the transient response of the population balance equations in a PFR to be determined. That is, both the time and the reactor length coordinates can be treated independently. This is relevant to reactor start-up and operation.

For practical purposes, it is useful to know how many PSRs are needed to accurately approximate the true PFR solution. This will be a function of the relative timescales of the particle processes with respect to the transport timescale. The Damköhler number is again used to measure the relative influence of coagulation; however the characteristic transport time  $\tau$  is here taken to be the residence time of the PFR being approximated by the PSR network (i.e.  $Da = \tau_{\text{PFR}}/\tau_{\text{coag}}$ ). To investigate the difference of a network solution to the PFR solution, the ‘average PFR error’  $\bar{\epsilon}_{\text{PFR}}$  is first defined. For a reactor network composed of  $N_{\text{reac}}$  PSRs, each with residence time  $\tau_{\text{PSR}}(Da)$ ; the error in the network’s solution with respect to the PFR solu-

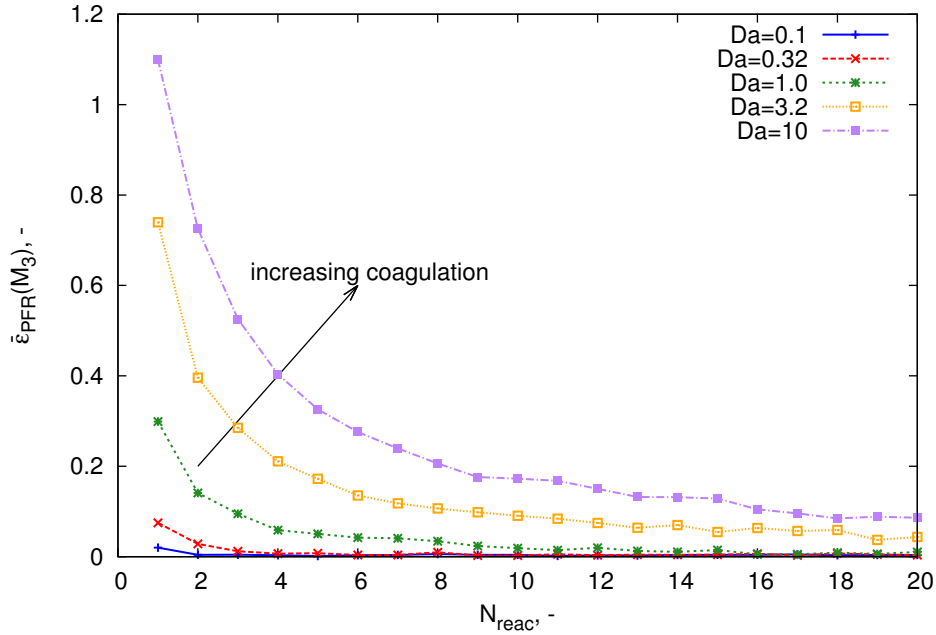


**Figure 5.9:** Normalised average error in  $M_3$  of the networked-PSR solution with respect to the PFR solution for particles undergoing coagulation (transition kernel).

tion is given by:

$$\bar{\epsilon}_{PFR}^{(Da, N_{reac})} = \frac{1}{N_{reac}} \sum_i^{N_{reac}} \frac{|\xi_{Ri}^{(Da)}(t_{SS}) - X_{PFR}^*(i\tau_{PSR})|}{X_{PFR}^*(i\tau_{PSR})} \quad (5.21)$$

where  $\xi_{Ri}$  is the mean of metric  $X(t)$  in reactor  $i$  of the network over  $L$  runs (Equation (2.28)), and  $X_{PFR}^*$  the PFR solution for that metric. The number of reactors required to approximate a PFR was studied for a system of particles undergoing a physical coagulation process (transition kernel, Equation (2.22)) with no inception or surface growth. The results for a variety of Damköhler numbers are given in Figure 5.9.

It is clear that when the relative influence of coagulation is small (low  $Da$ ), the PSR network approximation to a PFR is valid for a small number of reactors, and the magnitude of the error is very small. This approximation appears to become less useful as the coagulation process occurs faster, relative to the transport time. It is again illustrated in Figure 5.10, where the zeroth moment is plotted for various  $(Da, N_{reac})$  pairs.

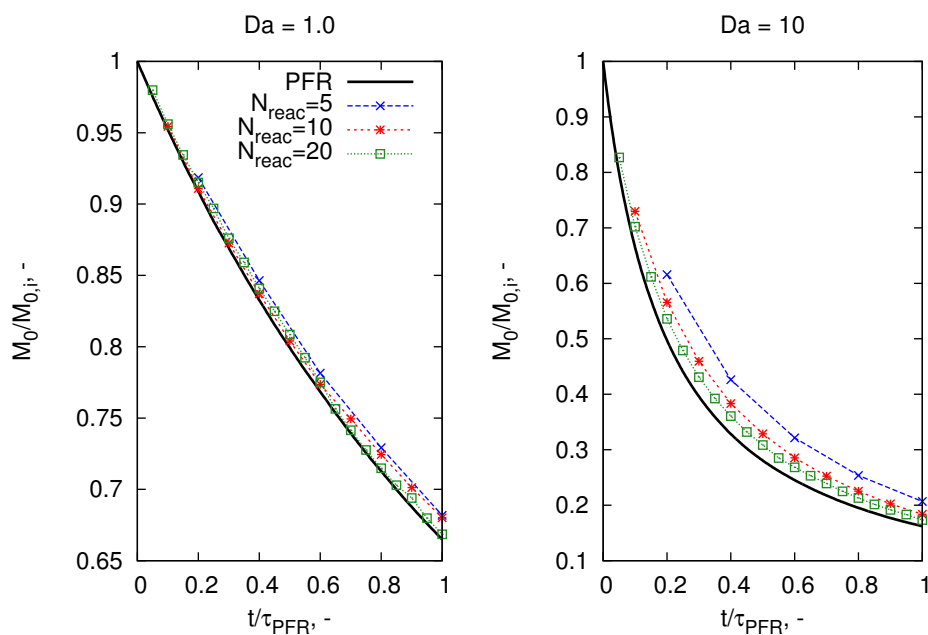


**Figure 5.10:** Temporal evolution of  $M_0$  normalised by its initial value ( $M_{0,i}$ ) of a reactor chain compared to the PFR solution.

## 5.4 Conclusions

This work has presented an algorithm to solve a reactor network with a fully-coupled gas-phase and stochastic population balance solver. The algorithm uses sequential modular simulation to solve the network in a stepwise fashion. Novel processes for accounting for particle in- and outflow were proposed.

The convergence properties of the network solution algorithm were assessed in order to identify suitable choices for numerical parameters. A choice of 4096 computational particles was recommended to minimise systematic error. A new algorithm for simulating particle outflow (termed volume ‘rescaling’) was also shown to be advantageous in reducing statistical error. Two algorithms for coagulation were considered: the direct simulation algorithm and a stochastic weighted algorithm. It was found that the SWA algorithm showed superior reduction of systematic and statistical error for almost all properties of the particle ensemble. The direct simulation algorithm was found to be unsuitable for networks with strong feedback.

To illustrate potential applications of this methodology, a plug flow reactor was approximated as a linear series of perfectly-stirred reactors. The number of PSRs required to approximate such a system as a function of coagulation rate was assessed. It was evident that many reactors are likely to be necessary when particle processes occur on a faster timescale than particle transport.

## Chapter 6

# A detailed model for silicon nanoparticle synthesis

*A novel multivariate particle model to simulate the synthesis of silicon nanoparticles across a wide range of process conditions is presented.*

*Material from this chapter has been published in [90].*

Silicon nanoparticles were traditionally considered as an unwanted contaminant formed as a by-product of semiconductor manufacture [41, 104] during the thermal decomposition of silane ( $\text{SiH}_4$ ). Today, they have a variety potential applications as a new material, particularly when made to a specific size and shape [7, 58, 86, 102]. As particle properties are primarily controlled by the complex decomposition mechanism of silane, it is necessary to understand the processes involved in this mechanism in order to make particles of a given diameter and morphology. In this chapter, a new model will be presented to simulate these processes leading to particle formation.

The thermal decomposition of silane begins with the collision and activation of the silane molecule [63, 125, 129, 159]. It then breaks down and recombines into other silanes, silenes (doubly-bound silicon hydrides, e.g.  $\text{SiH}_2\text{SiH}_2$ , suffixed 'A' [149]) and silylenes (radical species, e.g.  $\text{SiH}_3\text{SiH}$ , suffixed 'B'), gradually increasing in size until it is treated as a particle or deposited on a surface.

This ‘clustering’ mechanism of gas-phase silicon hydrides has been investigated in a number of ways. For example, the decomposition of monosilane (and higher silanes) has been analysed using shock tubes [77, 159], rotating-disk reactors, [63] plasma discharge [154] and gas chromatography [16, 129]. Accompanying these studies are the numerical models of the decomposition process. Many models of varying degree of complexity have been proposed, from the ‘simple’ three-step reaction of Purnell and Walsh [129]; to the popular mechanism of Swihart and Girshick [149]; who proposed a mechanism containing 2615 reactions and 221 silicon hydride species, up to Si<sub>20</sub>. Quantum chemical calculations and automatic mechanism generation have also been used to further develop these mechanisms [1, 160]. An excellent review of the current understanding of the silane pyrolysis mechanism and in particular, its pressure dependence, is given by Petersen and Crofton [125].

The heterogeneous reaction of silicon hydrides at silicon surfaces has also been studied in detail. Houf et al. [64] identified that silanes react with a silicon surface according to a dissociation-absorption-hydrogen mechanism, assuming that silenes and silylenes collide with surfaces with a sticking coefficient of unity. Further, it was reported that the rate of evolution of hydrogen from silicon hydride surfaces is proportional to the coverage of hydrogen at the surface [64, 147]. These mechanisms were incorporated into the kinetic mechanism of Ho et al. [63] in a detailed model of the chemical vapour deposition process of silicon.

Like the gas-phase mechanism, silicon particle synthesis has been widely investigated. Early studies focused on the process conditions required to observe the onset of nucleation of particles; with a view to suppressing particle formation so as to yield higher-quality semiconductors [41, 101]. Since then, several groups have used a variety of experimental methodologies to study silicon particle synthesis. Cannon et al. [22] used CO<sub>2</sub> laser heating to analyse the decomposition of silane and subsequent formation of particles in inert gases. A series of papers [23, 44, 95, 96] expanded the initial work to encompass the effect of process conditions upon the properties of silicon films deposited through laser-heating of silane.

The decomposition of silane is also sensitive to specific microwave frequencies. This was used in several studies to form photoluminescent silicon nanoparticles, or ‘quantum dots’ in a tubular microwave reactor [51, 58,

72]. It was reported that control of the microwave power (and therefore the temperature profile) allowed for fine adjustment of the primary particle size.

The Flagan group conducted impressively-detailed experimental studies into nucleation of silicon in single- [103, 162, 163] and multi-stage [135, 161] tubular hot-wall reactors. In all cases, different heating zones were used to tightly control the temperature profile of the reacting gas. Depending on the reactor configuration and the imposed temperature profile; particles of different size and morphology could be obtained. In typical reactor operation, it was reported that coagulation and sintering would control particle growth unless care was taken to reduce the number concentration of particles as produced by homogeneous nucleation [103].

These process conditions were recently identified by Körmer et al. [75], who produced narrowly-distributed silicon nanoparticles in a hot-wall tubular reactor with dilute silane mixtures ( $\sim 4\%$ ) at low pressures (2500 Pa) and high temperatures (900–1100°C). Population balance modelling was used to confirm that heterogeneous reaction of silicon hydrides at the particle surface was predominantly responsible for particle growth [56, 76, 92].

There have been a number of other attempts to use population balance modelling to understand silicon nanoparticle formation. Nguyen and Flagan [103] used a fine-seed model to investigate the effect of pressure and temperature upon particle structure. Kruis et al. [79] employed homogeneous nucleation theory to elucidate the process conditions leading to onset of nucleation. This was expanded upon by Nijhawan et al. [104], who coupled the gas-phase mechanism of Swihart and Girshick [149] with a population balance model for a spray reactor. The kinetic mechanism of Swihart and Girshick [149] was also used in a two-dimensional fully-coupled model incorporating the effect of fluid and particle dynamics [31, 32]; illustrating the relative importance of the various interconnected particle processes involved in synthesis.

Much work has been undertaken on the chemical and physical properties of particles obtained from silane thermal decomposition. Onischuk et al. [110] used a flow reactor to produce particles with specific hydrogen content and chemical bond structure. Subsequent works used kinetic and population balance modelling approaches to analyse kinetic pathways through which particles were formed [111, 112, 114]. Aggregate particles

were studied in [113], in which particles were synthesised at low temperatures under finite-rate sintering conditions.

Silane decomposition at above-atmospheric pressure was addressed theoretically and experimentally by Odden et al. [107], where it was reported that particle size was independent of initial silane pressure. Additional mechanistic pathways (in comparison to the mechanism of Ho et al. [63]) were also proposed to account for the observed reaction rates at these process conditions [108, 109].

The aerosol dynamics models described previously are typically ‘validated’ by comparison of theoretical predictions of particle size distributions (PSDs) against those obtained experimentally. These are often obtained via direct transmission electron microscope (TEM) imaging [75], or, in older work, though differential mobility analysers and condensation nuclei counters [103, 162]. However, despite the wealth of information available about experimental configurations, PSDs and mechanistic pathways, no effort has been made to unify the conclusions of these previous studies.

The key aim of this chapter therefore is to develop a new model with a detailed type-space to accurately predict the size and morphology of silicon nanoparticles synthesised from the thermal decomposition of silane across a range of different process conditions. The stochastic particle method coupled with a gas-phase ordinary differential equation solver is employed to achieve this.

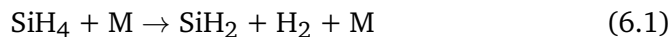
The structure of this chapter is as follows. The gas-phase and particle models are explained in Section 6.1. The parameter estimation procedure applied to the gas-phase mechanism is outlined in Section 6.2. The numerical results are discussed in Section 6.3.1, while the model predictions are compared with experimental data in Section 6.3.2. The chapter is concluded by an evaluation of the model and discussion of further avenues for research.

## 6.1 Model development

### 6.1.1 Gas-phase kinetic model

Much study has been carried out into the decomposition of silanes. For conditions of practical interest, the rate of decomposition of silane can be

written as the bimolecular expression [125]:



where M is a third body. It is well-understood that silane decomposition proceeds through a series of intermediate gas-phase species, such as silylene ( $\text{SiH}_2$ ) and higher silenes/silanes (e.g.  $\text{Si}_3\text{H}_8$ ). Thus, silicon decomposition mechanisms are often presented with many subsequent reactions after the initial decomposition step. Such examples include the work of Ho et al. [63] and Swihart and Girshick [149]. The presence of these appended ‘clustering’ reactions accelerates precursor decomposition [125].

This work adopts the mechanisms proposed by Ho et al. [63] to describe the chemical kinetics involved in silane decomposition and is given in full in Table 6.1. Note that the reactions for the species “Si” are omitted. Where appropriate, the low-pressure limit parameters (according to a Lindemann form falloff reaction, Equation 2.11) or reverse parameters are given. This mechanism was chosen in place of more recent [1, 125] or more detailed [49, 52, 149] kinetics due to sound testing at atmospheric pressure [63], relative simplicity and provision of pressure-dependent reactions.

The system of ordinary differential equations describing the reactions of Table 6.1 was solved using *MOPS*’ ODE solver and the in-house developed chemical kinetics library *Sprog* for a zero-dimensional batch reactor configuration. In order to gain better agreement with experimental data, pre-exponential factors for five reactions were adjusted. The reasons for this are discussed in Section 6.2.

### 6.1.2 Particle model

#### Type-space

The binary-tree model from Section 3.1 is used for the particle model in this chapter. Each primary particle is described by the number of silicon atoms  $\eta_{\text{Si}}$  and hydrogen atoms  $\eta_{\text{H}}$ :

$$p_x = p_x(\eta_{\text{Si}}, \eta_{\text{H}}) \quad (6.2)$$

The derived properties of the type-space are identical to those given for the binary-tree particle model in Table 3.1. Here, the value of the fractal

**Table 6.1:** Gas-phase mechanism employed. Parameters in bold have been adjusted from their original referenced values (see Section 6.2). Pre-exponentials are given with units in terms of cm, mol, s.

No.	Reaction	$A$ cm, mol, s	$n$ -	$E_A$ kcal/mol	Ref.
1	$\text{SiH}_4 (+M) \rightleftharpoons \text{SiH}_2 + \text{H}_2 (+M)$	$3.2 \times 10^9$	1.7	54.7	[63]
	low-pressure parameters	<b><math>4.0 \times 10^{12}</math></b>	0	45.1	[125]
2	$\text{Si}_2\text{H}_6 (+M) \rightleftharpoons \text{SiH}_4 + \text{SiH}_2 (+M)$	$1.8 \times 10^{10}$	1.7	50.2	[63]
	low-pressure parameters	<b><math>1.8 \times 10^{35}</math></b>	-10.4	56.0	[63]
3	$\text{Si}_2\text{H}_6 (+M) \rightleftharpoons \text{Si}_2\text{H}_4\text{B} + \text{H}_2 (+M)$	$9.1 \times 10^9$	1.8	50.2	[63]
	low-pressure parameters	<b><math>7.8 \times 10^{40}</math></b>	-7.8	59.0	[63]
4	$\text{Si}_3\text{H}_8 (+M) \rightleftharpoons \text{SiH}_2 + \text{Si}_2\text{H}_6 (+M)$	$7.0 \times 10^{12}$	1.0	52.7	[63]
	low-pressure parameters	$1.7 \times 10^{69}$	-15.1	60.5	[63]
5	$\text{Si}_3\text{H}_8 (+M) \rightleftharpoons \text{Si}_2\text{H}_4\text{B} + \text{SiH}_4 (+M)$	$3.7 \times 10^{12}$	1.0	50.9	[63]
	low-pressure parameters	<b><math>4.4 \times 10^{66}</math></b>	-17.3	59.3	[63]
6	$\text{Si}_2\text{H}_4\text{B} (+M) \rightleftharpoons \text{Si}_2\text{H}_4\text{A} (+M)$	$2.5 \times 10^{13}$	0.2	5.4	[63]
	low-pressure parameters	$1.1 \times 10^{33}$	-5.8	9.2	[63]
7	$\text{Si}_2\text{H}_4\text{B} + \text{H}_2 \rightleftharpoons \text{SiH}_4 + \text{SiH}_2$	$9.4 \times 10^{13}$	0	4.1	[63]
	reverse parameters	$9.4 \times 10^{10}$	1.1	5.7	[63]
8	$\text{Si}_2\text{H}_4\text{B} + \text{SiH}_4 \rightleftharpoons \text{Si}_2\text{H}_6 + \text{SiH}_2$	$1.7 \times 10^{14}$	0.4	8.9	[63]
	reverse parameters	<b><math>5.2 \times 10^{11}</math></b>	0.1	8.5	[63]

dimension ( $D_f$ ) is assumed to be 1.59, taken from the silicon particle synthesis work of Rogak et al. [135]. Their work also provides an expression to estimate the mobility diameter of particles in the free-molecular regime:

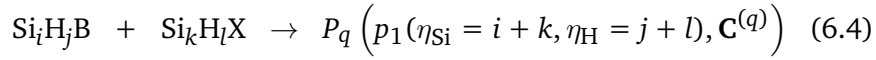
$$d_{\text{mob}}^{\text{fm}} = \overline{d_{\text{pri}q}} \sqrt{0.802(n_q - 1) + 1} \quad (6.3)$$

### 6.1.3 Particle processes

Particles may be created and changed according to a number of processes.

#### Inception

Particles are created in the population balance according to a general inception reaction, where silylene can collide with a silene or another silylene to form particles:



where  $P_q(p_1(\eta_{\text{Si}}, \eta_{\text{H}}), \mathbf{C}^{(q)})$  is the  $(N(t) + 1)^{\text{th}}$  particle, with  $\eta_{\text{Si}}$  silicon atoms and  $\eta_{\text{H}}$  hydrogen atoms and X is A (silene) or B (silylene). This inception mechanism is consistent with that proposed by Giunta et al. [52]. The rate of inception is given by:

$$R_{\text{incep}} = \begin{cases} \frac{1}{2} N_{\text{A}}^2 c_{\text{Si}_i\text{H}_j\text{B}} c_{\text{Si}_k\text{H}_l\text{X}} K^{\text{tr}}(\text{Si}_i\text{H}_j\text{B}, \text{Si}_k\text{H}_l\text{X}) & d_q \geq d^* \\ 0 & d_q < d^* \end{cases} \quad (6.5)$$

where  $d_q$  is the incepting diameter of the particle  $P_q$  resulting from collision of species  $\text{Si}_i\text{H}_j\text{B}$  and  $\text{Si}_k\text{H}_l\text{X}$ .  $c_{\text{Si}_i\text{H}_j\text{B}}$  and  $c_{\text{Si}_k\text{H}_l\text{X}}$  refer to the gas-phase concentrations of the colliding species and  $K^{\text{tr}}$  is the transition regime coagulation kernel (given in Equation (2.22)). The variable  $d^*$  is the critical nucleus diameter, representing the threshold above which gas-phase species may convert to particles. It is calculated using the Kelvin equation [76, 79]:

$$d^* = \frac{4 \gamma_{\text{Si}} v_1}{k_{\text{B}} T \ln(S_{\text{Si}})} \quad (6.6)$$

$v_1$  is the volume of silicon monomer and  $\gamma_{\text{Si}}$  is the surface energy of silicon, given by [76]:

$$\gamma_{\text{Si}} = 1.152 - 1.574 \times 10^{-4} T(\text{K}) \text{ N/m} \quad (6.7)$$

$S_{Si}$  is the supersaturation of silicon, given by the ratio of silicon partial pressure to saturation vapour pressure of silicon:

$$S_{Si} = \frac{P_{Si}}{P_{Si,sat}} \quad (6.8)$$

In the present work, the silicon partial pressure is approximated using the sum of partial pressure of silylenes. The following correlation is used for the saturation vapour pressure [55, 76]:

$$P_{Si,sat} = 10^{7.5341 - \frac{23399}{T(K)}} \text{ atm} \quad (6.9)$$

When the incepting diameter  $d_q$  exceeds the critical nucleus diameter, the rate of inception is calculated using the transition regime coagulation kernel.

### Coagulation

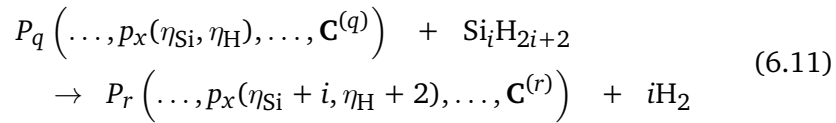
Coagulation of particles results in the usual change to the type-space for the binary-tree particle model:

$$\begin{aligned} P_q(p_1, \dots, p_{n_q}, \mathbf{C}^{(q)}) + P_r(p_1, \dots, p_{n_r}, \mathbf{C}^{(r)}) \\ \rightarrow P_s(p_1, \dots, p_{n_q}, p_{n_q+1}, \dots, p_{n_q+n_r}, \mathbf{C}^{(s)}) \end{aligned} \quad (6.10)$$

The rate of coagulation is calculated using the transition regime coagulation kernel.

### Surface reaction

This work adopts a version of the ‘dissociation-adsorption-hydrogen’ mechanism, originally proposed by Sinniah et al. [147]. Silanes ( $\text{SiH}_4$ ,  $\text{Si}_2\text{H}_6$ ,  $\text{Si}_3\text{H}_8$ ) react with the particle surface, releasing hydrogen. A primary  $p_x$  of particle  $P_q$  is transformed as:



where  $\mathbf{C}^{(r)}$  is the new connectivity matrix resulting from the addition of surface area. The change in connectivity matrix ( $\mathbf{C}^{(q)} \rightarrow \mathbf{C}^{(r)}$ ) is given by Equation (4.8). The rate of surface reaction is modelled as an Arrhenius process; and is also proportional to the surface area of particle,  $S_q$ :

$$R_{SR} = A_{SR, \text{Si}_i\text{H}_{2i+2}} S_q c_{\text{Si}_i\text{H}_{2i+2}} \exp\left(-\frac{E_{A,SR}}{RT}\right) \quad (6.12)$$

**Table 6.2:** Heterogeneous reaction processes included in the present work. Parameters in bold have been adjusted from their original referenced values (see Section 6.2). Surface reaction pre-exponentials have units cm/mol s and hydrogen release pre-exponentials have units 1/s and condensation scaling factors are dimensionless.

Reaction	Type	A cm, mol, s	$E_A$ kcal/mol	Ref.
$\text{SiH}_4 + p_x \rightarrow p_x(\eta_{\text{Si}} + 1, \eta_{\text{H}} + 2) + \text{H}_2$	S.R.	<b><math>3.0 \times 10^{33}</math></b>	37.5	[63]
$\text{SiH}_2 + p_x \rightarrow p_x(\eta_{\text{Si}} + 1, \eta_{\text{H}} + 2)$	cond	1.0	-	[63]
$\text{Si}_2\text{H}_6 + p_x \rightarrow p_x(\eta_{\text{Si}} + 2, \eta_{\text{H}} + 2) + 2\text{H}_2$	S.R.	<b><math>3.0 \times 10^{34}</math></b>	37.5	[63]
$\text{Si}_2\text{H}_4\text{A} + p_x \rightarrow p_x(\eta_{\text{Si}} + 2, \eta_{\text{H}} + 4)$	cond.	1.0	-	[63]
$\text{Si}_2\text{H}_4\text{B} + p_x \rightarrow p_x(\eta_{\text{Si}} + 2, \eta_{\text{H}} + 4)$	cond.	1.0	-	[63]
$\text{Si}_3\text{H}_8 + p_x \rightarrow p_x(\eta_{\text{Si}} + 3, \eta_{\text{H}} + 2) + 3\text{H}_2$	S.R.	<b><math>3.0 \times 10^{34}</math></b>	37.5	[63]
$p_x \rightarrow p_x(\eta_{\text{Si}}, \eta_{\text{H}} - 2) + \text{H}_2$	$\text{H}_2$	<b><math>1.2 \times 10^{19}</math></b>	47.0	[147]

where  $A$  and  $E_A$  are the Arrhenius parameters for silane species  $\text{Si}_i\text{H}_{2i+2}$ . The Arrhenius parameters are estimated by the fitting procedure, explained in detail in Section 6.2. These reactions and parameters are given in Table 6.2. The Arrhenius parameters for  $\text{Si}_2\text{H}_6$  and  $\text{Si}_3\text{H}_8$  were set to ten times that of  $\text{SiH}_4$ , consistent with the observations of Buss et al. [21] and as done in previous models [63, 104].

### Condensation

Particles can grow by the deposition of silenes and silylenes on the particle surface. The state-space of the particle is modified according to:

$$\begin{aligned}
 P_q \left( \dots, p_x(\eta_{\text{Si}}, \eta_{\text{H}}), \dots, \mathbf{C}^{(q)} \right) + \text{Si}_i\text{H}_j\text{X} \\
 \rightarrow P_r \left( \dots, p_x(\eta_{\text{Si}} + i, \eta_{\text{H}} + j), \dots, \mathbf{C}^{(r)} \right)
 \end{aligned} \tag{6.13}$$

This may be modelled as a collisional process, with rate given by:

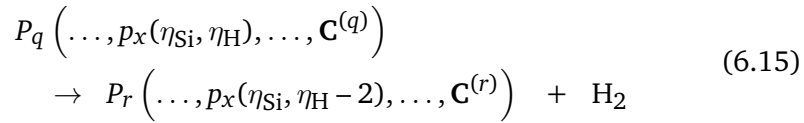
$$R_{\text{cond}} = A_{\text{cond}} c_{\text{Si}_i\text{H}_j\text{X}} \sqrt{\frac{\pi k_B T}{2 m_{\text{Si}_i\text{H}_j\text{X}}}} \left( d_{\text{Si}_i\text{H}_j\text{X}} + d_{\text{col},q} \right)^2 \tag{6.14}$$

where  $A_{\text{cond}}$  is the collisional efficiency of the process (assumed 1.0, consistent with [63] for silylenes),  $m_{\text{Si}_i\text{H}_j\text{X}}$  and  $d_{\text{Si}_i\text{H}_j\text{X}}$  are the mass and diameter of the colliding species respectively, and  $d_{\text{col},q}$  is the collision

diameter of particle  $q$ . These processes are again summarised in Table 6.2.

### Hydrogen release

The hydrogen content of a silicon nanoparticle is a strong function of temperature and annealing time [95, 96, 147]. The present model therefore includes a stochastic jump process to account for release of hydrogen from particles:



A study of hydrogen desorption from a silicon hydride film found that the rate of desorption was first-order in coverage of hydrogen [147]. Here, the hydrogen coverage  $\theta$  is estimated by the ratio of number of hydrogen atoms to silicon atoms in each particle:

$$\theta(P_q) = \frac{\sum_{x=1}^{n_q} p_x(\eta_{\text{H}})}{\sum_{x=1}^{n_q} p_x(\eta_{\text{Si}})} \quad (6.16)$$

It is assumed that the common surface element remains unchanged due to the loss of hydrogen from the particle surface ( $\mathbf{C}^{(q)} = \mathbf{C}^{(r)}$ ). The rate of hydrogen desorption is proportional to the coverage, given here by the ratio of number of hydrogen to number of silicon atoms:

$$R_{\text{H}_2} = A_{\text{H}_2} \theta_q \exp \left( -\frac{E_{\text{A,H}_2}}{RT} \right) \quad (6.17)$$

The pre-exponential parameter  $A_{\text{H}_2}$  is adjusted according to the methodology in Section 6.2, and  $E_{\text{A,H}_2}$  is given in Table 6.2

### Sintering

Sintering is implemented using the exponential excess surface area decay formula given in Equation (3.18). In this model, the sintering parameters suggested by Kruis et al. [78] are used. These parameters account for sintering through a grain-boundary diffusion process, with the characteristic time given by:

$$\tau_{\text{S}} = A_{\text{S}} d^{n_{\text{S}}} T \exp \left( \frac{E_{\text{S}}}{RT} \right) \quad (6.18)$$

where  $A_{\text{S}}$ ,  $n_{\text{S}}$  and  $E_{\text{S}}$  are empirical parameters.

**Table 6.3:** Numerical and model parameters used in the silicon model.

Description	Symbol	Value	Ref.
<i>Numerical parameters</i>			
Maximum splitting timestep	$\Delta t_s$	$2.5 \times 10^{-4}$ s	[143]
Max. number of stochastic particles	$N_{\max}$	16,384	[143]
Number of runs	$L$	8	[143]
<i>Model parameters</i>			
Maximum zeroth moment	$M_{0,\max}$	$1.0 \times 10^{14}$ #/m <sup>3</sup>	-
Sintering pre-exponential	$A_S$	$1.15 \times 10^{13}$ s/m <sup>4</sup>	[78]
Sintering diameter power	$n_S$	4	[78]
Sintering characteristic energy	$E_S$	55.0 kcal/mol	[78]
Surface smoothing factor	$\sigma_{SR}$	1.0	[144]
Density of silicon	$\rho_{Si}$	2329 kg/m <sup>3</sup>	-
Density of hydrogen	$\rho_H$	101 kg/m <sup>3</sup>	-
Free-molecular enhancement factor	$k_{fm}$	1.0	-
<i>Process settings</i>			
Temperature range	$T$	800–1400 °C	-
Residence time range	$\tau$	0.001–1.0 s	-
Initial fraction of SiH <sub>4</sub> range	$y_{SiH_4}$	0.0004–1.0	-
Total pressure range	$P$	2500–101,325 Pa	-

#### 6.1.4 Coupling algorithm

The gas-phase kinetic model and the particle population balance are coupled using an operator-splitting algorithm with Strang splitting [25, 26]. The Linear Process Deferment Algorithm is used to accelerate linear processes such as surface reaction and condensation (see Section 2.2.2). The full algorithm though which this occurs for an analogous particle model is described by Shekar et al. [143]. The numerical and model parameters used for the fully-coupled model are summarised in Table 6.3.

## 6.2 Parameter estimation

Previous studies have identified that, at low pressure, use of literature gas-phase mechanisms (e.g. that of Swihart and Girshick [149]) requires scaling of either the gas-phase pre-exponentials [56, 76, 92] or scaling of the nucleation rate [104]. In some cases, both the kinetic parameters and the nucleation rates (via usage of collision efficiencies) were empirically adjusted to obtain model fits [113, 114]. Thus, it is necessary to choose appropriate parameter values to ensure theoretical results are comparable with experimental results.

Of the reactions included in the gas-phase mechanisms, Petersen and Crofton [125] noted that the silane and silylene concentration was most sensitive to Reactions 1 and 7 (given in Table 6.1). Onischuk et al. [114] additionally reported that fitting of Reactions 1 and 3 was required for their population balance model. Preliminary calculations indicated that adjustment of the pre-exponentials of Reaction 5 and Reaction 8 (reverse) was necessary to achieve agreement with experimental work. As silane decomposition occurs at the low-pressure limit [125] up to 5 atm the low-pressure pre-exponentials were adjusted, where available.

As in previous studies, the surface reaction [56, 76, 92] and hydrogen release [114] rates were adjusted via the pre-exponential factors. In total, there are seven parameters which require estimation. This system's parameter vector is therefore given by:

$$\mathbf{x} = \left( A_{1,LP}, A_{2,LP}, A_{3,LP}, A_{5,LP}, A_{8,rev}, A_{SR,SiH_4}, A_{H_2} \right) \quad (6.19)$$

To choose an appropriate set of parameters  $\mathbf{x}$ , a staged optimisation methodology analogous to those given in [92] was employed. Firstly, low-discrepancy (Sobol) sequences were used to locate four parameter sets close to minima, as defined by objective function  $\Phi(\mathbf{x})$ :

$$\Phi(\mathbf{x}) = \sum_{i=1}^{N_{exp}} \left( \phi_i^{exp} - \phi_i^{sim}(\mathbf{x}) \right)^2 \quad (6.20)$$

where  $\phi_i$  represents one of the datasets used in fitting, listed in Table 6.4. The superscript 'exp' refers to an experimentally-sourced dataset, and 'sim' that obtained from simulation. A selection of studies using a range of

**Table 6.4:** Experimental data used in fitting the model.  $\sigma_a(d_{\text{pri}})$  refers to the arithmetic standard deviation of the primary diameter.

$i$	$T$	$y_{\text{SiH}_4}$	$P$	$\tau$	$\phi_i$	$\phi_i^{\text{exp}}$ , nm	Ref.
1	1100	4.0	2.5	0.08	$d_{\text{pri,mode}}$	26.7	[75]
2	1100	4.0	2.5	0.08	$\sigma_a(d_{\text{pri}})$	1.7	[75]
3	1100	4.0	2.5	0.08	$d_{\text{pri},10}$	24.1	[75]
4	1100	4.0	2.5	0.08	$d_{\text{pri},90}$	28.8	[75]
5	900	4.0	2.5	0.42	$d_{\text{pri,mode}}$	21.2	[75]
6	580	5.0	39.0	0.53	$d_{\text{pri,mode}}$	41.0	[113]
7	816	3.3	51.0	0.0026	$d_{\text{pri,mode}}$	11.0	[49]
8	1047	3.3	51.0	0.0021	$d_{\text{pri,mode}}$	11.0	[49]

process conditions were used, and equal weighting was applied to each of the datasets used in the objective function. The bounds for the Sobol scans were found empirically. The four best parameter sets from the initial parameter space scan are further refined by applying the simultaneous stochastic approximation algorithm (SPSA) [62]; the best of which  $\mathbf{x}^*$  is chosen according to:

$$\mathbf{x}^* = \arg \min_{\mathbf{x}} \{\Phi(\mathbf{x})\} \quad (6.21)$$

The optimal set of parameters is obtained via use of the Bayesian approach of Mosbach et al. [100] and Braumann et al. [17]. Using an Inverse-Wishart prior (as the error in the experimental values is unknown), a Metropolis-Hastings algorithm is employed to estimate the posterior distribution of the parameters. A fourth-order response surface was constructed locally around the point  $\mathbf{x}^*$  in order to reduce the time needed for the many model evaluations required by the sampling algorithm. This methodology provides an estimate of the modal value of each parameter in  $\mathbf{x}$  and its corresponding uncertainty.

## 6.3 Results and discussion

### 6.3.1 Numerical results

The model parameters and their credible intervals as obtained from the parameter estimation procedure are given in Table 6.5. A qualitative under-

**Table 6.5:** Optimal parameters obtained from the parameter estimation procedure. The mode, upper and lower bounds are those of the high probability density region for a 99.99% credible interval.

Parameter	Units	Lower bound	Mode	Upper bound
$A_{1,LP}$	$\text{cm}^3/\text{mol.s}$	$3.2 \times 10^{12}$	$4.0 \times 10^{12}$	$5.8 \times 10^{12}$
$A_{2,LP}$	$\text{cm}^3/\text{mol.s}$	$3.8 \times 10^{33}$	$1.8 \times 10^{35}$	$2.8 \times 10^{37}$
$A_{3,LP}$	$\text{cm}^3/\text{mol.s}$	$2.1 \times 10^{39}$	$7.8 \times 10^{40}$	$1.8 \times 10^{43}$
$A_{5,LP}$	$\text{cm}^3/\text{mol.s}$	$1.7 \times 10^{54}$	$8.4 \times 10^{55}$	$1.4 \times 10^{58}$
$A_{8,rev}$	$\text{cm}^3/\text{mol.s}$	$8.1 \times 10^{10}$	$5.2 \times 10^{11}$	$7.0 \times 10^{13}$
$A_{SR, SiH_4}$	$\text{cm}^3/\text{mol.s}$	$1.1 \times 10^{33}$	$3.0 \times 10^{33}$	$1.3 \times 10^{34}$
$A_{H_2}$	1/s	$1.2 \times 10^{19}$	$3.08 \times 10^{20}$	$6.3 \times 10^{20}$

standing of sensitivity of the objective function  $\Phi(\mathbf{x})$  to each parameter can be gained from this information. For example, the credible intervals of  $A_{1,LP}$  and  $A_{SR, SiH_4}$  are within an order of magnitude of the modal value, indicating that the accuracy of the model is strongly dependent on correct estimation of these values. In comparison, the bounds for  $A_{3,LP}$  span four orders of magnitude, suggesting that  $\Phi(\mathbf{x})$  is less sensitive to this value.

As the objective function is very sensitive to Reaction 1 and previous studies [125] have identified it as the most important step in governing the decomposition rate, it is worthwhile to discuss the value of  $A_{1,LP}$  obtained here through model-fitting. Table 6.6 lists the low-pressure parameters for Reaction 1 for several other studies: one used in a mechanism to describe chemical vapour deposition (CVD) of silane [63], another obtained through detailed experimental studies [125], and the others used for coupling with particle models [49, 76, 92, 123].

There is clearly a large variation in values of the pre-exponential, especially when the additional temperature fitting power  $n$  is used. It is useful to use a unimolecular rate constant ( $k_{1b}$ ) when comparing the reaction rates predicted by each set of parameters [125]. Here, it is given by:

$$\frac{dc_{SiH_4}}{dt} = -k_1 c_{SiH_4} c_M = -k_{1b} c_{SiH_4} \quad (6.22)$$

This rate constant is compared across the kinetic models of Table 6.6 in Figure 6.1. It is evident that the rate constants in pure gas-phase models (e.g. [63, 125]) are three to four orders of magnitude greater than those

**Table 6.6:** Comparison of other kinetic expressions for the low-pressure limit of Reaction 1.

Study	$A$ cm <sup>3</sup> /mol.s	$n$ -	$E_A$ kcal/mol
Ho et al. [63]	$5.2 \times 10^{29}$	-3.5	57.6
Frenklach et al. [49]	$1.2 \times 10^{47}$	-8.8	67.2
Petersen and Crofton [125]	$7.2 \times 10^{15}$	0	45.1
Paur et al. [123]	$1.3 \times 10^{12}$	0.68	58.0
Körmer et al. [76]	$9.0 \times 10^{12}$	0	45.1
Menz et al. [92]	$5.1 \times 10^{10}$	0	45.1
this work	$4.0 \times 10^{12}$	0	45.1

coupled to particle models [49, 76, 92, 123]. Even within the set of those coupled to particle models, the unimolecular rate constant spans three orders of magnitude. The rate expression found in this thesis (from parameter estimation) appears to correspond well with that of Körmer et al. [76].

It is hypothesised that  $k_{1b}$  reported here is a result of fitting an overall inception rate to the experimental case studies. As already discussed, models developed for silicon nanoparticle synthesis typically require scaling of the nucleation rate (with a collision efficiency) or silane decomposition rate (as in this case). This clearly indicates that a key challenge is obtaining the correct nucleation rate of ‘seed’ particles. It is therefore hypothesised that when combined with the Equation (6.5), the gas-phase mechanism found through fitting (Table 6.1) provides a correct overall nucleation rate for the experimental cases studies. On its own, the gas-phase mechanism is not physically representative of the real decomposition rate.

After conversion from *SURFACE CHEMKIN* [30] to the type-space of this particle model, the value of  $A_{SR, SiH_4}$  shows good agreement with that proposed by Houf et al. [64] and used in the gas-surface mechanism of Ho et al. [63]. The conversion is given in Appendix B.1.

### 6.3.2 Case studies

There is an overwhelming amount of literature which describes the production of silicon nanoparticles under a variety of process conditions. Several of these cases representing different types of particles or reactor configu-

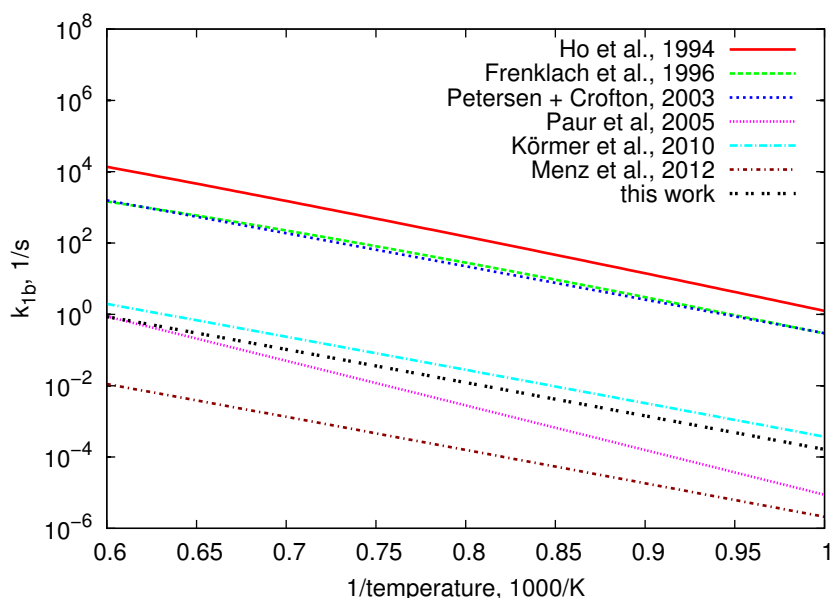


**Figure 6.1:** Dependence of the unimolecular rate constant ( $k_{1b}$ ) upon temperature at 2.5 kPa (conditions of Körmer et al. [75]) for a variety of literature kinetic models.

rations were selected. Those studied in the present work are displayed in Table 6.7. Where available, published temperature profiles were used (e.g. [163]), given in Figure 6.2.

All profiles (e.g. temperature versus length in [45]) were converted from length coordinates to time coordinates assuming plug flow and volumetric flowrates, unless a residence time was supplied. In the cases with no temperature profile (e.g. [113]), the time corresponds to a hot-zone residence time; and a constant temperature was used. PSDs are the number-density distributions and were generated using kernel density estimation and the normal distribution approximation to estimate the bandwidth [146].

### Narrow PSDs

Narrowly-distributed particles are obtained when inception occurs for a very short period of time, coagulation is negligible, and particles are grown by heterogeneous deposition [76, 92]. A detailed study of the production of uniform silicon nanoparticles was conducted by Körmer et al. [75], where particle size could be controlled between 20 and 40 nm through choice of

**Table 6.7:** Experimental data and corresponding process conditions investigated for model comparison.

Study	Reactor	$T$ °C	$y_{\text{SiH}_4}$ %	$P$ (bath) kPa	$\tau$ s
Flint et al. [45]	Laser	700–1000	0.21	20 (Ar)	0.005
Wu et al. [163]	PFR	450–1200	1.0	101 (N <sub>2</sub> )	1.0
Nguyen and Flagan [103]	PFR	500–1200	0.04–1.0	101 (N <sub>2</sub> )	0.9
Frenklach et al. [49]	Shock tube	816–1307	3.3	51 (Ar)	~0.001
Onischuk et al. [113]	PFR	580	5.0	39 (Ar)	0.2–0.8
Körmer et al. [75]	PFR	500–1100	2.0–13.0	2.5 (Ar)	0.08–0.42

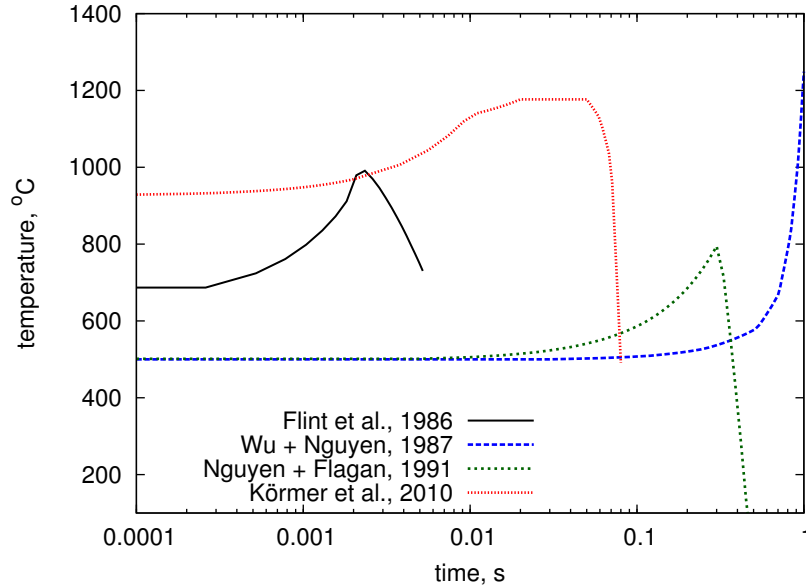


**Figure 6.2:** Experimental temperature profiles used in the model calculations for the case studies of Table 6.7.

process conditions.

Under these conditions, much of the precursor is lost to the wall due to vapour deposition on the reactor surface. In a similar vein to [56], this work assumes that only 16% of the initial precursor reacts to form particles. A temperature profile similar to the optimised profile of Gröschel et al. [56] is used for the 84 ms, 1100°C cases, given in Figure 6.2. The model predictions and experimental results for this system are compared in Figure 6.3.

As previously identified [56, 76, 92], coagulation should be negligible in order to obtain a narrow size distribution. There is reasonable agreement between the model and literature results, especially for greater silane fractions. The secondary and very small tertiary peaks for the ‘base case’ is a result of particles coagulating once or twice. For the higher silane fraction cases, much more silicon in the particle phase yields many more coagulation events, broadening the distribution and ‘smoothing-out’ the additional modal peaks.

At long residence times ( $\tau \sim 420$  ms) the PSDs predicted by the model are far too broad as compared to those observed experimentally [75]. It is evident that in these cases, the model either over-predicts the rate of coagulation or is not capturing some aspect of detail of the real process. It is likely that transport processes should be included in the model for this case study, as there is much precursor lost to the walls, particle size and morphology has a radial dependency [75] and the system is particularly sensitive to the temperature profile imposed [56].

Nucleation of silicon particles in a shock tube was studied by Frenklach et al. [49]. Spherical particles with sizes between 10 and 40 nm and narrow size distributions were produced in the shock tube at a range of process conditions. Experimental PSDs were reported for a 3.3% SiH<sub>4</sub>-Ar mixture with a total pressure of 0.5 atm, and are compared to the theoretical predictions in Figure 6.4.

Very good agreement of theoretical and experimental PSDs is observed for the 816°C and 1307°C cases. However, the modal diameter for the 1047°C case is approximately double that reported in [49]. In a similar vein to the 420 ms cases of Körmer et al. [75] described previously, the broadening observed in this case is associated with too much coagulation.

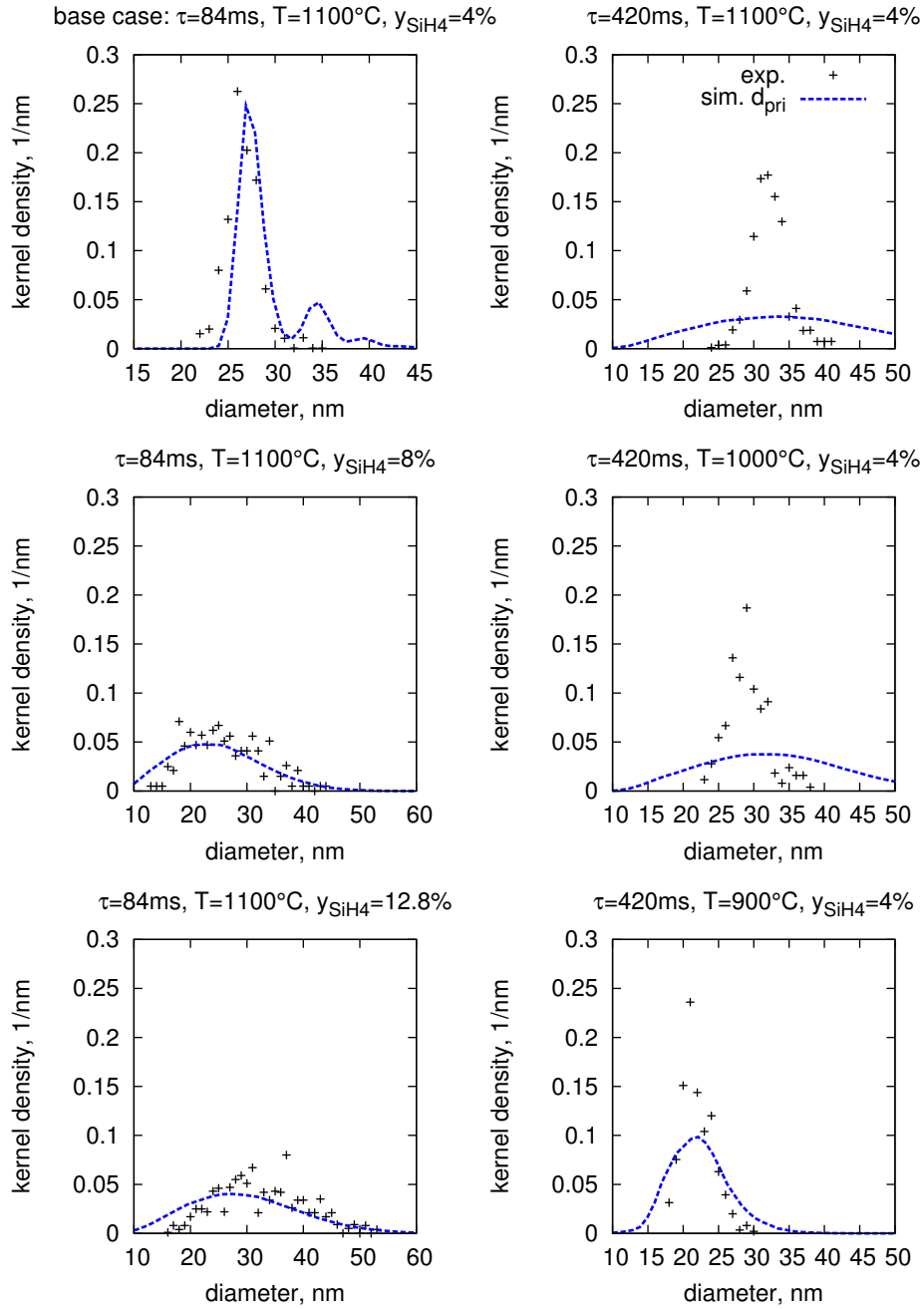


**Figure 6.3:** Comparison of the experimental PSDs of Körmer et al. [75] (crosses) at 25 kPa total pressure (in Ar) and those predicted by the present model (lines).

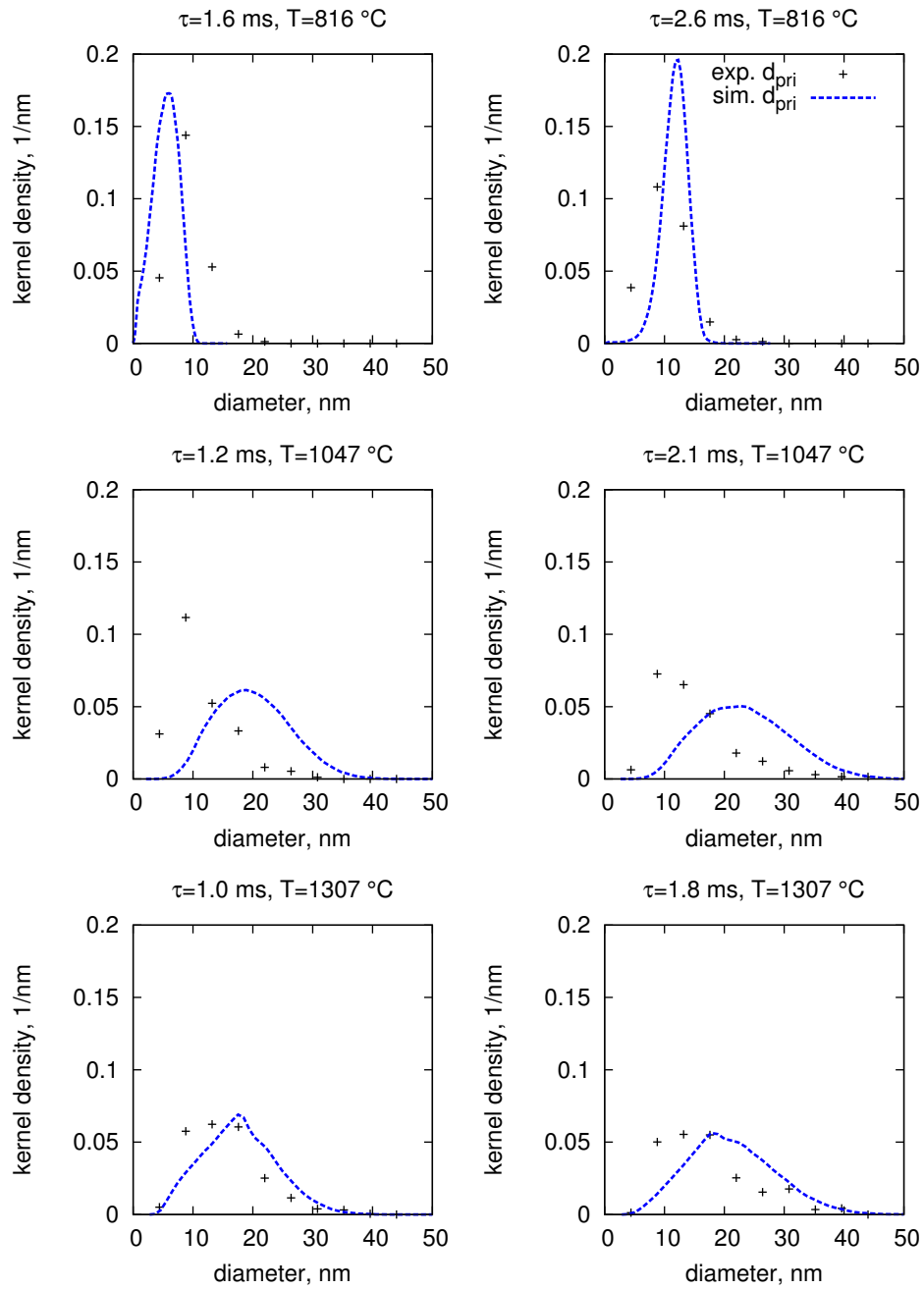


**Figure 6.4:** Comparison of theoretical (lines) and experimental PSDs (crosses) for the shock tube reactor of Frenklach et al. [49] with initial conditions  $y_{\text{SiH}_4}=3.3\%$  (in Ar) and  $P=51$  kPa.

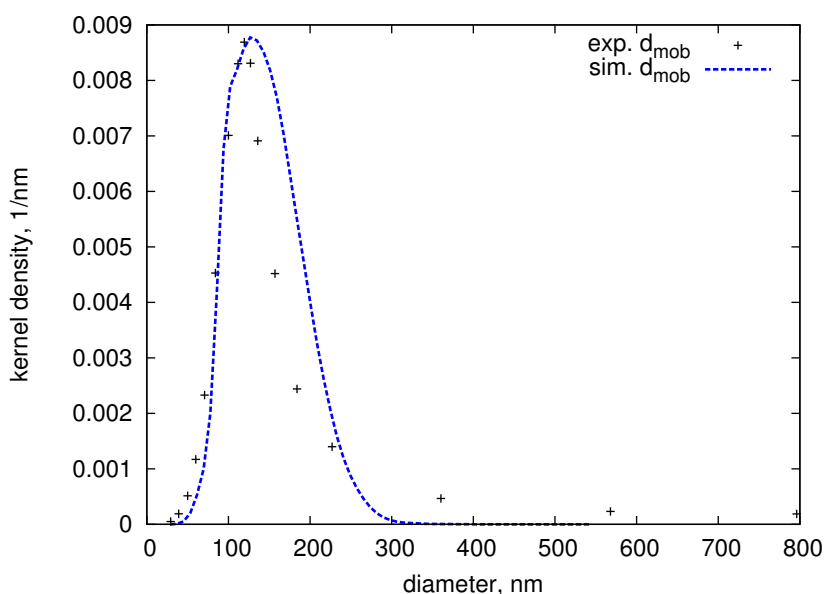


**Figure 6.5:** Comparison of theoretical (lines) and experimental PSDs (crosses) for the system of Wu et al. [163] with initial conditions  $y_{\text{SiH}_4} = 1.0\%$  (in  $\text{N}_2$ ) at atmospheric pressure.

### Sintered particles

Wu et al. [163] used a tubular reactor to generate highly-spherical crystalline silicon particles through coagulation and sintering of smaller particles at a high temperature. A peak temperature of  $1200^\circ\text{C}$  (temperature profile given in Figure 6.2) and initial silane fraction of 1% at atmospheric pressure (in nitrogen) was required to achieve these particles. The resulting particle size distribution is given in Figure 6.5.

The model predictions show excellent agreement with the experimental PSD. The particles predicted by the model are completely spherical, with a geometric standard deviation of 1.50, indicating that the particle size distribution is at the self-preserving limit.

### Particle aggregates

Particle synthesis under conditions of finite-rate sintering was experimentally and theoretically investigated by Nguyen and Flagan [103]. Using a single-stage tubular reactor, they investigated formation of aggregates at different silane concentrations (0.01–1.0%) with a lower peak reactor tem-

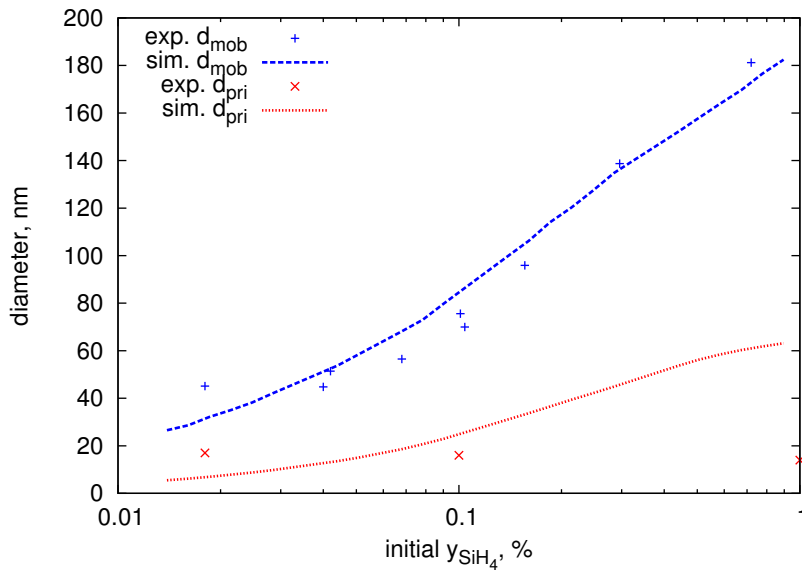


**Figure 6.6:** Dependence of particle size on initial precursor concentration for the system of Nguyen and Flagan [103] with a peak reactor temperature of 800°C .

perature as compared to Wu et al. [163]. This reactor was operated at atmospheric pressure with nitrogen as the bath gas. Their results are compared to those predicted by the present model in Figures 6.6 and 6.7.

It is evident that the theoretically-predicted average mobility diameter and the mobility diameter particle size distributions (Figure 6.7) are in good agreement with the experimental data. However, the primary diameter is too large for silane concentrations above 0.07% (Figure 6.6). This is attributed to the sintering kinetics used; which remain untested in population balances [92].

The formation of particle aggregates was also identified by Onischuk et al. [113] in a detailed examination of the nature of particle structures obtained when sampling from the hot- and cold-zones of the reactor. Aggregates were sampled from inside the reactor, corresponding to various hot-zone residence times and their primary particle structure analysed. The model and experimental results are compared in Figure 6.8 for a constant temperature of 580°C and initial conditions of 5% silane in argon at 39 kPa.

Excellent agreement is observed between the model predictions of the temporal evolution of the average primary diameter and the experimental

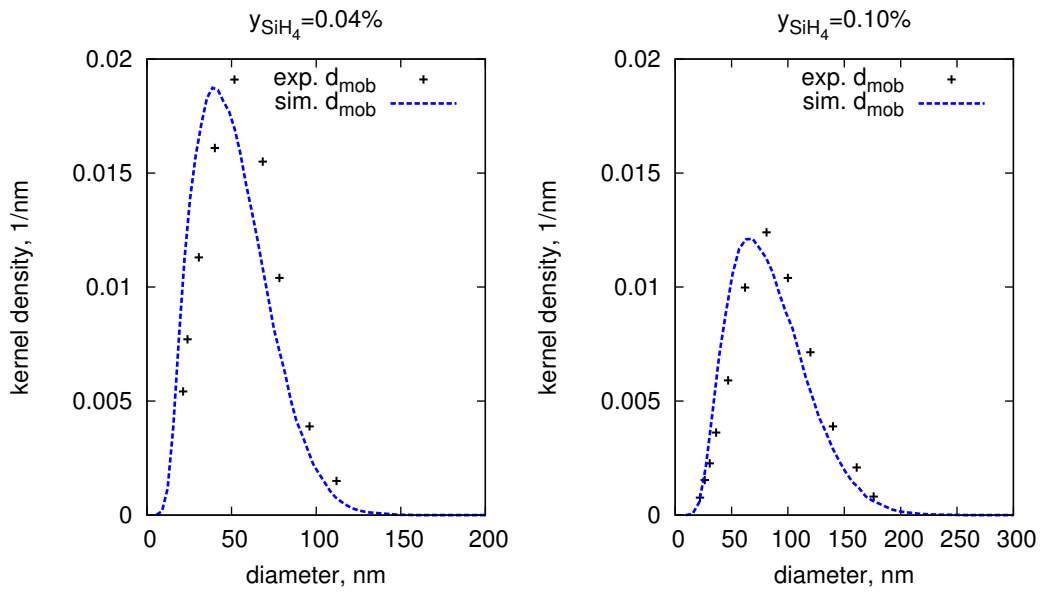


**Figure 6.7:** Comparison of theoretical (lines) and experimental PSDs (crosses) for the conditions of Nguyen and Flagan [103] with a peak reactor temperature of 800°C .

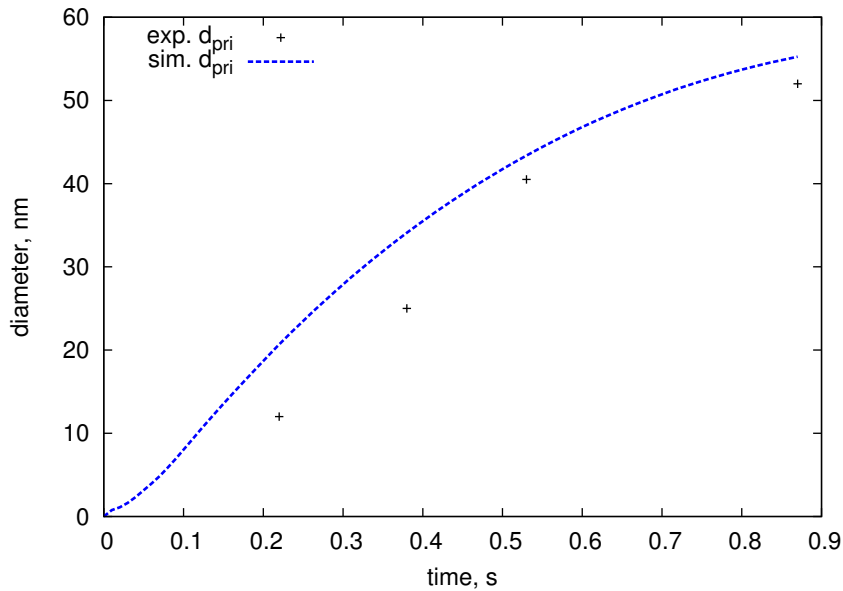


**Figure 6.8:** Temporal evolution of the mean primary particle diameter for the conditions of Onischuk et al. [113] with initial conditions  $y_{\text{SiH}_4} = 5\%$  (in Ar) at 39 kPa and 580°C .

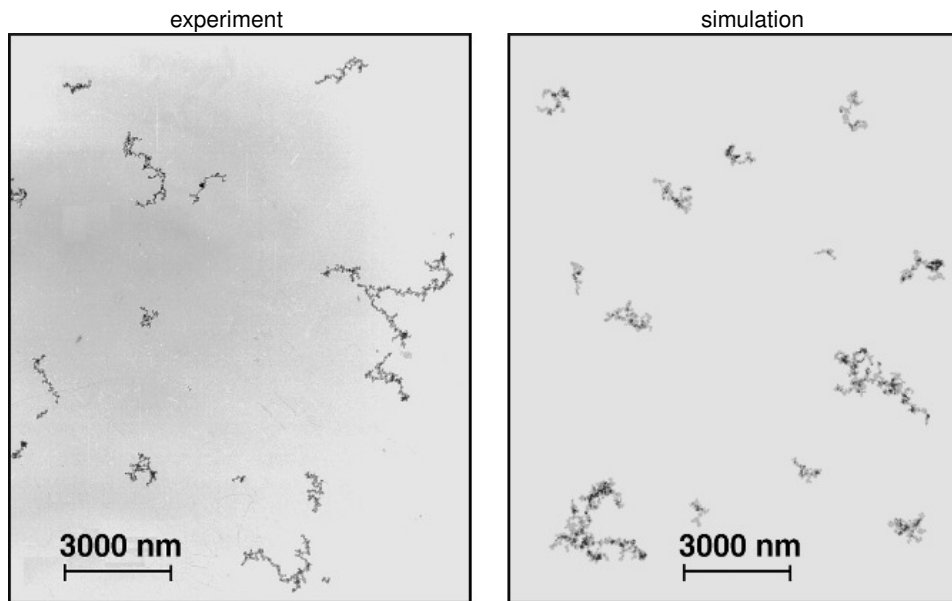


**Figure 6.9:** An experimental TEM micrograph from the work of Onischuk et al. [113] (left panel) compared with a computer-generated TEM-style image from the present work’s model (right panel) for 0.53 s reaction time followed by 17.8 s in the reactor ‘cold zone’. Particle images were rendered using POV-Ray [124].

results. In order to compare particle aggregates, a TEM-style image was generated from model results by assuming that primary particles randomly adhere to each other (Figure 6.9). Here, it is clear that there is at least qualitative agreement with aggregate size and structure.

### Laser synthesis of particles

Silicon particles can also be synthesised in a laser-driven flame [22, 23, 44, 45]. These studies varied process conditions such as silane fraction and cell pressure to produce highly spherical and loosely-agglomerated particles. The particle size and number density was tracked through the flame using laser-scattering measurements. To convert the temperature-length profiles given in [45], the velocity of the particles was estimated using the formula provided in [44]:

$$v = \frac{2 Q_{\text{STP}} T/273}{\pi r^2 P_{(\text{atm})}} \quad (6.23)$$

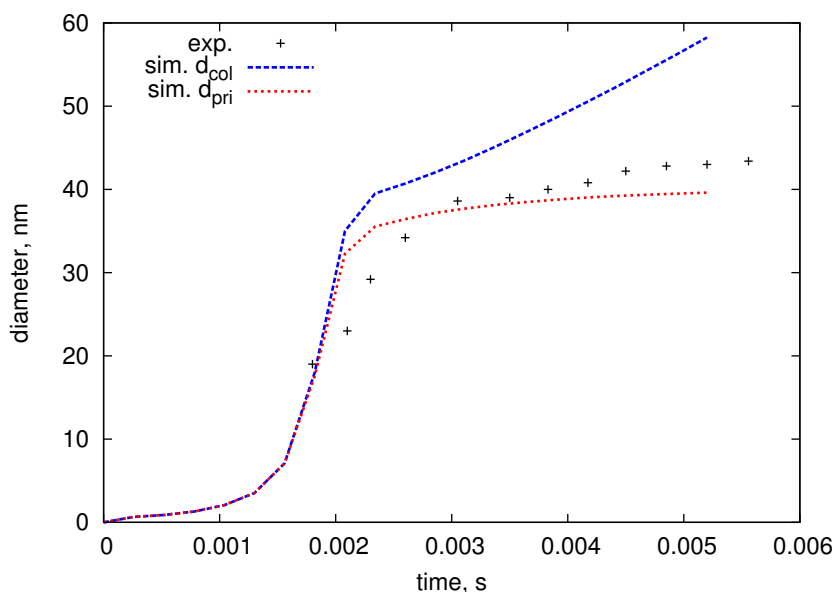


**Figure 6.10:** Evolution of mean particle diameter for the laser-driven flame (case 630S) of Flint et al. [45] and Cannon et al. [23].

where  $Q_{STP}$  is the volumetric silane flow at standard temperature and pressure and  $r$  is the radius of the flame. Thus, using the velocity through the flame, the temperature-time profiles were obtained. The experimental data and model predictions for this system are supplied in Figure 6.10 for the 630S powder (see [45] for more information about different powder codes), assuming  $109 \text{ cm}^3/\text{s}$  of silane [45] and  $400 \text{ cm}^3/\text{s}$  of argon [22] in the inlet stream.

The new model gives reasonable agreement with the experimental trajectories when comparing the primary particle diameter to the experimentally observed diameter. The separation of  $d_{col}$  and  $d_{pri}$  at approximately 0.003 s represents the peak of the temperature profile, where the reaction has gone to completion and aggregates begin to form.

## 6.4 Conclusions

A novel fully-coupled gas-phase and particle model for the synthesis of silicon nanoparticles was presented. The mechanism of Ho et al. [63] was used to describe the gas-phase kinetics. A multidimensional particle model track-

ing the number of silicon and hydrogen units of each primary particle and the connectivity of the primaries in an aggregate was used in conjunction with a population balance model to study nanoparticle synthesis.

By adjusting the pre-exponential factors of five gas-phase and two heterogeneous reactions, good fit to a variety of experimental studies was obtained. The model was applied to different reactor configurations, process conditions and particle morphologies. Varying degrees of fit of theoretical results with experimental results were obtained, with the model generally better for atmospheric pressure cases. The robustness of this modelling methodology was demonstrated by generating a TEM-style image of silicon aggregates in qualitative agreement with experiment.

It was hypothesised that, when combined with the inception process, the new gas-phase mechanism with adjusted parameters accurately described the silicon particle inception rate. It was, however, noted that gas-phase mechanism is unlikely to represent the physical rate of decomposition of silicon hydrides. A key challenge in developing a physical model for silicon nanoparticle formation is resolving this issue.

It was reported that in some cases where aggregate particles were produced, or where large amounts of coagulation occurred, the primary diameter was larger than that observed experimentally. This was attributed to the finite-rate sintering kinetics employed. As this area is generally poorly characterised (particularly in terms of experimental work) for silicon, it is suggested that the model could be significantly improved by using an accurate sintering expression. Despite this, the model successfully knits-together many of the historical studies of silicon nanoparticle synthesis and provides a foundation on which the space of process conditions can be reliably explored.

## Chapter 7

# Putting it all together

*The new methods developed in Chapters 3–5 are applied to the experimental case Wu et al. [163] with the new silicon particle mechanism.*

*Material from this chapter has been published in [91, 94].*

The advances in modelling presented in Chapters 3–5 have so far only been applied to a general population balance model, or for the silica particle model of Shekar et al. [144]. In this chapter, the methods developed in Chapters 3–5 will be applied to the new model for silicon nanoparticle synthesis presented in Chapter 6. It is intended that this should illustrate potential uses for such methods.

The experimental system of Wu et al. [163] will be investigated using the new model and methods. This case was selected as it represented a relatively simple hot-wall reactor system and showed good agreement with experimental results (Figure 6.5). In Section 7.1, the case will be analysed with different particle models, while in Section 7.2, a linear network of reactors will be used to investigate the unsteady-state response of the hot-wall reactor.

### 7.1 Particle model analysis

In Chapter 3, the use of different particle models was investigated. It was identified that use of a particular particle model can strongly alter the solution of the population balance model. The calculations done in that analysis were for a generic implementation of the binary-tree particle model, and

did not include factors such as a reactive gas-phase or surface growth on particles.

Here, the analysis of Chapter 3 will be expanded by combining the spherical and surface-volume particle models with the new mechanism for silicon nanoparticle formation given in Chapter 6. The key aim is to assess how different particle models behave in a ‘real-life’ modelling application.

To do this, characteristic times for coagulation and sintering of the particle ensemble are first defined. The characteristic coagulation time is estimated using the average properties of the ensemble:

$$\tau_C(t) = \frac{1}{M_0(t)K^{tr}(\mu_a[d_{col}](t), \mu_a[m](t))} \quad (7.1)$$

where the average mass and average diameter are substituted into Equation (2.22) for  $K^{tr}$ . The expression of Equation (6.18) for sintering is non-linear. Thus, the three particle models will begin to diverge when sintering moves from effectively instantaneous (very small particles) to finite-rate. This transition is best approximated by use of the maximum primary particle diameter, hence the characteristic sintering time is given by:

$$\tau_S(t) = \tau_S(\max[d_{pri}](t), T(t)) \quad (7.2)$$

The evolution of important particle and ensemble characteristics for this model, as applied to the case of Wu et al. [163], is given in Figure 7.1. Note that a temperature profile (increasing from 500°C to 1250°C) is imposed across this simulation (Figure 6.2).

All the models predict that spherical particles are obtained at the end of the process time. However, neither the surface-volume nor the spherical particle model perform comparably to the binary-tree model. The number density ( $M_0$ ) is double the binary-tree model’s prediction, and the average collision diameter ( $\mu_a(d_{col})$ ) 20 % lower. The surface-volume and spherical models predict the occurrence of a secondary nucleation period (at  $t = 0.6s$  in  $M_0$  panel of Figure 7.1), consistent with other spherical particle modelling efforts [103] of this system.

The predictions of the surface-volume model are also very similar to those of the spherical particle model, despite containing a finite sintering rate. It is hypothesised that this is due to the high polydispersity of particles ( $\sigma_g > 3.0$ , Figure 7.1 lower panels) for this case study, resulting in a similar

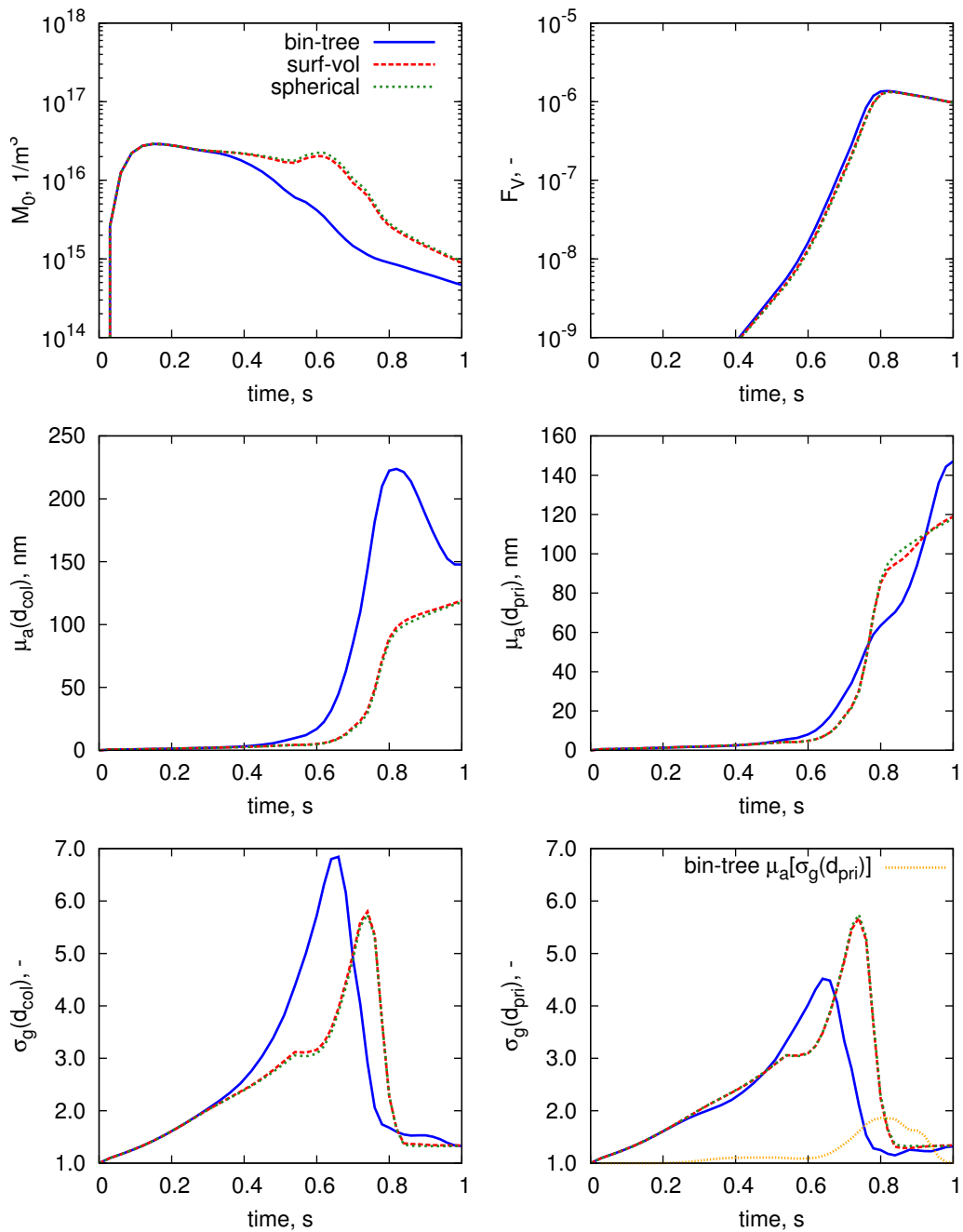


**Figure 7.1:** Comparison of model predictions for the case of Wu et al. [163] using Chapter 6's silicon model. Depicted are the zeroth moment ( $M_0$ ), volume fraction ( $F_V$ ), arithmetic mean ( $\mu_a$ ) and geometric standard deviation ( $\sigma_g$ ) of the collision and primary diameters.

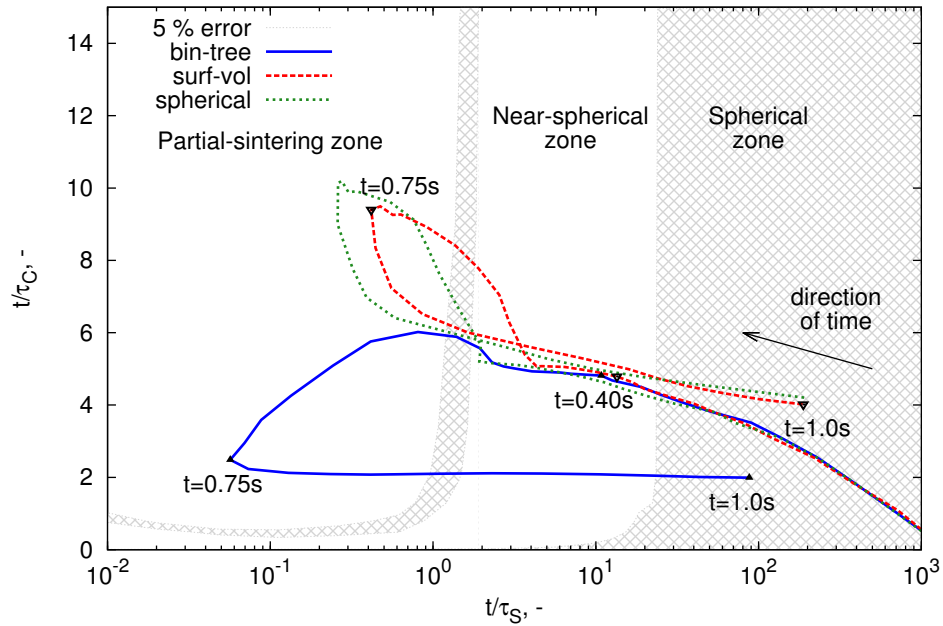


**Figure 7.2:** Trajectory of the case of Wu et al. [163] using Chapter 6’s silicon model through the  $t/\tau_C$ ,  $t/\tau_S$  space. The shading depicts the 5% error margins as described in Figure 3.3. Specific process times for the binary-tree and surface-volume models from Figure 7.1 are labelled,  $t < 0.2$ s omitted for clarity.

‘convergence’ of the two models as depicted in Figure 3.4. To further understand the differences between these models, this case is plotted atop Figure 3.3’s coagulation-sintering map in Figure 7.2.

The system begins with small spherical particles at high  $t/\tau_S$ . The three models diverge from each other after passing through the near-spherical zone. The surface-volume and spherical models subsequently show a large increase in coagulation rate, while it steadily decreases for the binary-tree model. This is due to the secondary nucleation period causing the number density to remain steady (Figure 7.1). The secondary nucleation period is absent for the binary tree model, as the increased surface area of the aggregate particles causes faster depletion of the precursor.

The minimum sintering rate, reached at approximately 0.75 s, represents the point at which the sintering time’s rate of decrease is balanced by the contributions from the rate of increase in particle diameter and rate of

increase in temperature. Past this point, the increasing temperature profile causes coalescence of aggregate structures, returning all models to the spherical zone.

Finally, it is also important to note that the history of the particle ensemble through the  $t/\tau_C$ ,  $t/\tau_S$  space is as important as its location in the space (Figure 7.2). When the particle system moves from one zone to another, it does not imply that all particles have the structure represented by the zone type. Rather, it implies that should the system remain in that zone, as the ensemble's particles will change with time to eventually resemble that of the zone.

## 7.2 Unsteady-state response

In Chapter 5, the reactor network infrastructure was used to approximate a PFR by consecutive PSRs. A SWA was used with the new formulation of the transition regime coagulation kernel developed in Chapter 4 to achieve this with reasonable precision. The same reactor network model will now be used to simulate the unsteady-state response of the hot-wall PFR of Wu et al. [163].

A network of 30 consecutive PSRs was composed, assuming that each PSR is isothermal and has a temperature which corresponds to its location along the PFR (i.e.  $T_i = T(i\tau_{PSR})$ ). This was done to account for the increasing temperature profile through the PFR (Figure 6.2). The initial state of the network is taken to have no particles, but is filled with nitrogen. The transient response of the PSR network was evaluated, allowing sufficient time for the system to reach steady state. The results of this analysis are given in Figure 7.3, where the transient and axial evolution of the particle properties are plotted.

Figure 7.3 (left panel) shows the behaviour of the primary polydispersity, given by the average of the geometric standard deviation of primary diameters in a particle. The 'time through reactor' coordinate refers to the axial position in the reactor, whereas the 'time' axis is the transient response. There is good agreement between the network and PFR solutions in early reactor times (i.e. initial section of PFR length). This agreement appears to decay as coagulation accelerates, similar to Figures 5.9 and 5.10.

The degree of sintering (Figure 7.3, right panel) shows better agreement

— PFR Solution

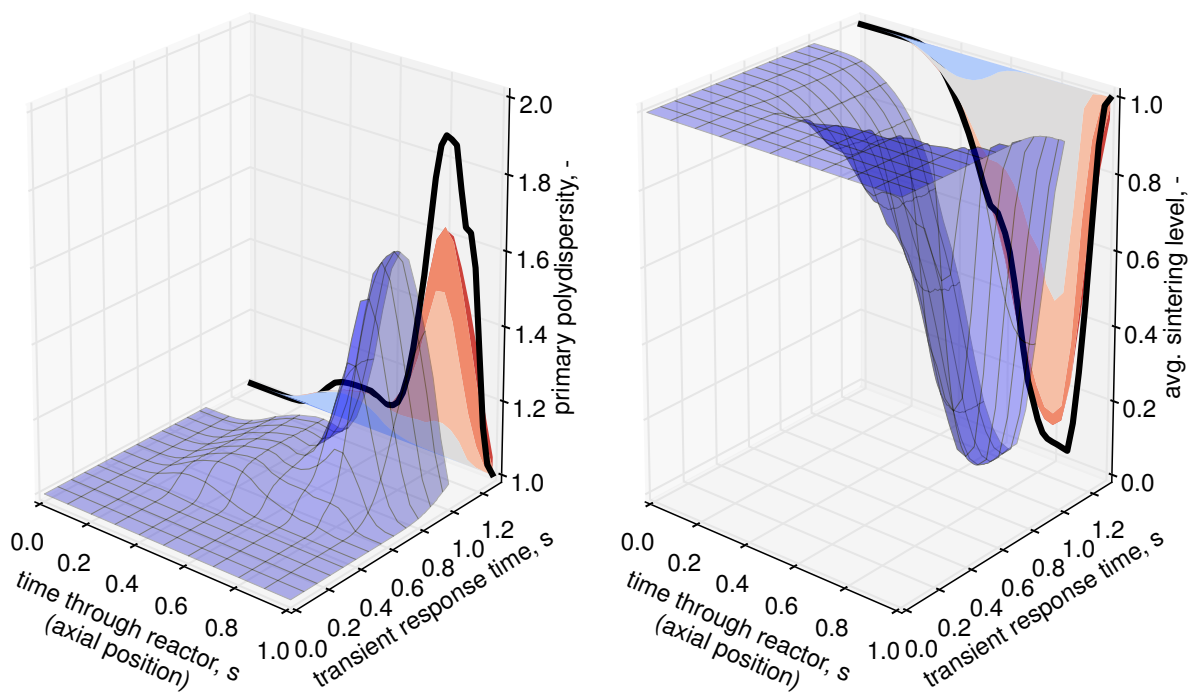


**Figure 7.3:** Mesh plots depicting the transient evolution of the primary polydispersity (given here by the Equation (3.21)) and the degree of sintering. Contour projections of the network solution are compared to the PFR solution (thick line).

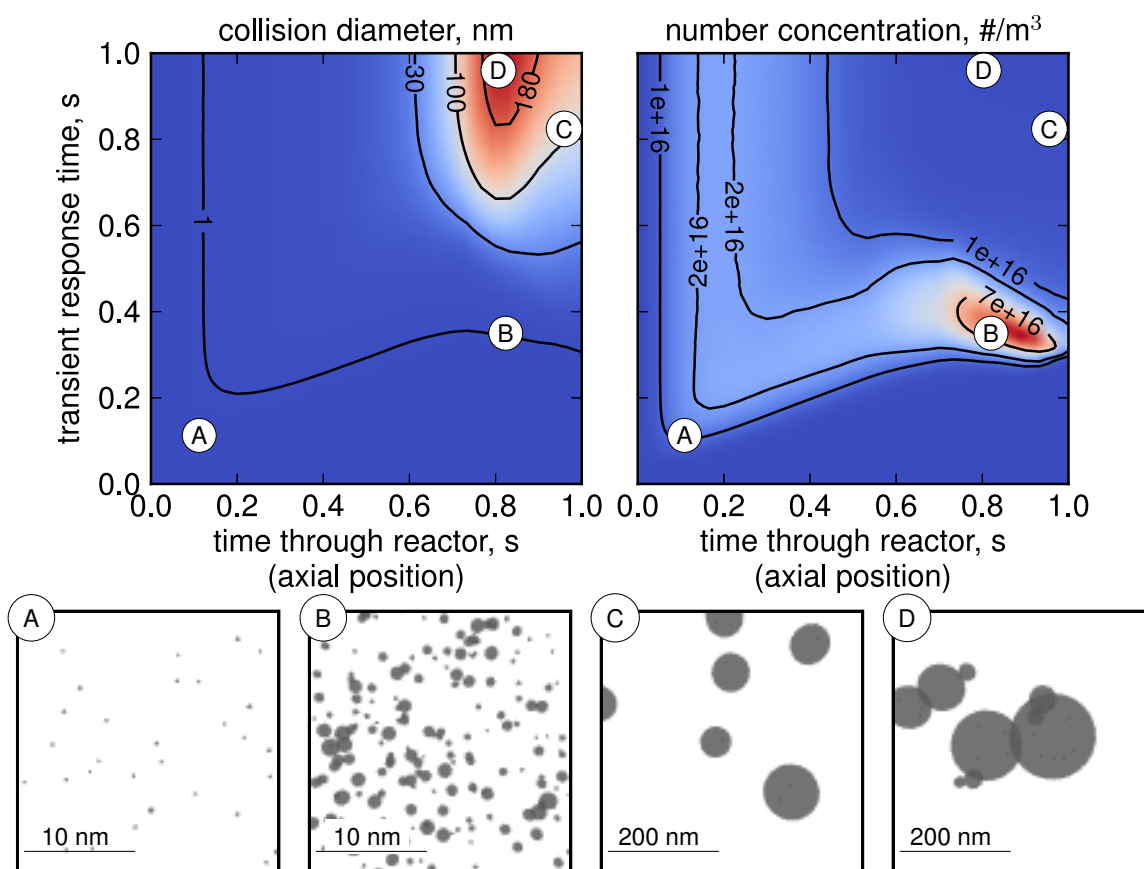


**Figure 7.4:** Contour plots of transient evolution of average collision diameter and particle number concentration. Insets illustrate the particle ensemble state with TEM-style images at the given reactor time (i.e. axial position) and transient response time coordinates, generated using POV-Ray [124].

than the primary polydispersity with PFR solution. In this particular example, the growth by coagulation and sintering under similar timescales [91] causes aggregates of partially-sintered primaries to form, thus depression in the sintering level in both time trajectories is observed.

Information stored in the binary-tree particle model can be used to generate images of sample particle structures. This is illustrated in Figure 7.4, where sample TEM-style images are generated for specific PFR axial position times and transient response times.

The collision diameter (Figure 7.4 left panel) and number concentration (Figure 7.4 right panel) are presented to give representative values of

particle size and quantity as a function of reactor position and transient response time. Panel A represents the initial generation of ‘seed’ particles, which are transported through the network until point B, where the temperature profile causes further rapid nucleation and surface growth. The spike in number concentration at B increases the coagulation rate, causing aggregates to form (Panel D). If particles are transported to the outlet of the reactor, the final temperature increase sinters the particles back to spheres (Panel C).

### 7.3 Conclusions

The case study in Section 7.1 illustrates the issue with parameter fitting in population balance modelling: what if the surface-volume model was used in the place of the binary-tree model for the fitting in Section 6.2? How would the parameters have been different, and would the resultant model have predicted a fundamentally different mechanism of particle formation?

These questions have a wider impact than the particular case of the silicon model analysed here. For example, the sintering parameters typically used in many titania particle models were obtained from model-fitting with the surface-volume type-space [141, 165]. It was not until these empirical expressions were augmented with insight from molecular dynamics (MD) calculations that any reasonable confidence can be held in the sintering parameters [19]. In essence, any fitted parameters should be used with caution until they can be evaluated with another modelling tool.

Further, the study in Section 7.1 highlights an example where experimental insight should be used with caution: if spherical particles are obtained experimentally, it does not necessarily justify the use of a spherical particle model.

The second case study presented an approach for simulating the unsteady-state response of a hot-wall reactor. The transient and axial evolution of the quantities illustrates the power of the methodology developed in this thesis; using a fully-coupled model incorporating gas-phase kinetics and a multi-dimensional particle model enables an unprecedented amount of detail of particle composition, size and structure to be captured.

## Chapter 8

# Conclusions

### 8.1 Findings of this work

The principal motivations of this thesis was to develop new methods and models for simulating silicon nanoparticle synthesis. This was accomplished using stochastic numerical methods to solve population balance models. The methods developed include a new expression for Brownian coagulation, compatible with stochastic weighted algorithms; and an approach to solve networks of linked reactors. Following formulation of a new multivariate model for silicon nanoparticle synthesis, these tools and algorithms were applied to the new silicon model in order to demonstrate how they might be used.

In the first part of this thesis, three existing particle models were compared. The particle properties predicted by these models as a function of coagulation rate and sintering rate were analysed, and different zones corresponding to a particular particle structure were identified. It was found that the models substantially differ from each other where coagulation and sintering occur on similar timescales. This analysis illustrated the importance of using multivariate particle models to accurately capture the size and structure of aggregate particles.

Stochastic methods for solving the population balance equations have only recently been extended to spatially inhomogeneous systems. Stochastic weighted algorithms (SWAs) were proposed in order to control the accumulation of statistical and systematic error in the solution of such systems [119]. The transition regime coagulation kernel was adapted for use with

these methods, allowing for efficient calculation of the coagulation rate using the technique of majorant rates and fictitious jumps. Recognising the importance of multidimensional particle models, the new kernel was tested using a detailed silica particle model. It was found that the new coagulation algorithm, while more computationally expensive than conventional direct simulation, exhibited the superior variance-reduction expected of SWAs.

An algorithm was subsequently presented for solving the population balance equations with the stochastic numerical method for networks of linked reactors. The particle population balance was also fully-coupled with a gas-phase ODE model. The reactor network could represent a mesh of cells in a computational fluid dynamics (CFD) simulation or a 'compartmental model' approximating such a system. The convergence behaviour of the algorithm was tested as a function of network size, degree of feedback and numerical parameters. It was demonstrated that use of SWAs was essential in controlling the accumulation of error, particularly where a large quantity of material was recycled.

A new model for silicon nanoparticle synthesis was then proposed. A systematic parameter estimation procedure was used to determine the pre-exponential factors of five gas-phase chemical reactions and two heterogeneous surface reactions, fitting to a variety of experimental studies over a range of process conditions. The model was tested against six different experimental configurations, with excellent agreement observed for the majority of cases. This new model represents a major step forward in uniting decades of research into silicon nanoparticle formation.

The new silicon model was analysed using the particle formation zones identified in the first part of the thesis. The analysis highlighted that parameters found through an estimation procedure are tied to the particle model with which they were developed, unless they can be confirmed using other sources of data. A reactor networking approach was employed to gain further insight into this silicon system, by studying the transient evolution of a one-dimensional tubular reactor. Here, the particle model was used to visualise the changes in particle concentration, size and structure through the reactor with time.

As stochastic methods are unrivalled in their ability to capture detail of particle structure and morphology, it is anticipated that their use will play a stronger role in process modelling. This thesis has contributed to the

understanding of practical and numerical aspects of such approaches, and provided a new foundation from which the nature of silicon nanoparticle synthesis may be explored.

## 8.2 Suggestions for future work

### **A more detailed particle model?**

The binary-tree particle model adapted to the silicon system in this thesis is currently unrivalled in the amount of detail it can provide about particle internal structure. However, it currently employs a number of assumptions to simplify the calculation of particle properties. For example, a constant fractal dimension is assumed to determine the collision diameter. Alternatively, the fractal dimension could be calculated dynamically from the structural information provided by the particle model. This would yield a more complete description of coagulation.

### **Influence of surface growth**

In Chapter 3, the effect of coagulation and sintering on particle models was assessed. However, it is well-documented that surface-growth can cause rounding of aggregate particles. It could therefore be useful to append a fourth axis representing a characteristic surface-growth rate to Figure 3.3, which could potentially elucidate the suitability of particle models in accounting for surface-rounding. This would require further investigation into the ‘surface smoothing factor’ ( $\sigma_{SR}$ ) for the binary-tree particle model, as its current value is somewhat arbitrary and it is not clear if this parameter can be linked to a physical property of a particle system.

### **Compartmental models**

The reactor networking tools presented in this thesis have many potential applications. One of the most immediate areas for future investigation is for the development of compartmental models. As discussed in Chapter 5 and mentioned above, these models coarsely approximate a CFD grid with linked reactors representing zones of flow. Since the binary-tree particle model is likely to be too computationally expensive to directly couple to CFD calculations, a compartmental model could

be a useful middle-ground for applying a detailed particle model to a system where fluid and particle transport is challenging to model.

### **Silicon colloids**

The model for silicon nanoparticle synthesis was developed on the assumption that silane was the precursor gas. It has, however, been demonstrated that disilane and higher silanes could be used to generate silicon materials, such as the ‘silicon colloids’ of Fenollosa et al. [42]. Confidence in the silicon model’s physical relevance could be further improved if the model was evaluated for these higher silane systems.

### **Silicon and silica models**

It is well-known that silicon will rapidly oxidise in contact with a source of oxygen. Indeed, typical production of silicon nanoparticles can yield particles with a thin oxide layer [75]. The silicon model presented in this thesis could therefore be combined with the multivariate silica particle model of Shekar et al. [144]. With an appropriate kinetic expression to describe the conversion of silicon hydride to silicon dioxide, the two models could be harmonised to provide a more realistic view of industrial manufacture of particles.

## Appendix A

# Appendix to Chapter 3

### A.1 Collision of particles in the near-spherical zone

Suppose two spherical particles with volume  $v_1$  and  $kv_1$  collide. How do the derived properties of the resulting particles differ? The total surface area of the resulting particle is given by:

$$S = \pi \left( \frac{6v_1}{\pi} \right)^{\frac{2}{3}} \left[ 1 + k^{\frac{2}{3}} \right] \quad (\text{A.1.1})$$

The equivalent spherical diameter is given by:

$$d_{\text{sph}} = \left( \frac{6v_1}{\pi} \right)^{\frac{1}{3}} \left[ 1 + k \right]^{\frac{1}{3}} \quad (\text{A.1.2})$$

Thus, the collision diameter as predicted by the surface-volume model may be calculated:

$$d_{\text{col}}^{\text{surf-vol}} = \frac{1}{2} \left( \frac{6v_1}{\pi} \right)^{\frac{1}{3}} \left[ (1 + k)^{\frac{1}{3}} + \sqrt{1 + k^{\frac{2}{3}}} \right] \quad (\text{A.1.3})$$

The binary-tree model requires estimation of the average primary diameter:

$$\overline{d}_{\text{pri}} = \frac{1}{2} \left( \frac{6v_1}{\pi} \right)^{\frac{1}{3}} \left[ 1 + k^{\frac{1}{3}} \right] \quad (\text{A.1.4})$$

Using this information, and calculating the ‘reduced number of primary particles’ (given by the term inside the  $\frac{1}{D_f}$  exponent) the binary-tree model calculates the collision diameter of the aggregate particle as:

$$d_{\text{col}}^{\text{bin-tree}} = \frac{1}{2} \left( \frac{6v_1}{\pi} \right)^{\frac{1}{3}} \left[ 1 + k^{\frac{1}{3}} \right] \left( \frac{\left[ 1 + k^{\frac{2}{3}} \right]^3}{\left[ 1 + k \right]^2} \right)^{\frac{1}{D_f}} \quad (\text{A.1.5})$$

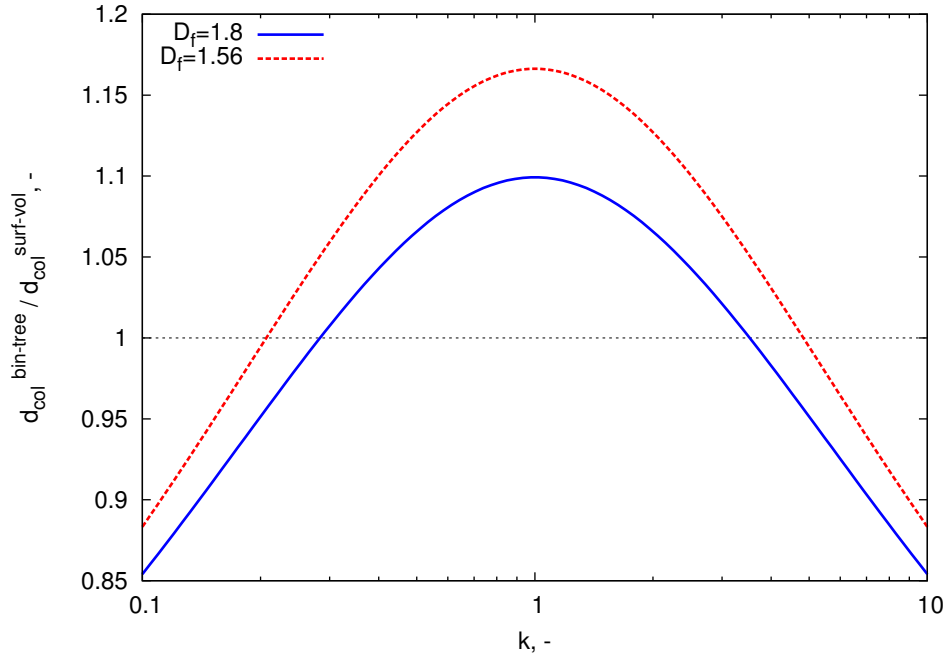


**Figure A.1.1:** Ratio of collision diameters predicted for the surface-volume and binary tree models as a function of relative colliding particle size.

The two models are compared by plotting the ratio of  $d_{\text{col}}^{\text{bin-tree}}$  to  $d_{\text{col}}^{\text{surf-vol}}$  using a fractal dimension  $D_f = 1.8$  and  $D_f = 1.56$ . It is evident that for like-sized particles ( $k \approx 1$ ) the collision diameter as predicted by the surface-volume model will be smaller than that predicted by the binary-tree particle model to a maximum of 10% under-estimation.

## A.2 Comparison of maximum sinterable surface area

Now suppose that a particle  $P_q$  consists of  $n$  equally-sized primary particles of volume  $v_1$ . The equivalent spherical surface area is given by:

$$S_{\text{sph}} = \pi \left( \frac{6nv_1}{\pi} \right)^{\frac{2}{3}} \quad (\text{A.2.1})$$

The initial surface area of such a particle as calculated by the surface-volume model is the sum of the surface area of each of the primaries:

$$S^{\text{surf-vol}} = n\pi \left( \frac{6v_1}{\pi} \right)^{\frac{2}{3}} \quad (\text{A.2.2})$$

In the binary-tree model, there are  $n-1$  connections between particles, each of these with a surface area given by the sum of the surface area of the two touching primaries. The total surface area considered by the binary tree model is therefore given by:

$$S^{\text{bin-tree}} = 2(n-1)\pi \left( \frac{6v_1}{\pi} \right)^{\frac{2}{3}} \quad (\text{A.2.3})$$

If sintering occurs with the same characteristic time  $\tau_S$ , the relative rates of sintering can be compared between models by comparing the difference between the initial and spherical surface area, termed the maximum sinterable surface area:

$$\Delta S = S - S_{\text{sph}} \quad (\text{A.2.4})$$

To compare these between the binary tree and surface-volume models, the ratio of the maximum sinterable surface area ( $r$ ) for between models is used:

$$r = \frac{\Delta S^{\text{bin-tree}}}{\Delta S^{\text{surf-vol}}} = \frac{2(n-1) - n^{2/3}}{n - n^{2/3}} \quad (\text{A.2.5})$$

For  $n \geq 2$ ,  $r \geq 1.0$  and as such, more sinterable surface area exists in the binary tree model, as compared to the surface-volume model.

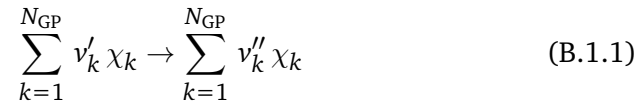
## Appendix B

# Appendix to Chapter 6

### B.1 Conversion of *SURFACE CHEMKIN* parameters

*SURFACE CHEMKIN* was developed by Coltrin et al. [30] to model the complex surface chemistry in chemical vapour deposition processes. It consists of a set of packages to interpret general heterogeneous chemical mechanisms in a standardised manner. As the gas-surface mechanism proposed by Houf et al. [64] and Ho et al. [63] was formulated in terms of a *SURFACE CHEMKIN* mechanism, the form of the rate expression requires ‘conversion’ so that is compatible with the type-space of the present work’s model.

In a similar vein to Equation (2.1) An irreversible heterogeneous reaction may be represented in the general form [30]:



Assuming only a single irreversible heterogeneous reaction is present, the rate of progress variable  $q$  (in mol/cm<sup>2</sup>s) is given by:

$$q = k_f \prod_{k=1}^{N_{\text{GP}}} c_{\chi_k}^{\nu'_k} \quad (\text{B.1.2})$$

where  $c_{\chi_k}$  is the gas-phase (mol/cm<sup>3</sup>) or surface (mol/cm<sup>2</sup>) concentration of species  $k$ . The forward rate constant  $k_f$  adopts a standard Arrhenius form:

$$k_f = A^* \exp\left(-\frac{E_A}{RT}\right) \quad (\text{B.1.3})$$

**Table B.1:** Surface reaction mechanism for silanes proposed by Ho et al. [63]. The (S) and (B) subscripts refer to surface and bulk species, respectively.

Reaction	$A^*$ cm <sup>5</sup> /mol <sup>2</sup> s	$E_A$ kcal/mol
$\text{SiH}_4 + 2\text{Si}_{(\text{S})} \rightarrow 2\text{SiH}_{(\text{S})} + \text{Si}_{(\text{B})} + \text{H}_2$	$8.39 \times 10^{26}$	37.45
$\text{Si}_2\text{H}_6 + 2\text{Si}_{(\text{S})} \rightarrow 2\text{SiH}_{(\text{S})} + 2\text{Si}_{(\text{B})} + 2\text{H}_2$	$8.39 \times 10^{27}$	37.45
$\text{Si}_3\text{H}_8 + 2\text{Si}_{(\text{S})} \rightarrow 2\text{SiH}_{(\text{S})} + 3\text{Si}_{(\text{B})} + 3\text{H}_2$	$8.39 \times 10^{27}$	37.45

To adapt the mechanisms for silane surface reactions [63, 64] to the present work, Equations B.1.1–B.1.3 must be applied to the chemical reactions given in Table B.1.

As an example, this will be done for  $\text{SiH}_4$ . Using Equation B.1.1, we observe that the forward rate coefficients are  $v'_{\text{SiH}_4} = 1$  and  $v'_{\text{Si}_{(\text{S})}} = 2$ . Thus, the rate of progress  $q$  for this reaction is given by:

$$q = A^* c_{\text{SiH}_4}^1 c_{\text{Si}_{(\text{S})}}^2 \exp\left(-\frac{E_A}{RT}\right) \quad (\text{B.1.4})$$

Writing Equation B.1.4 in this form enables deduction of the units of  $A^*$ . Here, they must be cm<sup>5</sup>/mol<sup>2</sup>s in order to ensure dimensional consistency. Assuming that the concentration of surface  $\text{Si}_{(\text{S})}$  sites—given by  $\lambda_{\text{Si}}$  (#/cm<sup>2</sup>)—is constant, we write:

$$\lambda_{\text{Si}} = N_A c_{\text{Si}_{(\text{S})}} \quad (\text{B.1.5})$$

To ‘translate’ Equation B.1.4 to the type-space of the present work, we must ensure that the surface reaction rate  $R_{\text{SR}}$  is dimensionally consistent with the other rates:

$$R_{\text{SR}} = S N_A q \quad (\text{B.1.6})$$

Substituting in for  $\lambda_{\text{Si}}$  and rearranging yields:

$$R_{\text{SR}} = A c_{\text{SiH}_4} S \left(-\frac{E_A}{RT}\right) \quad (\text{B.1.7})$$

where  $A$  is the alternative pre-exponential factor used in the present work, given by:

$$A = \frac{A^* \lambda_{\text{Si}}^2}{N_A} \quad (\text{B.1.8})$$

**Table B.2:** Estimation of  $A_{\text{SR,SiH}_4}$  based on different site densities.

Parameter	Lower bound	This work	Upper bound
$\lambda_{\text{Si}}$ ( $\#/ \text{cm}^2$ )	$8.0 \times 10^{14}$ [140]	-	$1.7 \times 10^{15}$
$A_{\text{SR,SiH}_4}$ (cm/mol.s)	$8.9 \times 10^{32}$	$3.0 \times 10^{33}$	$4.0 \times 10^{33}$

By estimating the site density  $\lambda_{\text{Si}}$ , it is possible to convert the value of the pre-exponential factor  $A^*$  into the  $A$  used in present work. An upper-bound on  $\lambda_{\text{Si}}$  can be estimated by using the bulk density of silicon. A lower bound on  $\lambda_{\text{Si}}$  is taken for the {111} surface of silicon at full saturation [140].

We observe that Equation B.1.7 is the same as that used by Menz et al. [92]; and that the parameters for silane in Table B.2 shows good agreement with their pre-exponential factors calculated via optimisation ( $A_{\text{SR,SiH}_4} = 3.0 \times 10^{33}$ ) in the present work.

# Nomenclature

## Upper-case Roman

$A$	Arrhenius pre-exponential factor
$C$	Connectivity matrix
$Da$	Damköhler number
$D_f$	Fractal dimension
$E_A$	Activation energy
$F_C$	Ratio of downstream to upstream scaling factors
$F_V$	Volume fraction of particles
$F_S$	Outflow rescaling factor
$G$	Gas-phase state-space
$\hat{H}$	Specific molar enthalpy
$K$	Coagulation kernel
$K_C$	Chemical equilibrium constant
$K^{\text{fm}}$	Free-molecular coagulation kernel
$K^{\text{sf}}$	Slip-flow coagulation kernel
$K^{\text{tr}}$	Transition regime coagulation kernel
$Kn$	Knudsen number
$L$	Number of independent runs
$M$	Third-body collision species symbol
$M_i(t)$	Moment $i$ of the particle ensemble
$N_A$	Avogadro's number
$N_{\text{GP}}$	Number of gas-phase chemical species
$N_h$	Number of factorised terms in majorant kernel
$N_{\text{rxn}}$	Number of gas-phase chemical reactions

$N_{\max}$	Maximum number of computational particles
$N(t)$	Number of computational particles at time $t$
$P$	Computational particle type
$P$	Pressure
$P_r$	Reduced pressure
$Q$	Volumetric flowrate
$R$	Ideal gas constant
$R_i$	Rate of particle process $i$
$S$	Surface area
$S_{\text{Si}}$	Supersaturation of silicon
$S_{\text{sph}}$	Equivalent spherical surface area
$T$	Temperature (in Kelvin)
$V$	Volume
$V_{\text{smp}}$	Sample volume for stochastic particle method
$X(t)$	Functional describing some particle ensemble property
$Z$	Particle state-space

### Lower-case Roman

$c$	Molar concentration of chemical species
$d_{\text{col}}$	Particle collision diameter
$d_{\text{mob}}$	Particle mobility diameter
$d_{\text{pri}}$	Primary particle diameter
$f$	Fractional inflow
$\dot{g}$	Molar production rate due to particle processes
$h_i^{(j)}$	Upper bound for majorant kernel
$m$	Mass of particle
$n$	Number of primary particles
$n(t, P)$	Number concentration of particles
$k$	Chemical rate coefficient
$k_0$	Low-pressure limit rate coefficient
$k_\infty$	High-pressure limit rate coefficient
$k_B$	Boltzmann constant

$k_{\text{maj}}$	Majorant constant
$t$	Time
$p$	Primary particle
$p_{\text{Si}}$	Partial pressure of silicon
$p_{\text{Si,sat}}$	Saturation vapour pressure of silicon
$q$	Chemical rate of progress variable
$s$	Sintering level
$v$	Primary particle volume
$w$	Statistical weight
$\mathbf{x}$	Parameter vector
$y$	Mole fraction

### Upper-case Greek

$\Phi$	Objective function
--------	--------------------

### Lower-case Greek

$\alpha$	Free-molecular coagulation parameter
$\beta$	Arrhenius temperature exponent
$\beta_1, \beta_2$	Slip-flow coagulation parameters
$\gamma(P_i, w_i, P_j, w_j)$	Weight transfer function [122]
$\gamma_{\text{si}}$	Surface energy of silicon
$\delta v$	Change in volume due to surface reaction
$\epsilon$	Relative numerical error
$\epsilon_{\text{stat}}$	Relative numerical error due to statistical fluctuations
$\eta_i$	Number of chemical units of species $i$
$\theta$	Molar coverage of species on surface
$\lambda$	Partial sum in particle binary tree
$\mu(\mathbf{X})(t)$	Average quantity of functional $X(t)$ over number of particles
$\nu$	Stoichiometric coefficient
$\xi$	Average quantity (over runs)
$\rho$	Density (mass or molar)

$\sigma$	Mean free path
$\sigma_{\text{SR}}$	Surface smoothing factor
$\zeta(P)$	Function representing sintering
$\tau$	Residence or characteristic time
$\phi$	Data point for fitting in objective function
$\chi$	Chemical symbol
$\psi$	Gas-phase expansion rate
$\dot{\omega}$	Molar production rate due to gas-phase reactions

### Superscripts

$(q)$	Particle property index
$[j]$	Stream index

### Subscripts

a	Arithmetic
g	Geometric
S	Denotes sintering property
SR	Denotes property of a surface reaction

### Abbreviations

CFD	Computational fluid dynamics
CSTR	Continuous-stirred tank reactor
DSA	Direct simulation algorithm
MD	Molecular dynamics
ODE	Ordinary differential equation
PFR	Plug-flow reactor
PSD	Particle size distribution
PSR	Perfectly-stirred reactor
SWA	Stochastic weighted algorithm

# Bibliography

- [1] A. J. Adamczyk, M. F. Reyniers, G. B. Marin, and L. J. Broadbelt. Exploring 1, 2-hydrogen shift in silicon nanoparticles: Reaction kinetics from quantum chemical calculations and derivation of transition state group additivity database. *The Journal of Physical Chemistry A*, 113(41):10933–10946, 2009.
- [2] M. K. Akhtar, Y. Xiong, and S. E. Pratsinis. Vapor synthesis of titania powder by titanium tetrachloride oxidation. *AIChE Journal*, 37(10):1561–1570, 1991.
- [3] J. Akroyd, A. J. Smith, L. R. McGlashan, and M. Kraft. Numerical investigation of DQMoM-IEM as a turbulent reaction closure. *Chemical Engineering Science*, 65(6):1915–1924, 2010.
- [4] J. Akroyd, A. J. Smith, R. Shirley, L. R. McGlashan, and M. Kraft. A coupled CFD-population balance approach for nanoparticle synthesis in turbulent reacting flows. *Chemical Engineering Science*, 66(17):3792–3805, 2011.
- [5] A. H. Alexopoulos, P. Pladis, and C. Kiparissides. Nonhomogeneous mixing population balance model for the prediction of particle size distribution in large scale emulsion polymerization reactors. *Industrial & Engineering Chemistry Research*, 52:12285–12296, 2013.
- [6] ANSYS, Inc. ANSYS FLUENT 12. 0 User’s Guide, 2009.
- [7] H. Antoniadis. Silicon ink high efficiency solar cells. In *Photovoltaic Specialists Conference (PVSC), 2009 34th IEEE*, pages 650–654, 2009.
- [8] M. Balthasar and M. Kraft. A stochastic approach to calculate the particle size distribution function of soot particles in laminar premixed flames. *Combustion and Flame*, 133(3):289–298, 2003.

- [9] J. F. Banfield and H. Zhang. Nanoparticles in the environment. *Reviews in Mineralogy and Geochemistry*, 44(1):1–58, 2001.
- [10] S. K. Bermingham, P. J. T. Verheijen, and H. J. M. Kramer. Optimal design of solution crystallization processes with rigorous models. *Chemical Engineering Research and Design*, 81(8):893–903, 2003.
- [11] F. Bezzo and S. Macchietto. A general methodology for hybrid multi-zonal/CFD models: Part II. Automatic zoning. *Computers & Chemical Engineering*, 28(4):513–525, 2004.
- [12] F. Bezzo, S. Macchietto, and C. C. Pantelides. A general methodology for hybrid multi-zonal/CFD models: Part I. Theoretical framework. *Computers & Chemical Engineering*, 28(4):501–511, 2004.
- [13] A. Bhave and M. Kraft. Partially stirred reactor model: Analytical solutions and numerical convergence study of a PDF/Monte Carlo method. *SIAM Journal on Scientific Computing*, 25(5):1798–1823, 2004.
- [14] G. Biskos, V. Vons, C. U. Yurteri, and A. Schmidt-Ott. Generation and sizing of particles for aerosol-based nanotechnology. *KONA Powder Particle J*, 26:13–35, 2008.
- [15] G. Blanquart and H. Pitsch. Analyzing the effects of temperature on soot formation with a joint volume-surface-hydrogen model. *Combustion and Flame*, 156(8):1614–1626, 2009.
- [16] M. Bowrey and J. H. Purnell. The pyrolysis of disilane and rate constants of silene insertion reactions. *Proceedings of the Royal Society of London A*, 321(1546):341–359, 1971.
- [17] A. Braumann, P. L. W. Man, and M. Kraft. The inverse problem in granulation modeling—Two different statistical approaches. *AIChE Journal*, 57(11):3105–3121, 2011.
- [18] V. S. Buddhiraju and V. Runkana. Simulation of nanoparticle synthesis in an aerosol flame reactor using a coupled flame dynamics—monodisperse population balance model. *Journal of Aerosol Science*, 43(1):1–13, 2012.

- [19] B. Buesser, A. J. Gröhn, and SE Pratsinis. Sintering rate and mechanism of TiO<sub>2</sub> nanoparticles by molecular dynamics. *The Journal of Physical Chemistry C*, 115(22):11030–11035, 2011.
- [20] A. Burcat. Thermochemical data for combustion calculations. In *Combustion Chemistry*, pages 455–473. Springer, 1984.
- [21] R. J. Buss, P. Ho, W. G. Breiland, and M. E. Coltrin. Reactive sticking coefficients for silane and disilane on polycrystalline silicon. *Journal of Applied Physics*, 63(8):2808–2819, 1988.
- [22] W. R. Cannon, S. C. Danforth, J. H. Flint, J. S. Haggerty, and R. A. Marra. Sinterable ceramic powders from laser-driven reactions: I, Process description and modeling. *Journal of the American Ceramic Society*, 65(7):324–330, 1982.
- [23] W. R. Cannon, S. C. Danforth, J. S. Haggerty, and R. A. Marra. Sinterable ceramic powders from laser-driven reactions: II, Powder characteristics and process variables. *Journal of the American Ceramic Society*, 65(7):330–335, 1982.
- [24] Cantera Developers. Cantera: An object-oriented software toolkit for chemical kinetics, thermodynamics, and transport processes, 2013. URL <http://code.google.com/p/cantera>.
- [25] M. Celnik, R.I.A. Patterson, M. Kraft, and W. Wagner. Coupling a stochastic soot population balance to gas-phase chemistry using operator splitting. *Combustion and Flame*, 148(3):158–176, 2007.
- [26] M. Celnik, R.I.A. Patterson, M. Kraft, and W. Wagner. A predictor-corrector algorithm for the coupling of stiff ODEs to a particle population balance. *Journal of Computational Physics*, 228(8):2758–2769, 2009.
- [27] D. Chen, Z. Zainuddin, E. Yapp, J. Akroyd, S. Mosbach, and M. Kraft. A fully coupled simulation of PAH and soot growth with a population balance model. *Proceedings of the Combustion Institute*, 34:1827–1835, 2013.
- [28] Z. Chen, H. Meng, G. Xing, H. Yuan, F. Zhao, R. Liu, X. Chang, X. Gao, T. Wang, and G. Jia. Age-related differences in pulmonary and car-

- diovascular responses to SiO<sub>2</sub> nanoparticle inhalation: nanotoxicity has susceptible population. *Environmental Science & Technology*, 42(23):8985–8992, 2008.
- [29] K.-Y. Cheng, R. Anthony, U. R. Kortshagen, and R. J. Holmes. Hybrid silicon nanocrystal-organic light-emitting devices for infrared electroluminescence. *Nano Letters*, 10(4):1154–1157, 2010.
- [30] M. E. Coltrin, R. J. Kee, F. M. Rupley, and E. Meeks. SURFACE CHEMKIN III: A Fortran Package for Analyzing Heterogeneous Chemical Kinetics at a Solid-Surface-Gas-Phase Interface. *Sandia National Laboratories*, 1996.
- [31] H. Dang and M. T. Swihart. Computational modeling of silicon nanoparticle synthesis: I. A general two-dimensional model. *Aerosol Science and Technology*, 43(3):250–263, 2009.
- [32] H. Dang and M. T. Swihart. Computational modeling of silicon nanoparticle synthesis: II. A two-dimensional bivariate model for silicon nanoparticle synthesis in a laser-driven reactor including finite-rate coalescence. *Aerosol Science and Technology*, 43(6):554–569, 2009.
- [33] E. Debry, B. Sportisse, and B. Jourdain. A stochastic approach for the numerical simulation of the general dynamics equation for aerosols. *Journal of Computational Physics*, 184(2):649–669, 2003.
- [34] R. E. L. DeVille, N. Riemer, and M. West. Weighted Flow Algorithms (WFA) for stochastic particle coagulation. *Journal of Computational Physics*, 230:8427–8451, 2011.
- [35] K. E. Drexler. *Engines of Creation*. Fourth Estate, 1986.
- [36] M. L. Eggersdorfer, D. Kadau, H. J. Herrmann, and S. E. Pratsinis. Aggregate morphology evolution by sintering: Number & diameter of primary particles. *Journal of Aerosol Science*, 46:7–19, 2012.
- [37] A. Eibeck and W. Wagner. An efficient stochastic algorithm for studying coagulation dynamics and gelation phenomena. *SIAM Journal on Scientific Computing*, 22(3):802–821, 2001.

- [38] A. Eibeck and W. Wagner. Stochastic particle approximations for Smoluchowski's coagulation equation. *Annals of Applied Probability*, pages 1137–1165, 2001.
- [39] D. Erhardt. Materials conservation: Not-so-new technology. *Nature Materials*, 2(8):509–510, 2003.
- [40] F. Erogbogbo, K.-T. Yong, I. Roy, G. Xu, P. N. Prasad, and M. T. Swihart. Biocompatible luminescent silicon quantum dots for imaging of cancer cells. *ACS Nano*, 2(5):873–878, 2008.
- [41] F. C. Eversteijn. Gas-phase decomposition of silane in a horizontal epitaxial reactor. *Philips Res. Repts*, 26(2):134–144, 1971.
- [42] R. Fenollosa, F. Ramiro-Manzano, M. Tymczenko, and F. Meseguer. Porous silicon microspheres: synthesis, characterization and application to photonic microcavities. *Journal of Materials Chemistry*, 20(25):5210–5214, 2010.
- [43] T. Finsterbusch and A. Mankertz. Porcine circoviruses—small but powerful. *Virus Research*, 143(2):177–183, 2009.
- [44] J. H. Flint and J. S. Haggerty. A model for the growth of silicon particles from laser-heated gases. *Aerosol Science and Technology*, 13(1):72–84, 1990.
- [45] J. H. Flint, R. A. Marra, and J. S. Haggerty. Powder temperature, size, and number density in laser-driven reactions. *Aerosol Science and Technology*, 5(2):249–260, 1986.
- [46] H. S. Fogler. *Elements of Chemical Reaction Engineering*. Pearson, New Jersey, 2006.
- [47] M. Frenklach. Method of moments with interpolative closure. *Chemical Engineering Science*, 57(12):2229–2239, 2002.
- [48] M. Frenklach and S. J. Harris. Aerosol dynamics modeling using the method of moments. *Journal of Colloid and Interface Science*, 118(1):252–261, 1987.
- [49] M. Frenklach, L. Ting, H. Wang, and M. J. Rabinowitz. Silicon particle formation in pyrolysis of silane and disilane. *Israel Journal of Chemistry*, 36(3):293–303, 1996.

- [50] A. Gallagher, A. A. Howling, and C. H. Hollenstein. Anion reactions in silane plasma. *Journal of Applied Physics*, 91(9):5571–5580, 2002.
- [51] B. Giesen, H. Wiggers, A. Kowalik, and P. Roth. Formation of Si-nanoparticles in a microwave reactor: Comparison between experiments and modelling. *Journal of Nanoparticle Research*, 7(1):29–41, 2005.
- [52] C. J. Giunta, R. J. McCurdy, J. D. Chapple-Sokol, and R. G. Gordon. Gas-phase kinetics in the atmospheric pressure chemical vapor deposition of silicon from silane and disilane. *Journal of Applied Physics*, 67(2):1062–1075, 1990.
- [53] M. Goodson and M. Kraft. An efficient stochastic algorithm for simulating nano-particle dynamics. *Journal of Computational Physics*, 183(1):210–232, 2002.
- [54] M. Goodson and M. Kraft. Simulation of coalescence and breakage: an assessment of two stochastic methods suitable for simulating liquid-liquid extraction. *Chemical Engineering Science*, 59(18):3865–3881, 2004.
- [55] D. E. Gray, editor. *American Institute of Physics Handbook*. McGraw-Hill, New York, 1972.
- [56] M. Gröschel, R. Körmer, M. Walther, G. Leugering, and W. Peukert. Process control strategies for the gas phase synthesis of silicon nanoparticles. *Chemical Engineering Science*, 73:181–194, 2012.
- [57] F. Guiaş. A stochastic numerical method for diffusion equations and applications to spatially inhomogeneous coagulation processes. In *Monte Carlo and Quasi-Monte Carlo Methods 2004*, pages 147–161. Springer, 2006.
- [58] A. Gupta and H. Wiggers. Surface chemistry and photoluminescence property of functionalized silicon nanoparticles. *Physica E*, 41(6):1010–1014, 2009.
- [59] Z. Haibo, Z. Chuguang, and X. Minghou. Multi-Monte Carlo approach for general dynamic equation considering simultaneous parti-

- cle coagulation and breakage. *Powder Technology*, 154(2-3):164–178, 2005.
- [60] S. J. Harris and I. M. Kennedy. The coagulation of soot particles with van der waals forces. *Combustion Science and Technology*, 59(4-6): 443–454, 1988.
- [61] M. C. Heine and S. E. Pratsinis. Polydispersity of primary particles in agglomerates made by coagulation and sintering. *Journal of Aerosol Science*, 38(1):17–38, 2007.
- [62] T. Hirokami, Y. Maeda, and H. Tsukada. Parameter estimation using simultaneous perturbation stochastic approximation. *Electrical Engineering in Japan*, 154:30–39, 2006.
- [63] P. Ho, M. E. Coltrin, and W. G. Breiland. Laser-induced fluorescence measurements and kinetic analysis of Si atom formation in a rotating disk chemical vapor deposition reactor. *The Journal of Physical Chemistry*, 98(40):10138–10147, 1994.
- [64] W. G. Houf, J. F. Grear, and W. G. Breiland. A model for low pressure chemical vapor deposition in a hot-wall tubular reactor. *Materials Science and Engineering: B*, 17(1-3):163–171, 1993.
- [65] M. J. Hounslow. A discretized population balance for continuous systems at steady state. *AIChE Journal*, 36(1):106–116, 1990.
- [66] A. A. Howling, J. L. Dorier, C. H. Hollenstein, U. Kroll, and F. Finger. Frequency effects in silane plasmas for plasma enhanced chemical vapor deposition. *Journal of Vacuum Science & Technology A*, 10(4): 1080–1085, 1992.
- [67] R. Irizarry. Fast compartmental monte carlo simulation of population balance models: Application to nanoparticle formation in nonhomogeneous conditions. *Industrial & Engineering Chemistry Research*, 51(47):15484–15496, 2012.
- [68] T. Johannessen, S. E. Pratsinis, and H. Livbjerg. Computational fluid-particle dynamics for the flame synthesis of alumina particles. *Chemical Engineering Science*, 55(1):177–191, 2000.

- [69] K. C. Kannenberg and I. D. Boyd. Strategies for efficient particle resolution in the direct simulation monte carlo method. *Journal of Computational Physics*, 157(2):727–745, 2000.
- [70] A. Kazakov and M. Frenklach. Dynamic modeling of soot particle coagulation and aggregation: Implementation with the method of moments and application to high-pressure laminar premixed flames. *Combustion and Flame*, 114(3):484–501, 1998.
- [71] Robert J Kee, Fran M Rupley, Ellen Meeks, and James A Miller. *CHEMKIN-III: A FORTRAN chemical kinetics package for the analysis of gas-phase chemical and plasma kinetics*. Sandia National Laboratories, 1996.
- [72] J. Knipping, H. Wiggers, B. Rellinghaus, P. Roth, D. Konjhodzic, and C. Meier. Synthesis of high purity silicon nanoparticles in a low pressure microwave reactor. *Journal of Nanoscience and Nanotechnology*, 4(8):1039–1044, 2004.
- [73] W. Koch and SK Friedlander. The effect of particle coalescence on the surface area of a coagulating aerosol. *Journal of Colloid and Interface Science*, 140(2):419–427, 1990.
- [74] A. Kolodko and K. Sabelfeld. Stochastic particle methods for Smoluchowski coagulation equation: variance reduction and error estimations. *Monte Carlo Methods Applied*, 9(4):315–339, 2003.
- [75] R. Körmer, M. P. M. Jank, H. Ryssel, H. J. Schmid, and W. Peukert. Aerosol synthesis of silicon nanoparticles with narrow size distribution—Part 1: Experimental investigations. *Journal of Aerosol Science*, 41(11):998–1007, 2010.
- [76] R. Körmer, H. J. Schmid, and W. Peukert. Aerosol synthesis of silicon nanoparticles with narrow size distribution—Part 2: Theoretical analysis of the formation mechanism. *Journal of Aerosol Science*, 41(11):1008–1019, 2010.
- [77] M. Koshi, S. Kato, and H. Matsui. Unimolecular decomposition of silane, fluorosilane, and difluorosilane at high temperatures. *The Journal of Physical Chemistry*, 95(3):1223–1227, 1991.

- [78] F. E. Kruis, K. Kusters, S. E. Pratsinis, and B. Scarlett. A simple model for the evolution of the characteristics of aggregate particles undergoing coagulation and sintering. *Aerosol Science and Technology*, 19: 514–526, 1993.
- [79] F. E. Kruis, J. Schoonman, and B. Scarlett. Homogeneous nucleation of silicon. *Journal of Aerosol Science*, 25(7):1291–1304, 1994.
- [80] F. E. Kruis, H. Fissan, and A. Peled. Synthesis of nanoparticles in the gas phase for electronic, optical and magnetic applications—a review. *Journal of Aerosol Science*, 29(5):511–535, 1998.
- [81] F. E. Kruis, A. Maisels, and H. Fissan. Direct simulation Monte Carlo method for particle coagulation and aggregation. *AIChE Journal*, 46 (9):1735–1742, 2000.
- [82] F. E. Kruis, J. Wei, T. van der Zwaag, and S. Haep. Computational fluid dynamics based stochastic aerosol modeling: Combination of a cell-based weighted random walk method and a constant-number Monte-Carlo method for aerosol dynamics. *Chemical Engineering Science*, 70:109–120, 2012.
- [83] P. Lavvas, M. Sander, M. Kraft, and H. Imanaka. Surface chemistry and particle shape: Processes for the evolution of aerosols in titan’s atmosphere. *The Astrophysical Journal*, 728(2):80, 2011.
- [84] J. Li, B. Freireich, C. Wassgren, and J. D. Litster. A general compartment-based population balance model for particle coating and layered granulation. *AIChE Journal*, 58(5):1397–1408, 2012.
- [85] X. Li, Y. He, and M. T. Swihart. Surface functionalization of silicon nanoparticles produced by laser-driven pyrolysis of silane followed by HF-HNO<sub>3</sub> etching. *Langmuir*, 20(11):4720–4727, 2004.
- [86] Z. F. Li and E. Ruckenstein. Water-soluble poly (acrylic acid) grafted luminescent silicon nanoparticles and their use as fluorescent biological staining labels. *Nano Letters*, 4(8):1463–1467, 2004.
- [87] F. A. Lindemann, S. Arrhenius, I. Langmuir, N. R. Dhar, J. Perrin, and W. C. McC. Lewis. Discussion on “the radiation theory of chemical action”. *Transactions of the Faraday Society*, 17:598–606, 1922.

- [88] L. Mangolini. Synthesis, properties, and applications of silicon nanocrystals. *Journal of Vacuum Science & Technology B*, 31(2): 020801, 2013.
- [89] D. L. Marchisio and R. O. Fox. Solution of population balance equations using the direct quadrature method of moments. *Journal of Aerosol Science*, 36(1):43–73, 2005.
- [90] W. J. Menz and M. Kraft. A new model for silicon nanoparticle synthesis. *Combustion and Flame*, 160:947–958, 2013.
- [91] W. J. Menz and M. Kraft. The suitability of particle models in capturing aggregate structure and polydispersity. *Aerosol Science & Technology*, 47:734–745, 2013.
- [92] W. J. Menz, S. Shekar, G. Brownbridge, S. Mosbach, R. Körmer, W. Peukert, and M. Kraft. Synthesis of silicon nanoparticles with a narrow size distribution: A theoretical study. *Journal of Aerosol Science*, 44:46–61, 2012.
- [93] W. J. Menz, R. I. A. Patterson, W. Wagner, and M. Kraft. Application of stochastic weighted algorithms to a multidimensional silica particle model. *Journal of Computational Physics*, 248:221–234, 2013.
- [94] W. J. Menz, J. Akroyd, and M. Kraft. Stochastic solution of population balance equations for reactor networks. *Journal of Computational Physics*, 256:615–629, 2014.
- [95] M. Meunier, J. H. Flint, J. S. Haggerty, and D. Adler. Laser-induced chemical vapor deposition of hydrogenated amorphous silicon. I. Gas-phase process model. *Journal of Applied Physics*, 62(7):2812–2821, 1987.
- [96] M. Meunier, J. H. Flint, J. S. Haggerty, and D. Adler. Laser-induced chemical vapor deposition of hydrogenated amorphous silicon. II. Film properties. *Journal of Applied Physics*, 62(7):2821–2829, 1987.
- [97] X. Michalet, F. F. Pinaud, L. A. Bentolila, J. M. Tsay, S. Doose, J. J. Li, G. Sundaresan, A. M. Wu, S. S. Gambhir, and S. Weiss. Quantum dots for live cells, in vivo imaging, and diagnostics. *Science*, 307(5709): 538–544, 2005.

- [98] N. M. Morgan, C. G. Wells, M. Kraft, and W. Wagner. Modelling nanoparticle dynamics: coagulation, sintering, particle inception and surface growth. *Combustion Theory and Modelling*, 9(3):449–461, 2005.
- [99] N. M. Morgan, C. G. Wells, M. J. Goodson, M. Kraft, and W. Wagner. A new numerical approach for the simulation of the growth of inorganic nanoparticles. *Journal of Computational Physics*, 211(2): 638–658, 2006.
- [100] S. Mosbach, A. Braumann, P. L. W. Man, C. A. Kastner, G. P. E. Brownbridge, and M. Kraft. Iterative improvement of bayesian parameter estimates for an engine model by means of experimental design. *Combustion and Flame*, 159(3):1303–1313, 2012.
- [101] T. Murthy, N. Miyamoto, M. Shimbo, and J. Nishizawa. Gas-phase nucleation during the thermal decomposition of silane in hydrogen. *Journal of Crystal Growth*, 33(1):1–7, 1976.
- [102] O. M. Nayfeh, D. A. Antoniadis, K. Mantey, and M. H. Nayfeh. Memory effects in metal-oxide-semiconductor capacitors incorporating dispensed highly monodisperse 1 nm silicon nanoparticles. *Applied Physics Letters*, 90(15):153105–153105, 2007.
- [103] H. V. Nguyen and R. C. Flagan. Particle formation and growth in single-stage aerosol reactors. *Langmuir*, 7(8):1807–1814, 1991.
- [104] S. Nijhawan, P. H. McMurry, M. T. Swihart, S. M. Suh, S. L. Girshick, S. A. Campbell, and J. E. Brockmann. An experimental and numerical study of particle nucleation and growth during low-pressure thermal decomposition of silane. *Journal of Aerosol Science*, 34(6):691–711, 2003.
- [105] B. Nowack and T. D. Bucheli. Occurrence, behavior and effects of nanoparticles in the environment. *Environmental Pollution*, 150(1): 5–22, 2007.
- [106] T. R. Nurkiewicz, D. W. Porter, A. F. Hubbs, J. L. Cumpston, B. T. Chen, D. G. Frazer, and V. Castranova. Nanoparticle inhalation augments particle-dependent systemic microvascular dysfunction. *Particle and Fibre Toxicology*, 5(1), 2008.

- [107] J. O. Odden, P. K. Egeberg, and A. Kjekshus. From monosilane to crystalline silicon, Part I: Decomposition of monosilane at 690–830 K and initial pressures 0.1–6.6 MPa in a free-space reactor. *Solar Energy Materials and Solar Cells*, 86(2):165–176, 2005.
- [108] J. O. Odden, P. K. Egeberg, and A. Kjekshus. From monosilane to crystalline silicon, Part III. Characterization of amorphous, hydrogen-containing silicon products. *Journal of Non-Crystalline Solids*, 351(14):1317–1327, 2005.
- [109] J. O. Odden, P. K. Egeberg, and A. Kjekshus. From monosilane to crystalline silicon, Part II: Kinetic considerations on thermal decomposition of pressurized monosilane. *International Journal of Chemical Kinetics*, 38(5):309–321, 2006.
- [110] A. A. Onischuk, V. P. Strunin, R. I. Samoilova, A. V. Nosov, M. A. Ushakova, and V. N. Panfilov. Chemical composition and bond structure of aerosol particles of amorphous hydrogenated silicon forming from thermal decomposition of silane. *Journal of Aerosol Science*, 28(8):1425–1441, 1997.
- [111] A. A. Onischuk, V. P. Strunin, M. A. Ushakova, and V. N. Panfilov. On the pathways of aerosol formation by thermal decomposition of silane. *Journal of Aerosol Science*, 28(2):207–222, 1997.
- [112] A. A. Onischuk, V. P. Strunin, M. A. Ushakova, and V. N. Panfilov. Studying of silane thermal decomposition mechanism. *International Journal of Chemical Kinetics*, 30(2):99–110, 1998.
- [113] A. A. Onischuk, A. I. Levykin, V. P. Strunin, K. K. Sabelfeld, and V. N. Panfilov. Aggregate formation under homogeneous silane thermal decomposition. *Journal of Aerosol Science*, 31(11):1263–1281, 2000.
- [114] A. A. Onischuk, A. I. Levykin, V. P. Strunin, M. A. Ushakova, R. I. Samoilova, K. K. Sabelfeld, and V. N. Panfilov. Aerosol formation under heterogeneous/homogeneous thermal decomposition of silane: experiment and numerical modeling. *Journal of Aerosol Science*, 31(8):879–906, 2000.

- [115] J.-H. Park, L. Gu, G. von Maltzahn, E. Ruoslahti, S. N. Bhatia, and M. J. Sailor. Biodegradable luminescent porous silicon nanoparticles for in vivo applications. *Nature Materials*, 8(4):331–336, 2009.
- [116] S. H. Park and S. N. Rogak. A novel fixed-sectional model for the formation and growth of aerosol agglomerates. *Journal of Aerosol Science*, 35(11):1385–1404, 2004.
- [117] R. I. A. Patterson and M. Kraft. Models for the aggregate structure of soot particles. *Combustion and Flame*, 151(1-2):160–172, 2007.
- [118] R. I. A. Patterson and W. Wagner. A stochastic weighted particle method for coagulation–advection problems. *SIAM Journal on Scientific Computing*, 34(3):B290–B311, 2012.
- [119] R. I. A. Patterson and W. Wagner. A stochastic weighted particle method for coagulation–advection problems. *SIAM Journal on Scientific Computing*, 34(3):290–311, 2012.
- [120] R. I. A. Patterson, J. Singh, M. Balthasar, M. Kraft, and J. R. Norris. The linear process deferment algorithm: A new technique for solving population balance equations. *SIAM Journal on Scientific Computing*, 28(1):303, 2006.
- [121] R. I. A. Patterson, J. Singh, M. Balthasar, M. Kraft, and W. Wagner. Extending stochastic soot simulation to higher pressures. *Combustion and Flame*, 145(3):638–642, 2006.
- [122] R. I. A. Patterson, W. Wagner, and M. Kraft. Stochastic weighted particle methods for population balance equations. *Journal of Computational Physics*, 230:7456–7472, 2011.
- [123] H. R. Paur, W. Baumann, H. Mätzing, and H. Seifert. Formation of nanoparticles in flames; measurement by particle mass spectrometry and numerical simulation. *Nanotechnology*, 16:S354, 2005.
- [124] Persistence of Vision Pty. Ltd. Persistence of Vision Raytracer (Version 3. 6), 2004. URL <http://www.povray.org/>.
- [125] E. L. Petersen and M. W. Crofton. Measurements of high-temperature silane pyrolysis using  $\text{SiH}_4$  IR emission and  $\text{SiH}_2$  laser absorption. *The Journal of Physical Chemistry A*, 107(50):10988–10995, 2003.

- [126] W. Phadungsukanan, S. Shekar, R. Shirley, M. Sander, R. H. West, and M. Kraft. First-principles thermochemistry for silicon species in the decomposition of tetraethoxysilane. *The Journal of Physical Chemistry A*, 113(31):9041–9049, 2009.
- [127] S. E. Pratsinis. Simultaneous nucleation, condensation, and coagulation in aerosol reactors. *Journal of Colloid and Interface Science*, 124(2):416–427, 1988.
- [128] S. E. Pratsinis and P. T. Spicer. Competition between gas phase and surface oxidation of  $\text{TiCl}_4$  during synthesis of  $\text{TiO}_2$  particles. *Chemical Engineering Science*, 53(10):1861–1868, 1998.
- [129] J. H. Purnell and R. Walsh. The pyrolysis of monosilane. *Proceedings of the Royal Society of London A*, 293(1435):543–561, 1966.
- [130] J. Pyykönen and J. Jokiniemi. Computational fluid dynamics based sectional aerosol modelling schemes. *Journal of Aerosol Science*, 31(5):531–550, 2000.
- [131] Reaction Design. CHEMKIN Software Theory Manual, 2011.
- [132] Reaction Design. CHEMKIN, retrieved 8 May 2013. URL <http://www.reactiondesign.com/chemkin/>.
- [133] N. Riemer, M. West, R. A. Zaveri, and R. C. Easter. Simulating the evolution of soot mixing state with a particle-resolved aerosol model. *Journal of Geophysical Research*, 114:D09202, 2009.
- [134] S. Rjasanow and W. Wagner. A stochastic weighted particle method for the Boltzmann equation. *Journal of Computational Physics*, 124(2):243–253, 1996.
- [135] S. N. Rogak, R. C. Flagan, and H. V. Nguyen. The mobility and structure of aerosol agglomerates. *Aerosol Science and Technology*, 18(1):25–47, 1993.
- [136] M. Sander, R. H. West, M. S. Celnik, and M. Kraft. A detailed model for the sintering of polydispersed nanoparticle agglomerates. *Aerosol Science and Technology*, 43(10):978–989, 2009.

- [137] M. Sander, R. I. A. Patterson, A. Braumann, A. Raj, and M. Kraft. Developing the PAH-PP soot particle model using process informatics and uncertainty propagation. *Proceedings of the Combustion Institute*, 33(1):675–683, 2011.
- [138] D. W. Schaefer and A. J. Hurd. Growth and structure of combustion aerosols: fumed silica. *Aerosol Science and Technology*, 12(4):876–890, 1990.
- [139] H. J. Schmid, S. Tejwani, C. Artelt, and W. Peukert. Monte carlo simulation of aggregate morphology for simultaneous coagulation and sintering. *Journal of Nanoparticle Research*, 6(6):613–626, 2004.
- [140] G. Schulze and M. Henzler. Adsorption of atomic hydrogen on clean cleaved silicon (111). *Surface Science*, 124(2):336–350, 1983.
- [141] T. Seto, M. Shimada, and K. Okuyama. Evaluation of sintering of nanometer-sized titania using aerosol method. *Aerosol Science and Technology*, 23(2):183–200, 1995.
- [142] S. Shekar, M. Sander, R. C. Riehl, A. J. Smith, A. Braumann, and M. Kraft. Modelling the flame synthesis of silica nanoparticles from tetraethoxysilane. *Chemical Engineering Science*, 70:54–66, 2011.
- [143] S. Shekar, W. J. Menz, A. J. Smith, M. Kraft, and W. Wagner. On a multivariate population balance model to describe the structure and composition of silica nanoparticles. *Computers & Chemical Engineering*, 43:130–147, 2012.
- [144] S. Shekar, A. J. Smith, W. J. Menz, M. Sander, and M. Kraft. A multidimensional population balance model to describe the aerosol synthesis of silica nanoparticles. *Journal of Aerosol Science*, 44:83–98, 2012.
- [145] R. Shirley, W. Phadungsukanan, M. Kraft, J. Downing, N. E. Day, and P. Murray-Rust. First-principles thermochemistry for gas phase species in an industrial rutile chlorinator. *The Journal of Physical Chemistry A*, 114(43):11825–11832, 2010.
- [146] B. W. Silverman. *Density estimation for statistics and data analysis*. Chapman & Hall/CRC, 1986.

- [147] K. Sinniah, M. G. Sherman, L. B. Lewis, W. H. Weinberg, J. T. Yates Jr, and K. C. Janda. Hydrogen desorption from the monohydride phase on Si (100). *The Journal of Chemical Physics*, 92:5700, 1990.
- [148] P. H. Stewart, D. M. Golden, and C. W. Larson. Pressure and temperature dependence of reactions proceeding via a bound complex. *Combustion and Flame*, 75(1), 1989.
- [149] M. T. Swihart and S. L. Girshick. Thermochemistry and kinetics of silicon hydride cluster formation during thermal decomposition of silane. *The Journal of Physical Chemistry B*, 103(1):64–76, 1999.
- [150] Thermodynamics Research Center, NIST Boulder Laboratories. Thermodynamics source database, retrieved 8 May 2013. URL <http://webbook.nist.gov>.
- [151] J. Troe. Theory of thermal unimolecular reactions in the fall-off range. I. Strong collision rate constants. *Berichte der Bunsengesellschaft für physikalische Chemie*, 87(2):161–169, 1983.
- [152] S. Tsantilis and S. E. Pratsinis. Evolution of primary and aggregate particle-size distributions by coagulation and sintering. *AIChE Journal*, 46(2):407–415, 2000.
- [153] S. Vemury and S. E. Pratsinis. Self-preserving size distributions of agglomerates. *Journal of Aerosol Science*, 26(2):175–185, 1995.
- [154] S. Vepřek, K. Schopper, O. Ambacher, W. Rieger, and MGJ Vepřek-Heijman. Mechanism of cluster formation in a clean silane discharge. *Journal of The Electrochemical Society*, 140:1935, 1993.
- [155] C. G. Wells, N. M. Morgan, M. Kraft, and W. Wagner. A new method for calculating the diameters of partially-sintered nanoparticles and its effect on simulated particle properties. *Chemical Engineering Science*, 61(1):158–166, 2006.
- [156] J. Z. Wen, M. J. Thomson, S. H. Park, S. N. Rogak, and M. F. Lightstone. Study of soot growth in a plug flow reactor using a moving sectional model. *Proceedings of the Combustion Institute*, 30(1):1477–1484, 2005.

- [157] E. Werwa, A. A. Seraphin, L. A. Chiu, C. Zhou, and K. D. Kolenbrander. Synthesis and processing of silicon nanocrystallites using a pulsed laser ablation supersonic expansion method. *Applied Physics Letters*, 64(14):1821–1823, 1994.
- [158] H. Wiggers, R. Starke, and P. Roth. Silicon particle formation by pyrolysis of silane in a hot wall gasphase reactor. *Chemical Engineering & Technology*, 24(3):261–264, 2001.
- [159] D. Woiki, L. Catoire, and P. Roth. High-temperature kinetics of Si-containing precursors for ceramic processing. *AIChE Journal*, 43(S11):2670–2678, 1997.
- [160] H. W. Wong, X. Li, M. T. Swihart, and L. J. Broadbelt. Detailed kinetic modeling of silicon nanoparticle formation chemistry via automated mechanism generation. *The Journal of Physical Chemistry A*, 108(46):10122–10132, 2004.
- [161] J. J. Wu and R. C. Flagan. Onset of runaway nucleation in aerosol reactors. *Journal of Applied Physics*, 61(4):1365–1371, 1987.
- [162] J. J. Wu, R. C. Flagan, and O. J. Gregory. Submicron silicon powder production in an aerosol reactor. *Applied Physics Letters*, 49(2):82–84, 1986.
- [163] J. J. Wu, H. V. Nguyen, and R. C. Flagan. A method for the synthesis of submicron particles. *Langmuir*, 3(2):266–271, 1987.
- [164] J. S. Wu, W. J. Hsiao, Y. Y. Lian, and K. C. Tseng. Assessment of conservative weighting scheme in simulating chemical vapour deposition with trace species. *International Journal for Numerical Methods in Fluids*, 43(1):93–114, 2003.
- [165] Y. Xiong and S. E. Pratsinis. Formation of agglomerate particles by coagulation and sintering—Part I. A two-dimensional solution of the population balance equation. *Journal of Aerosol Science*, 24(3):283–300, 1993.
- [166] M. Zachariah and M. Carrier. Molecular dynamics computation of gas-phase nanoparticle sintering: a comparison with phenomenological models. *Journal of Aerosol Science*, 30:1139–1152, 1999.

- [167] R. Zauner and A. G. Jones. On the influence of mixing on crystal precipitation processes—application of the segregated feed model. *Chemical Engineering Science*, 57(5):821–831, 2002.
- [168] H. Zhao and C. Zheng. A new event-driven constant-volume method for solution of the time evolution of particle size distribution. *Journal of Computational Physics*, 228(5):1412–1428, 2009.
- [169] H. Zhao and C. Zheng. A population balance-Monte Carlo method for particle coagulation in spatially inhomogeneous systems. *Computers & Fluids*, 71:196–207, 2013.
- [170] H. Zhao, F. E. Kruis, and C. Zheng. A differentially weighted Monte Carlo method for two-component coagulation. *Journal of Computational Physics*, 229(19):6931–6945, 2010.